ULTRASOUND SWITCHABLE FLUORESCENCE IMAGING BASED ON A TIME GATED ICCD CAMERA

by

SHUAI YU

DISSERTATION

Submitted in partial fulfillment of the requirements
for the degree of Doctor of Philosophy at
The University of Texas at Arlington
August 2019

Arlington, Texas

Supervising Committee:

Baohong Yuan, Supervising Professor

Hanli Liu

Kytai Nguyen

George Alexandrakis

Acknowledgements

I would like to express my sincere gratitude to my supervising advisor, Dr. Baohong Yuan, for your guidance and support in my graduate studies throughout the past five years. It is my fortune to work with you and have the opportunity to create new imaging techniques. In research, you give me a great flexibility and teach me to think and work independently. When I have a failure, you always encourage me: "A negative result sometimes may turn into a positive one, if we think in a different way. Never be afraid of failures." Your passion and dedication always inspire me to move on. Your humble academic attitude sets up a good model for me. Thank you for helping me become a better researcher and person.

It is my privilege to have Dr. Hanli Liu, Dr. Kytai Nguyen, and Dr. Georgios Alexandrakis on my dissertation committee. I am very grateful for all the insightful criticisms and suggestions given for my dissertation. Individually, I would like to express many thanks to Dr. Hanli Liu, from you I have learned a lot about fundamental knowledges in medical imaging and advices in giving a presentation; to Dr. Kytai Nguyen, for your collaboration and suggestions on synthesizing imaging contrast agents; to Dr. Georgios Alexandrakis, for your excellent teaching and your knowledge in optical imaging.

I would like to thank professors Dr. Yi Hong and Dr. Kytai Nguyen, for all the help, for giving me access to the facilities in their labs and providing invaluable advices. I'm very grateful to have so many wonderful colleagues, Dr. Yuan Liu, Dr. Mingyuan Wei, Dr. Bingbing Cheng, Dr. Jayanth Kandukuri, Dr. Ruilin Liu, Dr. Wenbin Cai, Dr. Jinglei Wu, Dr. Cancan Xu, Miss Bahar Saremi, Miss Liqin Ren, Mr. Tingfeng Yao, Mr. Yang Liu, Mr. Zhen Wang. Thank you all for your professional contributions, discussion, companions and support during the past five years. Especially, I'm very fortunate to have Dr. Yuan Liu and Mr. Tingfeng Yao as my labmates, from you I learned many about imaging instruments, and also Dr. Mingyuan Wei and Dr. Ruilin Liu, who are experts in chemistry and share a lot of knowledges in developing imaging contrast agents. I am thankful to our collaborators Dr. Francis D'Souza and Mr. Venugopal Bandi in the University of North Texas for providing environment-sensitive fluorophores. Thank you all! Without your help, I would never be able to accomplish my dissertation so smoothly.

I would like to thank the Office of Graduate Studies Dissertation Fellowship, which supports me to focus on completing this dissertation. I would like to express many thanks that my dissertation work was supported in part by funding from the CPRIT RP120052 and RP170564 (PI: Baohong Yuan), and the NSF CBET-1253199 (PI: Baohong Yuan) during the past years.

Very importantly, I’m sincerely thankful to my family, who always love me by your deepest heart. To my beloved parents, Jianping Yu and Shunai Xu, thank you for all your support more than financially in my graduate studies in the US during the past seven years. To my dear wife, Xuesong Yang, who is my best friend and partner, thank you for spending your best life with me and accompany me through all the difficulites. To my lovely daughter, Melanie Yu, you keep me learning to be a good parent as well as a caring person. To my beloved parents in law, Sumin Chen and Qingshuang Yang, thank you for bringing up your daughter with excellent personalities. Dear parents, thank you for support in our happy marriage and our PhD career. Without you, I wouldn’t be here today.

I would like to extend my appreciation to all my friends and the church family of the Arlington Chinese Church, and my pastor Edward Leung. Without your prayers and encouragements, I would not be able to finish the work so successfully.

Lastly, I praise Lord Jesus Christ for giving me wisdom, strength, patience and determination to complete my dissertation. To God be the Glory!

July, 30th, 2019

ABSTRACT

ULTRASOUND SWITCHABLE FLUORESCENCE IMAGING BASED ON A TIME GATED ICCD CAMERA

Shuai Yu, Ph.D.

The University of Texas at Arlington, 2019

Supervising Professor: Baohong Yuan

Ultrasound switchable fluorescence (USF) imaging has been proposed as a novel imaging modality which provides microscopic fluorescence imaging in centimeter-deep tissue. USF is possible to reveal many interesting phenomena such as microcirculation, tumor angiogenesis, and cancer metastasis and diagnose early-stage cancer. USF adopts a focused ultrasound (FU) to repetitively switch "on" fluorescent agents in tissue, and the USF photons scatter out and are captured by a detector. A USF image provides acoustic resolution and optical sensitivity. In USF, there are two key components: 1) an excellent USF contrast agent; and 2) a sensitive USF imaging system. The major challenge of USF is to develop USF contrast agent with excellent USF properties and also long-term stability, bio-stability, and functionalization, as well as to develop a USF imaging system with high detection sensitivity, specificity, efficiency, and also flexible experimental operations for a desired imaging quality. In addition, *in vivo* USF imaging is an important step to push USF technique to future biomedical applications. This dissertation focuses on investigating and developing new USF contrast agents and imaging systems, for the purpose of improving USF imaging qualities (i.e., sensitivity, spatial resolution, imaging contrast, data acquisition time) and also its feasibility of long-term study, functional imaging, as well as *in vivo* USF imaging.

This work is categorized into three major parts: (I) USF contrast agents; (II) a new USF imaging system; and (III) *in vivo* USF imaging. In part (I), we developed two series of NIR USF contrast agents: (a) new generation ICG-encapsulated poly(N-isopropylacrylamide) nanoparticles, and (b) ADP- and ZnPc- encapsulated pluronic-based nanocapsules. We synthesized, characterized, and selects those with excellent USF properties. Meanwhile, we also discussed how their performance affected a USF image. In part (II), we developed an ICCD camera-based, time-domain USF imaging system. We demonstrated its features and advantages for USF imaging. Also, we described the

tradeoffs inherent in USF imaging and suggested appropriate USF imaging strategies. In addition, based on this system, we developed several USF imaging processing algorithms for a better imaging quality. In part (III), we successfully carried out *in vivo* USF imaging in mice via an ICCD camera-based *in vivo* USF imaging system. USF imaging of tumors and *in vivo* organs were successfully achieved in the experiments.

In part (I)-(a), the results shows that the new generations ICG-NPs have a significantly improved shelf (> 6 month) compared to the old generation (<1 month). Also, the new generation ICG-NP is conjugated with functional groups (hydroxyl or carboxyl) and is capable of functional imaging when attached with a targeting moiety. Besides, we investigated that the effect of the temperature-switching threshold (T_{th}) of the agent should be slightly higher than the background temperature (T_{BG}) for a best signal-acquisition efficiency. The T_{th} should be controlled around 38–40 °C for a best *in vivo* USF imaging. In part (I)-(b), the results show that the selected ADP- and ZnPc- encapsulated pluronic-based nanocapsules have excellent USF properties. In addition, we demonstrated that some factors: 1) pluronic categories, and 2) nanocapsules' concentration will affect the T_{th}s, while other factor: 3) fluorophore categories will not. The pluronics' T_{th} sequence is F127 < F98 < F68 < F38 based on using different pluronics. And, a lower nanocapsule concentration brings a higher T_{th}. We also discussed to adopt the nanocapsules as temperature sensors. In part (II), we demonstrated the ICCD camera-based time-domain USF imaging system is appropriate for USF imaging. Meanwhile, we could balance the tradeoffs between imaging qualities (i.e., SNR, spatial resolution, temporal resolution) by adjusting experimental parameters including CCD camera recording time, FU power, imaging depth, and gate delay of ICCD camera as well as selecting an appropriate USF contrast agent. Thus, we could acquire a best USF image based on our desire. Following that, we investigated several USF imaging processing algorithms to improve USF imaging qualities including: 1) improving the SNR by a correlation method; 2) improving the spatial resolution by an ascending-slope-weighted method; 3) improving the spatial resolution by an algorithm called a spatial back-projection method. In part (III), *In vivo* USF imaging in the mouse's glioblastoma tumor with one or multiple targets were demonstrated. Also, *in vivo* USF imaging of the mouse's spleen and liver were achieved. The results were validated by 3D co-registration with the micro-CT images and showed *in vivo* feasibility of USF imaging. We adopted ICG-NP as the *in vivo* USF contrast agents, which shows a high bio-stability in mice's tumor as well as spleen and liver. Finally, we discussed the advantages of the ICCD camera-based system for *in vivo* USF imaging.

Table of Contents

Chapter 1 Introduction

1.1 Motivation of ultrasound-switchable fluorescence (USF) imaging

Over the past decades, people were seeking non-invasive biomedical imaging techniques that are appropriate for cancer detection and staging, one of the leading cause of death worldwide.[1,2] Early-stage cancer diagnosis is crucial for the survival rate of patients. For example, the five-year relative survival rate of breast cancer is 100% at stages 0 and 1, which drops significantly to 22% at stage 4, according to National Cancer Institute. Compared to other common cancer diagnostic methods including biopsy, blood or urine test, and genetic tests[2], biomedical imaging has dominant advantages such as non-invasive operation and real-time monitoring.

Currently, the most common biomedical imaging modalities include: X-ray[3] and X-ray based computed tomography (CT)[4], ultrasound[3,5], magnetic resonance imaging (MRI)[6,7], positron emission tomography PET[8,9] and single-photon emission computerized tomography (SPECT)[10], and optical imaging[11-18]. When comparing and selecting different imaging modalities, an important consideration is about the imaging qualities, which include: 1) imaging depth, 2) spatial resolution, 3) acquisition time, 4) imaging contrast and sensitivity.[19] At the same time, other considerations such as cost, bio-safety are essential too. Comparing these imaging modalities, CT and MRI have an excellent imaging depth (up to tens of centimeters) as well as a good spatial resolution. Thus, they are appropriate for whole body imaging. However, their sensitivity to biological tissue is relatively low and it is difficult to track molecular- and/or cellular- level biological information.[20] What's worse, MRI and CT are very costly for patients. Also, MRI has a relatively slow imaging speed and it usually takes a long time diagnosis. CT adopts X-ray as the external energy source and it's harmful for patients' healthy because of ionizing radiation.

On the contrary, optics and ultrasound share many beneficial features over MRI and CT. Both of them are fast, cost-efficient, safe, and also flexible in selecting appropriate imaging contrast agents.[21-23] Besides, the optical imaging provides a highest sensitivity in biological tissue and is capable of tracking many interesting physiological and pathological micro-phenomena such as microcirculation, angiogenesis, and cancer metastasis.[24-26] In addition, because of a wide range of wavelengths (from 400 to 1300 nm), optics is capable of multiplex imaging based on different colors.[27,28] Thus, many molecular- or cellular- level bio-interactions could be revealed. However, due to a high scattering property in biological tissue, the spatial resolution of optics significantly decreases with the increase of imaging depth.[24] Consequently, except for optical microscopy[18,29], fluorescence microscopy[11,30], and super solution fluorescence microscopy[31], which have a high spatial resolution (from hundreds of nanometers and up to a few nanometers) and meanwhile a very low imaging depth (< 1 mm), as well as optical coherence tomography[13,32], which has a spatial resolution up to a few microns and meanwhile an imaging depth to a few millimeters, other common optical imaging techniques (such as diffusive optical tomography[12] and fluorescence diffusive optical tomography[16,17]) serves low spatial resolution when imaging deep tissues. On the contrary, ultrasound has a scattering coefficient two to three orders of magnitude less than light in the biological tissue[33], which allows it penetrate in centimeter-deep tissue while maintaining good spatial resolution (up to hundreds of microns). Yet, a major disadvantage is its relatively low sensitivity to tissue and its contrast agents (i.e., microbubbles). [34]

Regarding to the other two modalities: PET and SPECT, they have a high detection sensitivity but meanwhile a low spatial resolution in deep tissue, similar to optical imaging.[8-10] Also, their cost are very high on current developments. In Table 1.1, we summarizes ranks about pros/cons of all the imaging modalities.

Table 1.1

Rank	**Depth/Resolution**	**Time**	**Sensitivity**	**Cost**	**Multiplex Imaging**
1	CT, MRI	Optics, Ultrasound	Optics, PET, SPECT	Optics, Ultrasound	Optics (possible)
2	Ultrasound	CT, PET, SPECT	Ultrasound	CT	Others (difficult or impossible)
3	Optics, PET, SPECT	MRI	MRI	MRI, PET, SPECT	
4			CT		

As one of the optical imaging technique, fluorescence imaging has attracted many interests over the past decades because of its high sensitivity, vast selection of probes (e.g., organic dyes, fluorescent proteins, quantum dots and nanoparticles), non-ionizing radiation, high sensitivity and specificity.[21,22,25,28,35,36] One outstanding advantage is its multicolor imaging via multiple fluorophores that thus enables fluorophore-based biomarkers to reveal cellular-level or molecular-level biological interactions.[27,28] More importantly, many fluorophores are highly sensitive to a micro-environment change in biological tissue such as tissue's pH, temperature, viscosity and polarity, as well as bio-molecule concentrations. Thus, fluorescence imaging could be adopted as a functional diagnosis of abnormalities in human body, including angiogenesis, metastasis, hypoxia.[24-26] Also, fluorescence imaging provides a guidance for drug delivery therapy.[37,38] It is worth mentioning here that, in selection of various wavelengths, near-infrared (NIR) fluorescence is highly desirable since it has less absorption and thus a good penetration in tissue.[24] Unfortunately, similar to other optical imaging, a major drawback of fluorescence imaging is its degraded spatial resolution caused by tissue's high scattering property. Consequently, fluorescence imaging cannot resolve much interesting microscopic information located in centimeter-deep tissue because of its low capability in deep-tissue imaging.

Over the past years, researchers have been investigating fluorescence imaging in deep tissue with high spatial resolution as well as high signal-to-noise ratio (SNR). One of them is called fluorescence diffuse optical tomography (FDOT). FDOT takes advantage of highly scattered photons with reconstruction algorithms and thus could achieve an image depth of a few centimeters. However, its spatial resolution is still low (a few millimeters). [16,17,39,40] In the recent few years, several technologies have been proposed and developed to overcome the limitation of low spatial resolution. One general idea is to use focused ultrasound (FU) to confine fluorescence emission into a small volume. Thus, fluorescence images with acoustic resolution (hundreds of microns, depending on the frequency) or even better than can achieve in deep tissues. Based on this idea, one technology is to focus excitation light in deep tissue by FU, so called time-reversed ultrasonically encoded optical focusing.[41-46] Another technology is to confine fluorescence emission by FU, so called ultrasound modulated or switchable fluorescence.[47-71] The former applies to any fluorophore excitation but requires a complicated imaging system. The latter requires a relatively simple system but demands unique contrast agents.

We have recently developed a technique which belongs to the latter: ultrasound switchable fluorescence (USF) imaging.[57,58,63-70] USF serves a multi-modality imaging technique and combines the advantages of both ultrasound imaging and fluorescence imaging. Table 1.2 summarizes the advantages of USF imaging properties in comparison to ultrasound imaging and FDOT. As mentioned, USF has a similar spatial resolution to other deep-tissue optical imaging technologies developed in the recent years, such as photoacoustic tomography[33,72], time-reversed ultrasonically encoded optical focusing[41-46], and ultrasound-modulated fluorescence[47,48,61]. Furthermore, USF has many unique features. First, USF signal has high detection specificity to its contrast agent because the detected USF photons only come from the agent. Second, USF has high detection sensitivity because we have developed several USF contrast agents that are highly sensitive to a small temperature change (only a few Celsius degrees) and could release strong fluorescence after being switched on[57,63-66]. Also, USF signal can be externally manipulated by controlling the FU signal and the data acquisition time[67] in a sensitive USF imaging system, which makes USF achieve a desired signal-to-noise ratio (SNR). Third, since USF only requires a temperature increase of a few Celsius degrees in tissue, it is safe for *in vivo* imaging. The reason is that a USF contrast agent's temperature threshold (T_{th}) could be well controlled slightly above the body temperature (~37 °C) and also its temperature transition bandwidth (T_{BW}) could be narrowed down to a few degrees (usually 3–5 °C). As a result, a corresponding temperature increase *in vivo* (e.g., from 37 °C to 40 °C) should provide sufficient energy to acquire a USF signal. Lastly, USF can be inherently combined with high intensity focused ultrasound (HIFU) treatment.

Table 1.2

Rank	**Ultrasound**	**FDOT**	**USF**
Sensitivity	Relatively poor	Excellent	Excellent (= FDOT)
Imaging Depth	Good (a few centimeters)	Good (a few centimeters)	Good (= ultrasound)
Resolution	Good (~ 10^1 to 10^2 microns)	Poor (> 1 mm)	Good (= ultrasound)
Imaging contrast	Acoustic contrast (structural information)	Optical contrast (functional information)	Optical contrast (= FDOT)
Multiplex imaging	Not possible	Possible	Possible (= FDOT)

1.2 Principles of USF imaging

In USF imaging, there are two essential components: an excellent USF contrast agent and a highly sensitive USF imaging system. The USF contrast agent is temperature-sensitive and its fluorescence intensity and/or lifetime changes as a function of temperature. Typically, when the temperature is below a threshold, its fluorescence is highly quenched and it is in "switch-off" state; when the temperature rises over the threshold, the contrast agent will release strong fluorescence and it is in "switch-on" state. In addition, its switchability of fluorescence is repetitive and thus the agent could be switched "on" and "off" for many times. In a USF imaging system, the key components are: an excitation light, a focused ultrasound (FU) transducer, and a sensitive optical detector. The FU transducer is adopted to induce a temperature rise in the imaging target (i.e., tissue). The size of the "heated" volume depends on the size of the ultrasound focus, which is usually hundreds of microns. When the USF contrast agent encounters such a temperature rise in tissue with the excitation light on, it will release strong fluorescence and the emitted photons are detected by the optical detector in USF imaging system. The detected signal is termed "a USF signal". By scanning the FU transducer, a USF image is acquired and provides the distribution of USF contrast agents in tissue. Because both the delivery of the excitation light and the collection of emission light depend on highly scattered (or diffused) photons, USF can achieve an imaging depth of a few centimeters. Meanwhile, because the emitted USF signal only comes from the FU focus, the USF image can achieve a high spatial resolution up to hundreds of microns.

1.3 USF contrast agents

1.3.1 Principle of designing a USF contrast agent

When a polarity- and viscosity-sensitive fluorophore is encapsulated in or conjugated with temperature-sensitive polymers, its fluorescence will become temperature-sensitive and the fluorescence intensity and/or lifetime changes as a function of temperature. This is because when the temperature rises over the lower critical solution temperature (LCST) of the polymers, the polymers experience a phase transition from hydrophilic to hydrophobic. Thus, the encapsulated (or conjugated) fluorophore experiences a microenvironment change from water-rich to polymer-rich. Due to its sensitivity to polarity and viscosity, this change sometimes increases the quantum yield significantly. As a result, when a USF contrast agent stays in a temperature below the LCST, it fluorescence is usually very weak; while temperature rises over the LCST, the agent will release strong fluorescence. For example, Figure 1.1 shows the illustration of indocyanine green (ICG)-encapsulated poly(N-isopropylacrylamide) nanoparticles (ICG-NPs), one of the commonly used USF contrast agents in USF imaging.[57] When the environment temperature is below a threshold (LCST of the polymers), the polymers are hydrophilic and thus the NPs absorb a large amount of water. Therefore, their size is relatively large.[73] ICG molecules inside the NPs suffers from a low quantum yield in a water-rich environment because of the water's high polarity and non-viscosity. When the temperature rises over the LCST, the polymers experience a phase transition from hydrophilic to hydrophobic. Thus, the NPs dramatically shrinks to a small size and the water molecules inside the NPs are expelled outside. The ICG molecules inside the NPs now are exposed to a polymer-rich microenvironment and its quantum yield increases significantly due to the polymers' high viscosity and low polarity. As a result, the ICG-NPs release strong fluorescence when the temperature is higher than the LCST.

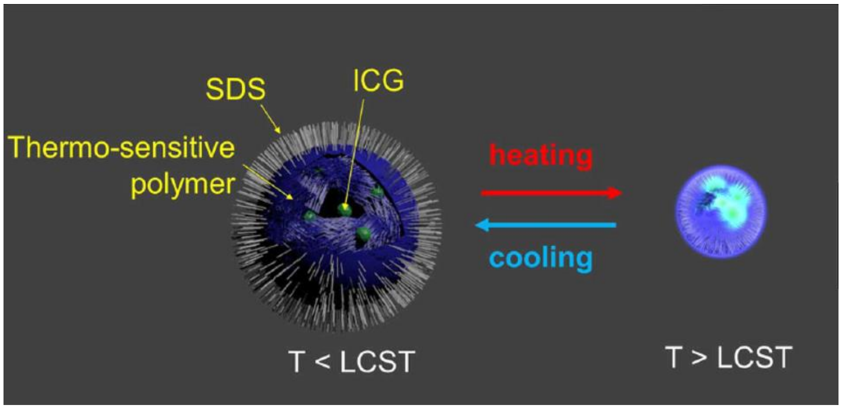

Figure 1.1 Illustration of ICG-encapsulated poly(N-isopropylacrylamide) nanoparticles (ICG-NPs) as a USF contrast agent. [57]

In addition to the switchability, the fluorescence should be capable of repetitively switching between the two temperatures.[57] In USF imaging, the USF contrast agents are switched "on" by the FU beam in a small volume and switched "off" by thermal diffusion in biological tissue. Also, a USF image is acquired by a point-to-point scan method and the agents would be switched "on" and "off" repetitively. Thus, the repeatability of switch is essential and ensured in designing a USF contrast agent.

1.3.2 Characterization of the USF contrast agents

In our previous work[63], we summarized five parameters characterizing the performance of a USF contrast agent. They are: (1) the fluorescence peak excitation and emission wavelengths (λ_{ex} and λ_{em}); (2) the fluorescence intensity ratio between its on- and off- states (I_{on}/I_{off}); (3) the fluorescence lifetime ratio between its on- and off- states (τ_{on}/τ_{off}); (4) the temperature threshold to switch on the fluorescence (T_{th}); and (5) the temperature transition bandwidth (T_{BW}). Figure 1.2 shows a diagram of the characterization. In the plot, the x-axis represents the environment temperature of the USF contrast agent, and the y-axis represents its fluorescence intensity or lifetime. The fluorescence intensity/lifetime changes as a function of temperature: the fluorescence intensity and/or lifetime is weak (short) when the temperature is below the T_{th}. When the temperature rises over T_{th}, the fluorescence intensity and/or lifetime increases significantly. When the temperature rises across the T_{BW}, the fluorescence becomes stabilized again. The fluorescence intensity and lifetime ratio between its on- and off- states are termed as I_{on}/I_{off} and τ_{on}/τ_{off}. An ideal USF contrast agent should have (a) near-infrared (NIR) λ_{ex} and λ_{em}; (b) a high I_{on}/I_{off} and a high τ_{on}/τ_{off}; (c) an adjustable $T_{th;}$ and (d) a narrow T_{BW}. This is because (a) NIR wavelengths provide good penetration to biological tissue; (b) a high I_{on}/I_{off} and a high τ_{on}/τ_{off} provide high sensitivity to detect a USF signal from background fluorescence; (c) an adjustable T_{th} provides USF contrast agents appropriate for both *ex vivo* and *in vivo* scenarios; and (d) a narrow T_{BW} provides fluorescence-switching efficiency by ultrasound heating (usually a few Celsius degrees).

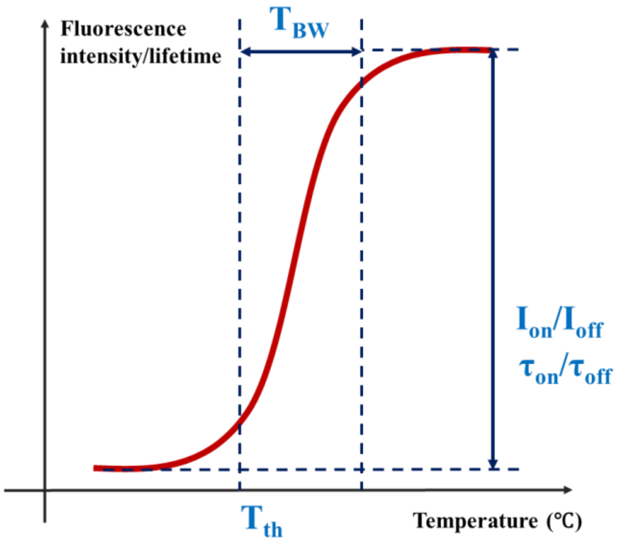

Figure 1.2 Characterization of a USF contrast agent's fluorescence intensity or lifetime as a function of temperature.[63] I_{on}/I_{off}: the fluorescence intensity ratio between its on- and off- states; τ_{on}/τ_{off}: the fluorescence lifetime ratio between its on- and off- states; T_{th}: the temperature threshold to switch on the fluorescence; T_{BW}: the temperature transition bandwidth.

1.3.3 Long-term stability, bio-stability and functionalization of the USF contrast agents

Long-term stability, also referred as shelf-life, of a USF contrast agent is highly desirable for USF imaging. When conducting comparative longitudinal studies such as monitoring disease development and treatment evaluation over a long period (usually > 6 months), adopting USF contrast agents synthesized from the same batch can avoid those unwanted variations that originate from the different batches of production. Meanwhile, fast degradation will make it challenging or sometimes even impossible to maintain contrast agents with same parameters and stable properties. In addition, stable contrast agents can save a large amount of effort (such as time and cost) by avoiding having to repetitively make new batch agents to replace quickly degraded agents. This is the key to reducing the cost of agent and further increasing its commercialization potential. Finally, a long-term stable USF contrast is necessary for applications that use USF imaging to monitor implanted medical device, in which USF contrast agents are sealed into the medical device for long-term use (up to years), making USF performance stability extremely important. Ideally, a desired shelf-life of a USF contrast agent should be longer than 6 months and up to a few years.[64]

Bio-stability of a USF contrast agent plays a vital role in the success of USF imaging when in live animals. There are several ways to inject the USF contrast agents in a live animal subject[74]: a) subcutaneous injection; b) intramuscular injection; c) intravenous injection; and d) intraperitoneal injection. By injection methods a) and b), in an initial state the USF contrast agents will cluster in the tissue's intercellular space and mainly interact with its surrounding biological environment. At a later stage, the agents might permeate through the tissue to blood and bio-distribute to the overall body, which will be a similar situation as by an intravenous injection method c). By c) an intravenous injection, the USF contrast agents are distributed throughout the body and are more likely to be partially or fully metabolized in the organs. Meanwhile, there is a chance that the agents would accumulate in some specific organs (such as liver) due to a specific metabolism. If the agents in the subcutaneous/muscular tissue, or in the organs still remain USF properties (i.e., their fluorescence changes as a function of temperature), they could be adopted as USF imaging targets *in vivo*. From the perspective of acquiring an *in vivo* USF signal successfully, the USF contrast agents should, at minimum, remain two key properties: (1) the USF contrast agents should remain the original T_{th}; (2) the USF contrast agents should remain a high fluorescence intensity on-to-off ratio (i.e., a high I_{on}/I_{off}).

Functionalizing the surface of a USF contrast agent is another important goal for conducting USF molecular imaging in biological tissue with high resolution. In cancer diagnosis, vascular endothelial growth factor (VEGF) has been discovered an important signaling protein in tumor angiogenesis.[75] The receptors of VEGF (VEGFR) are highly expressed in active-growing vessels in tumor and these vessels are appropriate functional imaging targets for cancer diagnosis. For example, if the USF contrast agent is functionalized with VEGF protein and specifically targets to the tumor vessels, USF imaging has a potential capability of cancer detection.

1.4 USF imaging system

In a USF imaging system, the essential instruments include: an excitation light, an FU transducer, and a sensitive optical detector.[57,58,65] The excitation light illuminates the tissue and the USF contrast agents inside. The FU transducer sends an ultrasound signal to the tissue and induces a temperature rise in a small volume (i.e., the ultrasound focus). The USF contrast agents in the ultrasound focus are switched "on" and emit USF photons. The USF photons are scattered to the tissue surface and captured by the sensitive optical detector. Currently, USF imaging adopts a point-to-point scan method and a motorized three-dimensional (3D) stage is adopted to move the FU transducer or the imaging subject. In our previous work[57,58,65], several USF imaging systems have been developed and are described below.

1.4.1 Direct current (DC) USF imaging system

In a direct current (DC) USF imaging system, a direct current continuouos wave (CW) laser was adopted as the exication light. Figure 1.3 (a) shows a simple diagram of acquiring a USF signal from a DC USF imaging system.[57] The first line represents that the FU transducer sends a ultrasound signal to the tissue with a fixed exposure time. The second line represents that the temperature at the FU focus rises up after the start of ultrasound exposure. At the end of ultrasound exposure, the temperature at the ultrasound focus starts to decrease. The third line represents the DC laser output. The output laser intensity/power is fixed at a constant. The fourth line represents the acquired USF signal. Figure 1.3 (b) shows an example of a DC USF imaging system adopted in our previous work.[57] Briefly, a diode laser (wavelength: 808 nm) was adopted to illuminate the sample at a DC mode and the USF signal was detected in a photomultiplier (PMT) and finally recorded in an oscilloscope. Due to that fact that the USF signal is extracted from a background fluorescence only by a small intensity increase at a low frequency range, and also the fact that many noises are added during signal acquisition (such as dark current noise in PMT, readout noise), the main limitation of a DC USF imaging system is low signal-to-noise ratio (SNR).

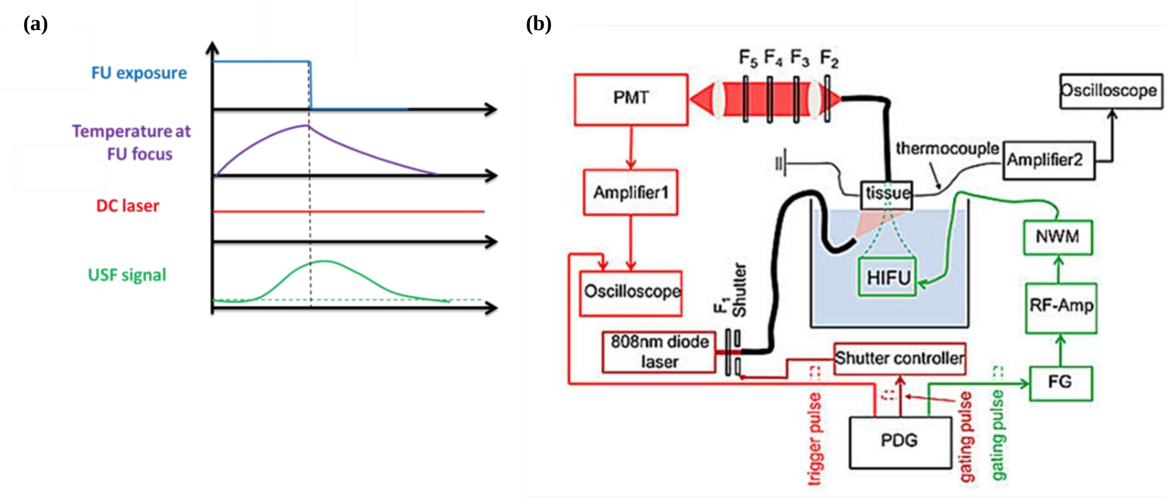

Figure 1.3 (a) Diagram of a direct current (DC) USF imaging system. (b) Set-up of a DC USF imaging system adopted in our previous work. [57]

1.4.2 Frequency-domain USF imaging system

To overcome the limitation of the DC USF imaging system, a frequency-domain USF imaging system was developed.[65] Figure 1.4 (a) shows a simple diagram of a frequency-domain USF imaging system. Instead of using an excitation laser in the DC mode, we modulate the laser at a specific frequency (e.g., 1 kHz) and thus the fluorescence is modulated at the same frequency as well. Consequently, the USF signal is also modulated at this frequency and thus could be specifically identified by a lock-in amplifier (i.e., a homodyne detection technique[76]). By frequency modulation and lock-in detection, the SNR of a USF image could be significantly improved. In Figure 1.4 (a), similarly, the first line represents the FU exposure, and the second line represents the temperature change at the FU focus. The third line represents the modulated laser at a fixed frequency, with a DC offset. The fourth line represents the USF signal, which is also modulated. The fifth line represents the lock-in interference at the same frequency. The sixth line represents the lock-in output, which is proportional to the USF signal. Figure 1.3 (b) shows an example of a frequency-domain USF imaging system adopted in our previous work.[65] Similar to the DC USF imaging system, a diode laser was adopted to illuminate the sample at a DC mode and the USF signal was detected by a PMT. The laser was modulated at a fixed frequency (1 kHz) by a function generator (FG). Following the PMT and its amplifier, a digital lock-in amplifier was adopted to further amplify the USF signal with a reference signal (1 kHz) from the same function generator. The output USF signal was finally acquired by a data-acquisition card (DAC) and record in a computer.

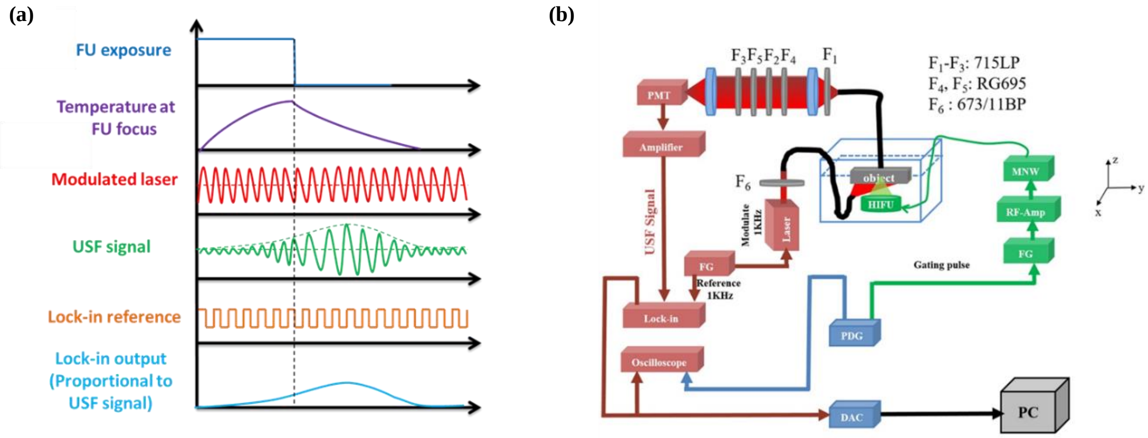

Figure 1.4 (a) Diagram of a frequency-domain USF imaging system. (b) Set-up of a frequency-domain USF imaging system adopted in our previous work.[65]

1.4.3 Time-domain USF imaging system

In the previous two USF imaging systems, it adopts CW laser as the excitation source. Differently, a time-domain USF imaging system adopts a narrow pulsed laser as the excitation source. Figure 1.5 (a) shows a simple diagram of a frequency-domain USF imaging system. Similarly, the first line represents the FU exposure, and the second line represent the temperature change at the FU focus. The third line represents a narrow pulsed laser (the red solid arrow). In the fourth line, besides the laser pulse (the red dash arrow), there are two output pulses (the two green solid curves). The first pulse is relatively narrow in the plot and represents the background. The background may include laser leakage, auto-fluorescence from tissue, and non-100%-off background fluorescence from the USF contrast agents when they are at "off" state. The second pulse is relatively broad and represents the USF signal. The plot represents a scenario that the background has a short lifetime while the USF signal has a long lifetime. In this situation, if the USF signal is acquired in a time-gated window with a time delay, the background can be significantly removed. The green shadow area in the fourth line represents the USF signal acquired in such a time-gated window. By doing this, the SNR of a USF image may be significantly improved due to an increase of signal-to-background ratio (SBR). The time-domain USF imaging system was first developed in a PMT detector-based USF imaging system.[58] Figure 1.5 (b) shows the time-domain USF imaging system adopted in the work. Briefly, a pico-second pulsed supercontinuum laser (pulse width: ~5 ps; with a broad illumination band) was adopted as the excitation source in this system. A cooled PMT was adopted as the detector. The USF contrast agent was DBD-AA labeled PNIPAM, whose T_{th} = ~ 31–32 °C, I_{on}/I_{off} = ~ 4–5 folds, and more importantly, τ_{on}/τ_{off} = 14 ns/ 4 ns = ~ 3.5 folds. By a narrowed excitation source, a fast detector, and a USF contrast agent with a high τ_{on}/τ_{off} (and also a high I_{on}/I_{off}), a time-domain USF imaging technique can be implemented.

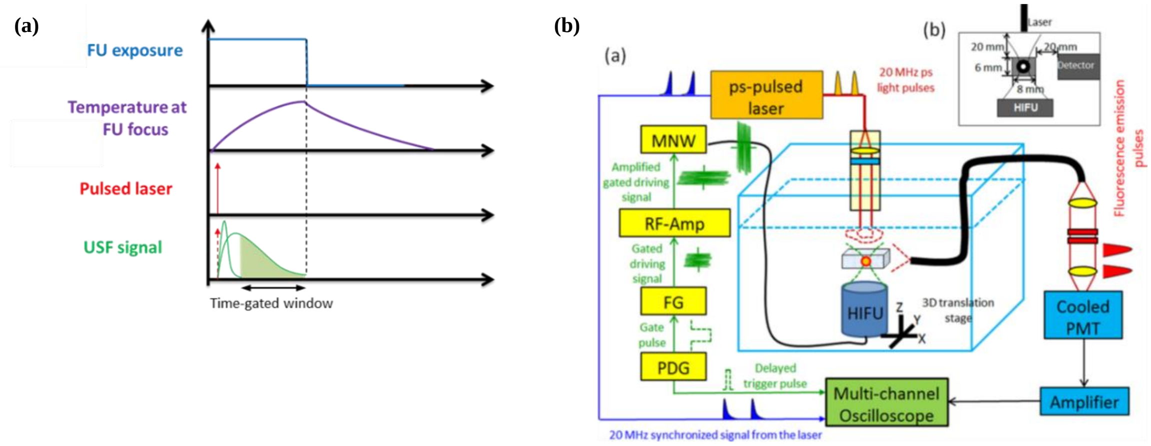

Figure 1.5 (a) Diagram of a time-domain USF imaging system. (b) Set-up of a time-domain USF imaging system adopted in our previous work.[58]

1.4.4 PMT-based v.s. camera-based USF imaging system

In review of the USF imaging systems developed in the previous work, the PMT was adopted as the detector. It has several advantages. First, it has a high sensitivity to a weak optical signal. Second, it usually has a fast detection speed (< 1 ns response time) and is capable of continuous acquisition. One main limitation of using a PMT in a USF imaging system is that it is a single sensing element and is not capable of providing the spatial information about the incoming photons. Here, we propose that adopting a camera has several advantages over adopting the PMT as the detector in the USF imaging system. The camera could provide two dimensional (2D) spatial information about a USF signal. As described, USF photons come from deep biological tissue and scatter to the tissue surface before detected. Thus, the acquired USF photons are usually dispersed in a large field of view (FOV). A camera-based USF imaging has the potential to increase the USF photon-collection efficiency. In addition, a 2D USF signal may provide useful information for analysis and thus to improve imaging qualities. Overall, a camera-based USF imaging system should be developed and investigated.

1.5 USF imaging qualities

Common imaging qualities include: imaging contrast and sensitivity, spatial and temporal resolution, as well as capability of imaging depth.[19] A higher contrast, a higher resolution and also a capability of larger imaging depth are desirable. Nevertheless, there exit tradeoff relationships among these qualities.[19,77] Accordingly, the tradeoffs should apply to USF imaging quality as well. Meanwhile, the imaging qualities rely on experimental parameters so that ways to balance the tradeoffs depend on how to adjust these parameters. In USF imaging these parameters may include: signal acquisition time/speed, and FU energy. For example, a higher FU power may induce a higher USF signal due to the increased size of the heated volume in tissue, but at the same time may also reduce the spatial resolution of the USF image. Investigation of the relationship between the imaging qualities and how to balance them is essential to achieve a best desired USF image.

1.6 *In vivo* feasibility of USF imaging

In vivo USF imaging in live animals is an important step as pre-clinical studies to push the USF technique to biomedical applications in the future. Recently, for the first time, we have achieved in vivo USF imaging in mice.[70,78] Acquiring USF signals and a USF image in live animals is likely to be more difficult compared to that in phantoms since the contrast agent would be bio-distributed and metabolized *in vivo*. Meanwhile, noises such as tissue auto-fluorescence[79] and motion artifacts are added to *in vivo* USF imaging. Consequently, the signal-to-noise ratio may be low. To successfully achieve *in vivo* USF imaging, the following studies should be conducted: 1) a bio-stable USF contrast agent should be synthesized and well characterized for *in vivo* use; 2) its bio-distribution and bio-stability should be studied; 3) an appropriate *in vivo* USF imaging system should be developed. 1) and 2) are partially discussed in the previous section 1.4.3. Briefly, the USF contrast agent should have a high detection sensitivity, excellent bio-stability, and also an appropriate metabolic pathway (i.e., an appropriate imaging target *in vivo*). In addition to the contrast agent, the USF imaging system should have a high detection sensitivity as well and also a suitable platform to operate the animals (such as an anesthesia device in the system).

1.7 Objectives of this dissertation

The objectives of this dissertation is to develop USF imaging technique regarding to 1) improving the USF contrast agents' performance based on the characterizations (i.e., NIR spectrum, a high I_{on}/I_{off}, a high τ_{on}/τ_{off}, an adjustable T_{th}, and a narrow T_{BW}) as well as their long-term stability, bio-stability, functionalization; 2) developing a sensitive USF imaging system and improving the USF imaging qualities (i.e., imaging contrast/SNR, spatial/temporal resolution, and imaging depth); 3) achieving *in vivo* USF imaging in live animals. The approaches are 1) developing a series of novel NIR USF contrast agents including (a) new generation ICG-encapsulated poly(N-isopropylacrylamide) nanoparticles (ICG-NPs), and (b) aza-BODIPY (ADP)- or Zinc phthalocyanine (ZnPc)-encapsulated pluronic nanocapsules; 2) developing an ICCD camera-based time-domain USF imaging system; 3) investigating the feasibility of *in vivo* USF imaging in a small animal model (mice) and carrying out *in vivo* USF imaging experiments in mice's tumor and organs. The specific aims were addressed in the following chapters.

In Chapter 2, we developed two new protocols of ICG-NPs for USF contrast agents with long-term stability, adjustable LCST, and functionalization. The shelf life of these new generation ICG-NPs developed in this study is much longer (>6 months)[64] than that of the first generation (<1 month)[57]. It is worth mentioning that, we tested some remaining batches of ICG-NPs and their USF performance is still very good as of writing (>3 years). Thus, we except the new generation ICG-NPs have a shelf life up to a few years. In this chapter, we also synthesized the new ICG-NPs with conjugation-functional groups (hydroxyl or carboxyl), which can be used for molecular imaging if they are attached with a targeting moiety. Finally, we investigated the effect of the temperature-switching threshold (T_{th}) of the agent and the background temperature on USF imaging. Maintaining the agents' temperature threshold slightly above the background temperature is necessary for conducting USF imaging successfully and efficiently. Therefore, for *in vivo* USF imaging, the temperature threshold of the contrast agents should be controlled around 38–40 °C, which is slightly above the body temperature of ~37 °C.

In Chapter 3, we synthesized, characterized, and selected a series of temperature-switchable fluorescence nanocapsules, by encapsulating two series of NIR fluorophores (ADP and ZnPc) in four pluronic polymers (F127, F98, F68, and F38). These nanocapsules showed excellent temperature-switchable properties of fluorescence intensity and/or lifetime. Also, we investigated that some factors (i.e., pluronic categories and nanocapsules' concentration) affected the nanocapsules' T_{th}s while other (i.e., fluorophore categories) did not. By selecting appropriate pluronic categories and adjusting the nanocapsule's concentration, we can synthesize the nanocapsules with a wide range of T_{th}s. These temperature-switchable fluorescence nanocapsules can be adopted as USF contrast agents.

Chapter 4 introduced an ICCD camera-based, time-domain USF imaging system. By implementing USF experiments on this system, we demonstrated its features and advantages for USF imaging. We also described the tradeoffs inherent in USF imaging and suggested appropriate USF imaging strategies, including balancing the tradeoffs by changing experimental parameters (i.e., CCD camera recording time, FU power, imaging depth, and gate delay of ICCD camera) and selecting an appropriate USF contrast agent.

Following up studies in Chapter 4, in Chapter 5 we investigated signal identification algorithms to improve USF imaging qualities. We described that the USF signal acquired in the ICCD camera was as a function of recording time and also as a function of 2D spatial scattering spot. Using the temporal information of a recorded USF signal, we improved the SNR of USF images by a correlation method.[65] Furthermore, we characterized the shape of the normalized USF signal's temporal information in three parameters: (1) the ascending slope; (2) the descending slope; and (3) the full-width-at-half-maximum (FWHM). By adopting an ascending-slope-weighted method, we improved the spatial resolution of USF images. Meanwhile, using the spatial information of a detected USF signal (i.e., 2D spatial scattering spot), we developed a completely new algorithm to plot a USF image: spatial back projection of USF scattering spots. By adopting this method, the spatial resolution was significantly improved. We investigated all these algorithms in one dimensional (1D) and 2D USF imaging with several imaging phantoms. Overall, Chapter 5 is focused on USF signal identification and imaging quality improvements based on USF experiments in the time-domain USF imaging system.

In Chapter 6, we successfully carried out *in vivo* 3D USF imaging in live mice via an ICCD camera-based *in vivo* USF imaging system. *In vivo* USF imaging in the mouse's glioblastoma tumor with one or multiple targets were demonstrated. Also, *in vivo* USF imaging of the mouse's spleen and liver were achieved. The results were validated by 3D co-registration with the micro-CT images. This work showed feasibility of *in vivo* USF imaging. The agent ICG-NP showed bio-stability in mouse's tumor as well as some organs (spleen and liver) and was proven a suitable USF contrast agent for *in vivo* USF imaging. Also, the camera-based *in vivo* USF imaging system demonstrated several advantages for *in vivo* USF imaging. This chapter, as pre-clinical studies of USF imaging, is an important step to push the USF technique to biomedical applications in the future.

The last chapter summarizes all the results and concludes this dissertation. Current limitations and future directions are discussed.

Chapter 2 Develop NIR P-NIPAM nanoparticle-based USF contrast agents

2.1 Introduction

The quality of a USF image depends significantly on the quality of the contrast agent.[57,63,65] Therefore, this chapter aims to upgrade (so-called new generation) one of our previously developed NIR USF contrast agents: indocyanine green (ICG)-encapsulated poly(N-isopropylacrylamide) (PNIPAM) nanoparticles (ICG-NPs). ICG-NP is a type of thermo-sensitive USF contrast agent that responds to the ultrasound-induced temperature change in the focal volume. Our previous publications have successfully demonstrated a family of ICG-NPs as an excellent USF contrast agent.[57] The ICG-NP outstands in the followings. First, ICG is an FDA-approved and commercially available NIR fluorophore.[80] Thus, it is relatively safe and cheap, and synthesizing USF contrast agents is relatively easy (no extra work is needed to synthesize fluorophores), which may increase the wide use of USF imaging. In addition, auto-fluorescence can be efficiently minimized because the excitation wavelength can be selected from 780 to 810 nm. Second, ICG-NP provides an acceptable on-to-off ratio of fluorescence intensity (I_{on}/I_{off} = ~3–9) and therefore a reasonable signal-to-noise ratio (SNR).[57] Third, the temperature threshold (T_{th}) at which to switch on ICG can be accurately controlled from room temperature (for *in vitro* studies) to the one above body temperature (>37 °C for *in vivo* studies). Fourth, the temperature transition bandwidth (T_{BW}) is narrow (generally ~5 °C); thus the switching efficiency is high.[57]

However, our previously developed ICG-NP (so-called first-generation ICG-NP) is also limited.[57] First, the shelf life (in terms of the temperature-switching property) is less than 1 month (stored at 4 °C) and thus it is difficult to store for long-term use. Second, the first-generation ICG-NP is lack of functional groups (such as carboxyl or amino) on its nanoparticle. Thus, the first-generation ICG-NP is limited for molecular imaging. In this study, we developed two new protocols that differ from the previous one, which successfully address these limitations. In addition, we also demonstrated the effect of the switching threshold (T_{th}) of ICG-NPs and background temperature on USF images, which is an important step towards future *in vivo* studies.

2.2 Methods

2.2.1 Chemical materials

N-isopropylacrylamide (NIPAM), acrylamide (AAm), ammonium persulfate (APS), 4-4'-Azobis(4-cyanopentanoic acid) (ACA), sodium dodecyl sulfate (SDS), N,N,N',N'-tetramethyl ethylene diamine (TEMED), N,N'-methylenebisacrylamide (BIS), N-tert-butylacrylamide (TBAM), succinic anhydride, Pluronic F127, dimethyl sulfoxide (DMSO) and indocyanine green (ICG) were purchased from Sigma-Aldrich (St. Louis, MO, USA). Pluronic F98 Pastille was purchased from BASF Corporation (Vandalia, IL, USA). All chemicals are used as purchased without further purification.

2.2.2 Synthesis protocols

2.2.2.1 Synthesis protocols of carboxylized pluronic F127

Pluronic F127 (8.5 g, 0.68 mmol) was dissolved in DMSO in a 250 mL 3-neck flask. The succinic anhydride (0.34 g, 3.4 mmol) in 5-fold excess was then added dropwise into the Pluronic F127/DMSO solution. The mixture was stirred at 60 °C for 24 hours under nitrogen atmosphere. The final product was collected after dialysis in distilled water for 3 days and lyophilization for 2 days. The chemical structure of synthesized carboxylized Pluronic F127 was confirmed by H^1 NMR (D_2O, 300 MHz) and ATR-FTIR.

2.2.2.2 Synthesis protocols of three different types of ICG-encapsulated P-NIPAM nanoparticles

Protocol A is the first-generation ICG-NP developed in our previous work.[57] Basically, 0.6822g NIPAM, 0.0131g BIS and 0.0219g SDS were dissolved with 50 mL de-ionized water in a 250 mL Schlenk tube, followed by nitrogen bubble purging for 10 minutes. AAm or TBAm was added by different ratio with NIPAM (i.e., NIPAM: TBAm = 185:15; pure NIPAM; NIPAM: AAm = 90:10; NIPAM: AAm = 86:14) to adjust the T_{th} (i.e., LCST) of NPs. 0.0034g ICG, 0.039g APS, and 51 µL TEMED were added into the tube, and then the tube was vacuumed and nitrogen-purged alternately for three times to give a nitrogen-protected environment for reaction. The reaction was carried out at room temperature for 4 hours, and stopped by exposing to air by loosening the valve. The sample was dialyzed in 3-liter deionized water using a 10-kDa molecular weight cut-off membrane for 3 days to remove extra unreacted materials. The first-generation ICG-NP adopts ammonium persulfate (APS) as reaction initiator. Meanwhile, it adopts sodium dodecyl sulfate (SDS) as surfactant. Therefore, we also call them ICG-encapsulated APS-initiated

SDS-surfactant poly(N-isopropylacrylamide) nanoparticles. For short, we donate them as ICG-encapsulated APS-PNIPAM-SDS NPs. In addition, we found that the ICG-encapsulated APS-PNIPAM-SDS NPs solution appears brown.

As mentioned, the first generation ICG-NP has a shelf life less than 1 month (stored at 4 °C). To overcome this issue, we developed two new synthesis protocols. In one new protocol (Protocol B, the synthesized agents are named as second generation ICG-NPs), we replaced the initiator (APS) adopted in the old protocol with a new initiator 4-4'-azobis(4-cyanopentanoic acid) (ACA) to avoid possible oxidization. The ACA works with high reaction efficiency at relatively high temperature (70 °C) with an oil bath. The oil bath makes this synthesis reaction more controllable and avoids secondary reactions before synthesis starts. Other synthesis procedures are the same as in Protocol A. The ICG-NP solution synthesized from this protocol appears pink. Because the second-generation ICG-NP adopts ACA as reaction initiator, we also call them ICG-encapsulated ACA-initiated SDS-surfactant poly(N-isopropylacrylamide) nanoparticles. For short, we donate them as ICG-encapsulated ACA-PNIPAM-SDS NPs. Similarly, ICG-encapsulated ACA-PNIPAM-SDS NPs with four different temperature-switching thresholds were synthesized.

In another new protocol (Protocol C, the synthesized agents are named as third generation ICG-NPs), instead of SDS in Protocol A and B, a new surfactant Pluronic F98 (0.329 g) or carboxylated Pluronic F127 (0.3164 g) is used. The reaction was carried out at 70 °C overnight with the initiator ACA, same as the procedure in Protocol B. The quantity of monomer NIPAM is doubled. Other synthesis procedures are the same as in Protocol A. The synthesized ICG-NP solution appears purple. Because the third-generation ICG-NP adopts ACA as reaction initiator, and meanwhile, it adopts Pluronic F98 or carboxylized Pluronic F127 as new surfactant, we also call them ICG-encapsulated ACA-initiated Pluronic-surfactant poly(N-isopropylacrylamide) nanoparticles. For short, we donate them as ICG-encapsulated ACA-PNIPAM-Pluronic NPs: ICG-encapsulated ACA-PNIPAM-PF98 NPs or ICG-encapsulated ACA-PNIPAM-cPF127 NPs. The hydroxyl groups on Pluronic F98 or the carboxyl groups on carboxylized pluronic F127 can be used for conjugation with other targeting moieties such as peptides, proteins or antibodies for the purpose of molecular targeting in the future.

2.2.2.3 Sample configuration protocol of silicon phantoms and tissue phantoms

The silicone kit was purchased from Factor II Inc. (VST-50: VerSilTal Silicone Elastomer). The kit includes two major components: silicone elastomer and catalyst. First, 1.33 mg titanium dioxide (TiO_2) was dissolved in 2 mL silicone catalyst. Then, it was mixed with 20 mL silicone elastomer. TiO_2 functions light scatters in the silicone phantom and the estimated absorption coefficient $\mu_a = 0.03$ and reduced scattering coefficient $\mu_s' = 3.5$ cm^{-1}.[65,81] The mixture was poured into a small plastic container and a silicone tube was inserted through the wall of container at an appropriate depth. The container was placed into a vacuum to remove small bubbles inside the silicone. Then, the silicone phantom was solidified at room temperature (for about 12 hours). Finally, the container was peeled off and the silicone phantom was ready to use. The porcine muscle tissue sample was prepared as follows. A silicone tube was carefully inserted into a piece of porcine muscle tissue with a thickness of 10 mm. Both the top and bottom sides of the porcine tissue were covered with ultrasound jell (01-08, AQUASONIC® 100, Parker Laboratories Inc., Fairfield, New Jersey, USA) to maintain appropriate ultrasound coupling. A piece of transparent parafilm (PM-992, BEMIS Company Inc. Neenah, WI, USA) was used to wrap the tissue and separate the sample from water to enable the tissue to maintain a natural status for a long time during experiments without drying from air exposure or degrading from water exposure.

2.2.3 Fluorescence intensity measurement of contrast agents as a function of temperature

We adopted the same system as in our previous study for measuring the fluorescence intensity of the ICG-NPs as a function of temperature.[63] Briefly, a sub-nanosecond pulsed and nitrogen-pumped dye-laser (peak wavelength: 775 nm) was filtered by a band-pass filter (749/789 nm) and used as the excitation source. An optical alignment system was adopted to collimate the fluorescence light and two 830-nm long-pass filters were used to block the excitation light. A photomultiplier tube (PMT) was adopted as the detector and a multichannel oscilloscope for data acquisition. 3 mL ICG-NP solutions were prepared in a quartz cuvette submerged in a water bath via a small transparent glass container. The water temperature is controlled via a temperature controller, a heater, and a temperature detection probe.

2.2.4 Fluorescence lifetime measurement

Fluorescence lifetime of ICG-NPs was measured via a gated ICCD camera system synchronized with a pico-sec laser in a customized inverted microscope system. The width of the impulse response function (IRF) of the ICCD camera system with the pico-second pulsed laser was ~250 ps. The measured ICG fluorescence signal was then de-convolved with the IRF to calculate the fluorescence lifetime of the ICG-NPs. To study whether the fluorescence lifetime of the ICG-NPs changes with temperature, the experiments were conducted both at room temperature ($<T_{th}$, ~25 °C) and high temperature ($>T_{th}$, ~50 °C). Data of the ICG-NPs fluorescence lifetime is shown in Table 2.1.

2.3 Results

2.3.1 ICG-encapsulated ACA-PNIPAM-SDS NPs with four LCSTs

The USF mechanism of the contrast agents has been discussed in our previous work.[57,63] Briefly, ICG were encapsulated into thermo-sensitive nanoparticles synthesized using thermo-sensitive polymers (PNIPAM). The ICG-NPs exhibit switch-like fluorescence intensity as a function of temperature. The switching transition between the two states (off and on) is reversible and repeatable.[57] Thus, if a high intensity focused ultrasound (HIFU) can control the tissue temperature in its focal area, we can use ultrasound to switch on the fluorescence emission. Figure 2.1 shows the normalized fluorescence intensity as a function of temperature of ICG-encapsulated ACA-PNIPAM-SDS NPs with four LCSTs (Protocol B, the second generation ICG-NPs). Like the temperature thresholds of first-generation ICG-NP,[57] the four temperature thresholds are 26, 30, 36, and 40 °C, respectively, which are suitable for both *ex vivo* (such as 26 °C) and *in vivo* (such as 40 °C) USF imaging.

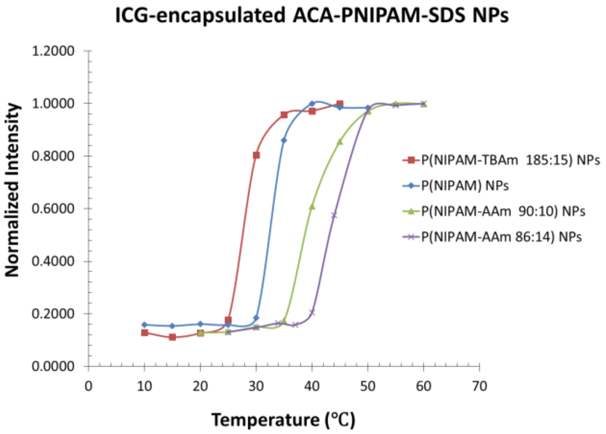

Figure 2.1 Normalized fluorescence intensity of the four ICG-encapsulated ACA-PNIPAM-SDS NPs with four LCSTs as a function of temperature.[64]

2.3.2 Shelf life studies of ICG-NPs in terms of USF switching properties

As mentioned, we developed the first generation ICG-NPs (Protocol A, ICG-encapsulated APS-PNIPAM-SDS NPs) for USF imaging in our previous work.[57] As described in the *Methods*, by adjusting the thermo-sensitive polymer components (NIPAM, TBAm, and/or AAm) and their ratios, the temperature threshold of ICG-NPs can be controlled. The following four ICG-NPs were synthesized and their temperature thresholds were found to be around 28, 31, 37, and 41 °C, respectively: (1) ICG-encapsulated P(NIPAM-TBAm 185:15) NPs, (2) ICG-encapsulated PNIPAM NPs, (3) ICG-encapsulated P(NIPAM-AAm 90:10) NPs, and (4) ICG-encapsulated P(NIPAM-AAm 86:14) NPs.[57] While all these agents show excellent temperature-switching properties, we found that their shelf life is less than 4 weeks (stored at 4 °C). As one example, Figure 2.2 (a) shows the switching property of ICG-encapsulated P(NIPAM-TBAm 185:15) NPs (measured at 1 and 4 weeks after the sample was synthesized). Clearly, the sample still exhibited an excellent switching property 1 week after the synthesis (with I_{on}/I_{off} = ~4.0). However, the agent degraded after 4 weeks because the I_{on}/I_{off} was reduced to ~2.0. Moreover, the fluorescence intensity reduced significantly under the same experimental condition. As mentioned, we found that the first-generation ICG-NP solution appears brown. The brown color is likely due to ICG oxidization during the synthesis because the reaction initiator APS and tetramethylethylenediamine (TEMED) serve as strong oxidizers to decompose alkene structures in ICG.[82] This may be the major factor in its short shelf life in terms of the temperature-switching property.

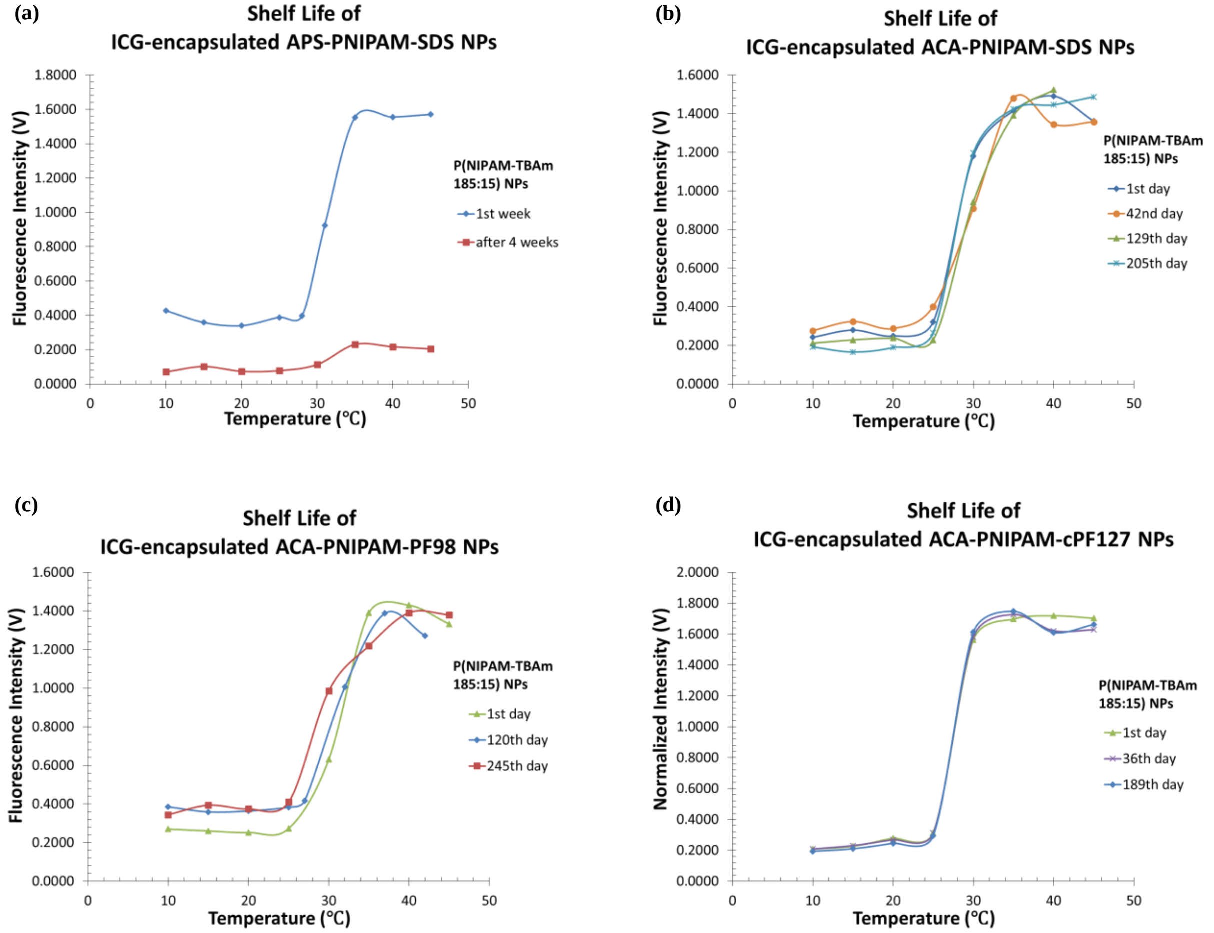

Figure 2.2 (a) Fluorescence intensity of the ICG-encapsulated APS-PNIPAM-SDS NPs nanoparticles as a function of temperature at different days (the 1st day and over 4 weeks) after the synthesis. (b) Fluorescence intensity of the ICG-encapsulated ACA-P(NIPAM-TBAm 185:15)-SDS NPs as a function of temperature at different days (the 1st day, 129th day and 205th day) after the synthesis. (c) Fluorescence intensity of the ICG-encapsulated ACA-P(NIPAM-TBAm 185:15)-PF98 NPs as a function of temperature at different days (1st day, 120th day and 245th day) after the synthesis. (d) Fluorescence intensity of the ICG-encapsulated ACA-P(NIPAM-TBAm 185:15)-cPF127 NPs as a function of temperature at different days (1st day, 36th day, 189th day) after the synthesis. [64]

As described in the *Methods*, in developing the second generation ICG-NPs (Protocol B, ICG-encapsulated ACA-PNIPAM-SDS NPs), we addressed the short shelf life issue by replacing the initiator APS with ACA to avoid possible oxidization. We found that the shelf life of the second-generation ICG-NP has significantly improved. As one example, Figure 2.2 (b) shows the temperature-switching properties of the ICG-encapsulated ACA-P(NIPAM-TBAm 185:15)-SDS NPs at three different time points: 1, 129, and 205 days after the sample was synthesized (stored at 4 °C). Clearly, the switching properties remain similar after 205 days ($I_{on}/I_{off} = 6.0$ on the 1st day and $I_{on}/I_{off} = 5.4$ on the 205th day); meanwhile, fluorescence intensity is not reduced, which indicates that this ICG-NP solution is more stable and suitable for long-term storage. Similar results are also found for the other ICG-encapsulated ACA-PNIPAM-SDS NPs (with T_{th}s of 30, 36, and 40 °C; data not shown).

Similarly, the third-generation ICG-NPs (Protocol C, ICG-encapsulated ACA-PNIPAM-PF98 NPs or ICG-encapsulated ACA-PNIPAM-cPF127 NPs) are also very stable. As an example, Figure 2.2 (c) shows the temperature-switching properties of the ICG-encapsulated ACA-P(NIPAM-TBAm 185:15)-F98 NPs at three different time points: 1, 120, and 245 days after the sample was synthesized (stored at 4 °C). The switching properties remain similar after 245 days ($I_{on}/I_{off} = 4.9$ on the 1st day and $I_{on}/I_{off} = 4.1$ on the 245th day); meanwhile the fluorescence intensity does not decrease, indicating that this ICG-NP solution is also suitable for long-term storage. Figure 2.2 (d) shows similar results of the ICG-encapsulated ACA-P(NIPAM-TBAm 185:15)-cPF127 NPs at three different time points: 1, 31, and 189 days after the sample was synthesized (stored at 4 °C).

Table 2.1 summarizes the performance of the three different types of ICG-NPs with (1) laser excitation wavelength λ_{ex} (nm) and the wavelength of the adopted fluorescence emission filter λ_{em} (nm), (2) the fluorescence intensity ratio between on and off states (I_{on}/I_{off}), (3) the temperature threshold to switch on fluorescence (T_{th}), (4) the fluorescence lifetime ratio between on and off states (τ_{on}/τ_{off}) and the fluorescence lifetime of on states (τ_{on}), (5) the temperature transition bandwidth (T_{BW}), and (6) their shelf lives. The shelf life data in Table 2.1 represent the longest time that we could measure after the synthesis of the sample when preparing this paper, but the shelf life could be longer.

Table 2.1[64]

	$\lambda_{ex}/\lambda_{em}$ (nm)	I_{on}/I_{off}	T_{th} or LCST (°C)	τ_{on}/τ_{off} τ_{on} (ns)	T_{bw} (°C)	Shelf-life
ICG-encapsulated APS-PNIPAM-SDS NPs	775nm/2×830nm LP	~ 4	~28 °C	~ 3.1 ~ 0.50 ns	~ 5 °C	< 30 days
ICG-encapsulated ACA-PNIPAM-SDS NPs	775nm/2×830nm LP	~ 6	~26, 30, 36, 40 °C	~ 3.1, 2.6, 2.6, 2.4 ~ 0.45, 0.49, 0.40, 0.40 ns	~ 5-8 °C	> 180 days for all LCSTs
ICG-encapsulated ACA-PNIPAM-PF98 NPs	775nm/2×830nm LP	~ 5	~26 °C	~ 2.4 ~ 0.48 ns	~ 8 °C	>180 days
ICG-encapsulated ACA-PNIPAM-cPF127 NPs	775nm/2×830nm LP	~ 5	~26 °C	~ 3.0 ~ 0.57 ns	~ 5 °C	>180 day

2.3.3 Shelf life studies of ICG-NPs in terms of their performance in USF imaging

To investigate whether the ICG-NPs can be used for USF imaging 6 months after their synthesis, we carried out USF imaging at different time points after USF contrast agents are synthesized. A tissue-mimic silicone phantom was adopted as a target. Figure 2.3 (a) shows the sample configuration. The thickness of the phantom is 10 mm (along the z-axis) and the width is 40 mm (along the x-axis). A silicone tube (with an inner diameter of 0.76 mm) is embedded in the silicone phantom (along the y-axis) at a depth of ~5 mm to simulate a blood vessel. Titanium dioxide (with a concentration of 0.06 mg/mL) is uniformly dissolved in the silicone phantom to make it a scattering medium ($\mu_a = 0.03$; $\mu_s' = 3.5\ cm^{-1}$).[65,81] The *Methods* section describes details of the sample configuration protocol. To image this tube, it was filled, respectively, with the aqueous solution of the three types of ICG-encapsulated P(NIPAM-TBAm 185:15) NPs (i.e., APS-PNIPAM-SDS NPs, ACA-PNIPAM-SDS NPs, ACA-PNIPAM-PF98 NPs). We adopted the USF imaging system that we had used in our previous publication.[65]

Figure 2.3 (b) shows the USF image of the tube on the x-y plane acquired from the ICG-encapsulated APS-P(NIPAM-TBAm 185:15)-SDS NPs (i.e., the first-generation ICG-NPs) right after the agents were synthesized (defined as the 1st day). The HIFU transducer has a 2.5 MHz central frequency (H-108, Sonic Concepts Inc, Bothell, WA, USA). The peak-to-peak driving voltage (V_{pp}) from the function generator is 120 mV and is further amplified 50 dB via a power amplifier (325LA, E&I, Rochester, NY, USA) before it is applied to the transducer. The HIFU exposure time is 300 ms. The FWHM of the image is 1.70 mm and the SNR of the image is 109 (SNR is defined as the ratio of the peak USF signal to the standard deviation of the background noise). After 4 weeks, we conducted the same experiment using the same batch agent. We found the quality of the USF image unacceptable (the image is not shown).

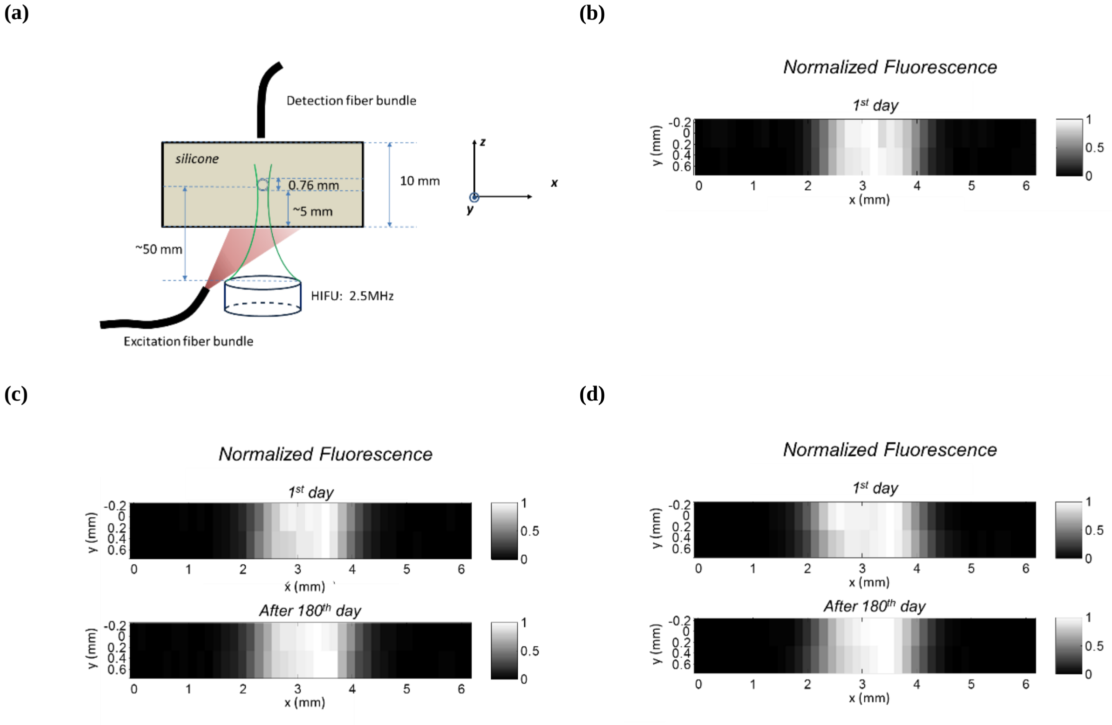

Figure 2.3 (a) The sample configuration, including the silicone phantom, the silicone tube (0.76 mm), the excitation and detection fiber bundle and the HIFU transducers (2.5 MHz). (b) USF image of the silicone phantom imbedded with the silicone tube (0.76 mm) using the ICG-encapsulated APS-P(NIPAM-TBAm 185:15)-SDS NPs (LCST = 28 °C) on 1st day after synthesis. (c) USF image of the silicone phantom imbedded with the silicone tube (0.76 mm) using ICG-encapsulated ACA-P(NIPAM-TBAm 185:15)-SDS NPs (LCST = 26 °C). The top sub-image used the NPs on 1st day after synthesis, the bottom sub-image used the NPs after 180th day. (d) USF image of the silicone phantom imbedded with the silicone tube (0.76 mm) using ICG-encapsulated ACA-P(NIPAM-TBAm 185:15)-PF98 NPs (LCST=26 °C). The top sub-image used the NPs on 1st day after synthesis, the bottom sub-image used the NPs after 180th day. The USF images were carried out and normalized based on the data processing method in our previous work. [64]

Figure 2.3 (c) shows the USF images of the same silicone phantom using the ICG-encapsulated ACA-P(NIPAM-TBAm 185:15)-SDS NPs (i.e., the second-generation ICG-NPs). The top and bottom images represent, respectively, the USF images acquired on the 1st day and after the 180th day after the agent was synthesized under the same experiment. The same HIFU transducer was used (2.5 MHz). However, the driving voltage from the function generator was slightly reduced (V_{pp} = 90 mV) while the HIFU exposure time remained 300 ms. The FWHMs of the top and bottom USF images are 1.70 and 1.64 mm, respectively, and the corresponding SNRs are 154 and 178.5. Similar results were achieved for the the ICG-encapsulated ACA-P(NIPAM-TBAm 185:15)-PF98 NPs (i.e., the third-generation ICG-NPs) and shown in Figure 2.4 (d). The experimental parameters remained the same as those for the above two experiments except that the HIFU driving voltage was V_{pp} = 110 mV. The FWHMs of the top and bottom

USF images are 1.70 and 1.90 mm, respectively, and the corresponding SNRs are 304 and 292. Figure 2(c) and (d) indicate that the qualities of both the ICG-encapsulated ACA-P(NIPAM-TBAm 185:15)-SDS NPs and the ICG-encapsulated ACA-P(NIPAM-TBAm 185:15)-PF98 NPs remain high and that both can be used for USF imaging even after 180 days. Table 2.2 provides a summary of USF imaging performance of the three ICG-NPs.

Table 2.2[64]

	HIFU central frequency & Power	**Target size & Imaging Depth**	**Scattering Medium**	**SNR**	**FWHM(mm)**	**Shelf-life**
ICG-encapsulated APS-PNIPAM-SDS NPs (LCST=28 °C)	2.5 MHz 120 mV	760 um & 10 mm	TiO2 Silicone Phantom	~ 109	~ 1.70	< 30 days
ICG-encapsulated ACA-PNIPAM-SDS NPs (LCST=26 °C)	2.5 MHz 90 mV	760 um & 10 mm	TiO2 Silicone Phantom	~ 166	~ 1.67	> 180 days
ICG-encapsulated ACA-PNIPAM-F98 NPs (LCST=26 °C)	2.5 MHz 110 mV	760 um & 10 mm	TiO2 Silicone Phantom	~ 298	~ 1.80	> 180 days

2.3.4 Studies of the effect of the temperature-switching threshold and the background temperature on USF imaging

To investigate the effect of the temperature-switching threshold (T_{th}) and the background temperature (T_{BG}) on USF imaging, we conducted the following experiments. First, we synthesized two ICG-encapsulated ACA-PNIPAM-SDS NPs contrast agents with LCST = 26 °C (i.e., ICG-encapsulated ACA-P(NIPAM-TBAm 185:15)-SDS NPs) and 40 °C (i.e., ICG-encapsulated ACA-P(NIPAM-AAm 85:15)-SDS NPs). Second, we made a tissue phantom by inserting a small silicone tube (with an inner diameter of 0.31 mm) into a piece of porcine muscle tissue (with a thickness of 10 mm). Figure 2.4 (a) shows the sample configuration. Third, the two ICG-NP solutions were injected, respectively, into the tube for USF imaging. Because the inner diameter of the tube (0.31 mm) is smaller than the previous one (0.76 mm), a relatively higher spatial resolution is preferable. Therefore, we replaced the previous 2.5-MHz HIFU transducer with a 15-MHz HIFU transducer (H-202, Sonic Concepts Inc, Bothell, WA, USA), thus reducing the lateral acoustic focal size from ~420 to ~100 microns. In addition, we used a temperature controller (with a heater and a temperature detection probe) to control the temperature of the water bath in which the phantom was submerged. Also, we used a magnetic stirrer (11-100-16S, Fisher Scientific, USA) along with a long magnetic bar to stir the whole water in the tank to stabilize the water temperature. Other parts of the USF system remained the same. Finally, we imaged the tube with the USF system at two different background temperatures by controlling the temperature of the water bath: 23.5 and 37.2 °C. The former and the latter simulate *ex vivo* and *in vivo* background temperatures, respectively.

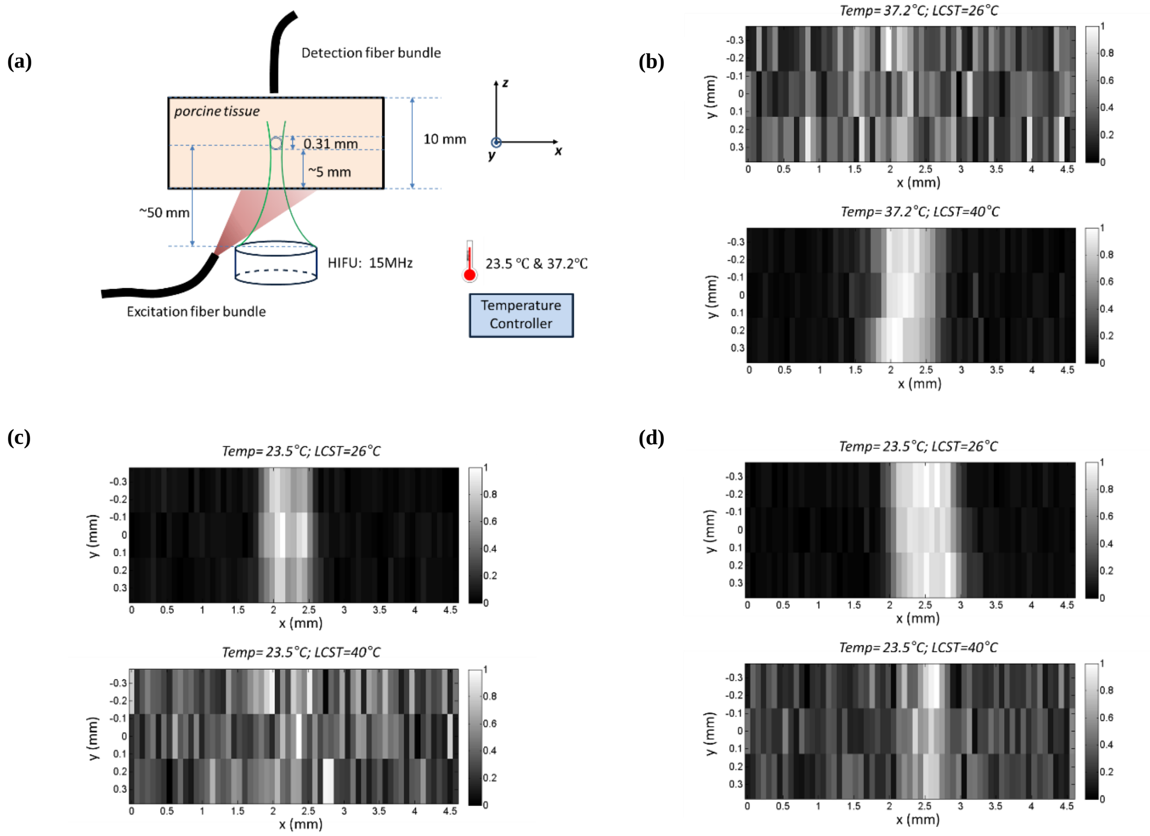

Figure 2.4 (a) the sample configuration, including the porcine tissue phantom, the silicone tube (0.31 mm), the excitation and detection fiber bundle, the HIFU transducers (15 MHz) as well as the temperature controller. The whole sample was merged into a big water tank and the sample temperature was controlled by water bath with the temperature controller. (b) USF image of the sample with experimental temperature at 37.2 °C. ICG-encapsulated ACA-PNIPAM-SDS NPs were used as the contrast agents; the top sub-image shows the USF image using ICG-encapsulated ACA-P(NIPAM-TBAm 185:15)-SDS NPs with LCST=26 °C, the bottom sub-image shows the USF image using ICG-encapsulated ACA-P(NIPAM-AAm 85:15)-SDS NPs with LCST=40 °C. The HIFU transducer driving voltage is 500 mV with a duration of 200 ms (single burst). (c) USF image of the same experimental condition as (b), except that the experimental temperature is 23.5 °C and the HIFU transducer driving voltage is 350 mV with a duration of 200 ms (single burst). (d) USF image of the same experimental condition as (b), except that the experimental temperature is 23.5 °C and the HIFU transducer driving voltage is 500 mV with a duration of 200 ms (single burst).   The USF images were carried out and normalized based on the data processing method in our previous work. [64]

Figure 2.4 (b) shows the USF images acquired at the background temperature of 37.2 °C from the two ICG-encapsulated ACA-PNIPAM-SDS NPs with LCST = 26 °C (top) and LCST = 40 °C (bottom). The driving voltage of the 15-MHz HIFU transducer from the function generator was V_{pp} = 500 mV, while the exposure time was 200 ms. The USF image clearly shows the tube filled with ICG-NP agent with LCST = 40 °C (the bottom figure). The FWHM of the image is 0.868 ± 0.074 mm and the SNR is 37.70 ± 2.69. However, the tube cannot visualized from the USF image when it was filled with ICG-NP agent with LCST = 26 °C (the top figure). We expected this result because the 37.2 °C background temperature may already completely switch on the ICG-NPs with LCST = 26 °C (i.e., the background temperature is above the temperature-switching threshold). Therefore, ICG-NPs do not respond further to an ultrasound-induced temperature increase in tissue. On the other hand, the 37.2 °C background temperature is not high enough to switch on the ICG-NPs with LCST = 40 °C (i.e., the background temperature is below the temperature-switching threshold) and the ICG-NPs remain intact. Accordingly, when ultrasound induces the tissue temperature above the threshold in its focal region, ICG-NPs are switched on and therefore the tube can be clearly imaged via USF. This result provides an excellent model for future *in vivo* studies because the background temperature of a living body (either vertebrate animals or human) is around 37 °C.

Similarly, we performed another experiment at room temperature to simulate an *ex vivo* scenario. The background temperature of the water bath was 23.5 °C. In this experiment the HIFU driving voltage from the function generator was V_{PP} = 350 mV and the exposure time remained 200 ms. Figure 2.4 (c) shows the USF images of the tube filled with ICG-NPs with LCST = 26 °C (top) and LCST = 40 °C (bottom). The tube is clearly imaged when filled with agents with low LCST (26 °C). The FWHM is 0.701 ± 0.012 mm and the SNR is 34.04 ± 2.02. However, the tube filled with agents with high LCST (40 °C) cannot be visualized using current parameters. This result indicates that the final temperature in the ultrasound focal region (the sum of the background temperature and the ultrasound-induced temperature) is high enough to switch on a significant number of ICG-NPs that have a low temperature-switching threshold (26 °C). However, the final temperature is still low and unable to switch on a significant number of ICG-NPs that have a relatively high temperature-switching threshold (40 °C). To switch on these high LCST ICG-NPs, a higher focal temperature is needed. To validate this idea, we increased the HIFU driving voltage from 350 mV to 500 mV while the exposure time remained 200 ms. We expected that the final temperature in the focal region should be increased. Figure 2.4 (d) shows the results. As the bottom image shows, the tube filled with high LCST agents can be roughly visualized (compared with the bottom image in Figure 2.4 (c)), although the image is still noisy. This indicates that ultrasound has switched on some number of ICG-NPs, which validates the assumption. Furthermore, the SNR of the USF image acquired from the low LCST agents (the top image) is increased to 47.66 ± 1.41 (compared with 34.04 ± 2.02 of the one in Figure 2.4 (c)), indicating that more ICG-NPs were switched on compared with those in Figure 2.4 (c) because HIFU induced higher temperature. In addition, the FWHM of this image is 0.927±0.023 mm, wider than the one in Figure 2.4 (c) (0.701 ± 0.012 mm). This is understandable because the higher the temperature that ultrasound induces, the larger the thermal volume is, therefore the lower the spatial resolution is. Table 2.3 summarizes the details of this study.

Table 2.3[64]

	HIFU central frequency & Power	Target size & Imaging Depth	Scattering Medium	SNR	FWHM (mm)	Sample Temperature (°C)
ICG-encapsulated ACA-PNIPAM-SDS NPs (LCST=26 °C)	15 MHz 350 mV	310 um & 10 mm	Porcine Tissue Phantom	~ 34.0	~ 0.70	23.5
ICG-encapsulated ACA-PNIPAM-SDS NPs (LCST=26 °C)	15 MHz 500 mV	310 um & 10 mm	Porcine Tissue Phantom	~ 47.6	~ 0.93	23.5
ICG-encapsulated ACA-PNIPAM-SDS NPs (LCST=40 °C)	15 MHz 500 mV	310 um & 10 mm	Porcine Tissue Phantom	~ 37.7	~ 0.87	37.2

2.4 Discussion

High-resolution USF imaging in centimeter-deep tissues is a new technology, highly dependent on the contrast agents adopted. The ICG-NPs are one family of excellent USF contrast agents because they have reasonable I_{on}/I_{off}, NIR excitation and emission spectra, narrow temperature transition bandwidths, and controllable temperature-switching thresholds. In this work, we addressed three additional challenges for this family of contrast agents, further reducing the application barriers of this technology.

2.4.1 Long-term stability of USF contrast agents

First, we developed two new protocols that significantly increased the stability of USF switching properties. The shelf life of ICG-NP was increased from less than one month to longer than 6 months. We expect that the shelf life of both the two new ICG-NPs (i.e., ICG-encapsulated ACA-PNIPAM-SDS NPs and ICG-encapsulated ACA-PNIPAM-Pluronic NPs) will be even longer than one year because we do not see the performance degradation in this work. Long-term stability of USF contrast agents is highly desirable for some experiments. For example, when conducting comparative longitudinal studies such as monitoring disease development and treatment evaluation over a long period (usually > 6 months), adopting USF contrast agents synthesized from the same batch can avoid those unwanted variations that originate from the different batches of production. Meanwhile, fast degradation will make it challenging or sometimes even impossible to maintain contrast agents with same parameters and stable properties. In addition, stable contrast agents can save a large amount of effort (such as time and cost) by avoiding having to repetitively make new batch agents to replace quickly degraded agents. This is the key to reducing the cost of agent and further increasing its commercialization potential. Finally, a long-term stable USF contrast is necessary for applications that use USF imaging to monitor implanted medical device, in which USF contrast agents are sealed into the medical device for long-term use (up to years), making USF performance stability extremely important.

2.4.2 Functionalization of USF contrast agents

Second, the success of replacing the original surfactant (SDS) of our previous ICG-NPs with Pluronic F98 or carboxylated Pluronic F127 provides a great opportunity to functionalize ICG-NPs in future. Molecular imaging has achieved significant progress in past years. Functionalizing the surface of contrast agents is an important future goal for conducting USF molecular imaging in deep tissue with high resolution. Unlike the sodium sulfate (SDS) end-groups, the two hydroxyl end-groups (F98) or the two carboxyl end-groups (carboxylated F127) are exposed to the surrounding hydrophilic aqueous solution and show potential to react with other molecules containing amine or carboxyl groups. Thus, these function groups could possibly be conjugated with targeting moieties such as antibodies and ligands to target specific molecules or proteins.

2.4.3 An appropriate temperature-switching threshold of the contrast agents for USF imaging

In addition, we demonstrated for the first time the effect of the temperature-switching threshold (T_{th}) and the background temperature (T_{BG}) on USF imaging. For ICG-NP based contrast agents, the results indicate that USF imaging can be successfully or efficiently conducted when Tth is controlled slightly above T_{BG} (the bottom figure in Figure 2.4 (b); the top figures in Figure 2.4 (c) and Figure 2.4 (d)). In contrast, when T_{th} is much higher than T_{BG}, USF imaging can fail (the bottom figures in Figure 2.4 (c)) or need stronger energy (the bottom figures in Figure 2.4 (d)). Finally, when T_{th} is well below T_{BG}, USF imaging can fail (the top figure in Figure 2.4 (b)). Based on these results, a very important indication for future *in vivo* studies is that the T_{th} of the ICG-NP based contrast agents should be controlled ~38-40 °C, which is slightly above the body temperature (37 °C). We will investigate this in future research.

2.5 Conclusion

In conclusion, two new protocols of ICG-P(NIPAM) nanoparticles were developed for USF contrast agents with long-term stability, adjustable LCST, and functionalization. The shelf life of these new generation ICG-NPs developed in this study is much longer (>6 months) than that of the first generation (<1 month), and their quality remains good as of this writing. We have also synthesized the new ICG-NPs with conjugation-functional groups (hydroxyl or carboxyl), which can be used for molecular imaging in the future if they are attached with a targeting moiety. Finally, we investigated the effect of the temperature-switching threshold of the agent and the background temperature on USF imaging. Maintaining the agents' temperature threshold slightly above the background temperature is necessary for conducting USF imaging successfully and efficiently. Therefore, for *in vivo* USF imaging, the temperature threshold of the contrast agents should be controlled slightly above the body temperature of 37 °C.

Chapter 3 Develop NIR nanocapsule-based USF contrast agents

3.1 Introduction

NIR environment-sensitive fluorophores are highly desired for many biomedical applications because of its non-invasive operation, high sensitivity and specificity, non-ionizing radiation and good penetration in biological tissue.[83-85] When the fluorophores are appropriately encapsulated in or conjugated with some thermal-sensitive polymers, they could become excellent temperature-switchable fluorescence contrast agents. In this chapter, we synthesized, characterized, and selected a series of temperature-switchable nanocapsules, based on two series of novel NIR fluorophores (ADP and ZnPc) and four pluronic polymers. The ADP fluorophores[66,86] include ADP, ADPCA, ADP(OH)$_2$-Top, ADP(OH)$_2$-Bottom, and the ZnPc fluorophores include ZnPc, ZnttbPc, ZnHFPc. The polymers include pluronic F127, pluronic F98, pluronic F68, and pluronic F38. Encapsulating each fluorophore in each polymer by sonication, we synthesized a series of nanocapsules which might show their fluorescence intensity and/or lifetime as a switch-like function of temperature. As described in the previous chapter[63], we summarized five parameters that characterizes the performance of a temperature-switchable fluorescence contrast agent: (1) the fluorescence peak excitation and emission wavelengths (λ_{ex} and λ_{em}); (2) the fluorescence intensity ratio between its on- and off- states (I_{on}/I_{off}); (3) the fluorescence lifetime ratio between its on- and off- states (τ_{on}/τ_{off}); (4) the temperature threshold to switch on the fluorescence (T_{th}); and (5) the temperature transition bandwidth (T_{BW}). By characterization of these nanocapsules in the fluorescence intensity and lifetime measurement system[63], we selected those which have excellent thermal-switchable fluorescence properties. In addition to selecting these nanocapsules, we investigated several factors that might change their T_{th}s. The factors include 1) fluorophore categories; 2) pluronic categories; and 3) nanocapsules' concentrations. These nanocapsules can be adopted as USF contrast agents. Also, these nanocapsules can be potentially used as temperature-sensing probes. Note that a part of the experimental works described in this chapter were conducted by Mr. Zhen Wang, who worked in the same laboratory.

3.2 Methods

3.2.1 Chemical materials

ADP series fluorophores[66,86] include BF2-chelated azadipyrromethane (also called aza-BODIPY, ADP for short), aza-BODPIY-based with two cyanocinnamic acids (ADP(CA)$_2$ for short), BF2-chelated 4-[2-[3-(4-hydroxyphenyl)-5-phenyl-1H-pyrrol-2ylimino]-5-phenyl-2H-pyrrol-3-yl] phenol (ADP(OH)$_2$-Top for short), BF2-

chelated [5-(4-hydroxyphenyl)-3-phenyl-1H-pyrrol-2-yl]-[5-(4-hydroxyphenyl)-3-phenylpyrrol-2-ylidene] amine ($ADP(OH)_2$-Bottom for short).[65,66,86] They were synthesized at the Department of Chemistry, University of North Texas (Denton). ZnPc series fluorophores include zinc phthalocyanine (ZnPc), zinc 2, 9, 16, 23-tetra-tert-butyl-29H, 31H-phthalocyanine (ZnttbPc), and zinc 1, 2, 3, 4, 8, 9, 10, 11, 15, 16, 17, 18, 22, 23, 24, 25-hexadecafluoro-29H, 31H-phthalocyanine (ZnHFPc). They were purchased from Sigma-Aldrich Corporate (St. Louis, MO, USA). Tetrabutylammonium iodide (TBAI), pluronic F127, and chloroform was purchased from Sigma-Aldrich Corporate (St. Louis, MO, USA). Pluronic F98, F68, F38 were purchased from BASF Corporation (Vandalia, IL, USA). All chemicals were used as received without further purification.

3.2.2 Synthesis protocols of ADP/ZnPc encapsulated pluronic nanocapsules

5 g or 1 g pluoronic polymers (F127, F98, F68, or F38) was dissolved in 100 mL DI water (pH=8.5) to make 5% or 1% pluronic solution. ADP-series fluorophores (ADP, ADPOH_Bottom, ADPOH_Top, or ADPCA) or ZnPc-series fluorophores (ZnPc, ZnttbPc, or ZnHFPc) were selected and each was prepared to encapsulate in the nanocapsules. 0.4 mg of the ADP series fluorophore or 1.2 mg of the ZnPc series fluorophore was mixed with 4.8 mg TBAI (cosolvent) and then dissolved in 6 mL chloroform. The fluorophore solution was added dropwise to 15 mL of the pluoronic solution, with 600 rpm stirring. The mixture was then under sonication (power = 40 Watts) for 4 mins to form fluorophore-encapsulated pluoronic-based nanocapsules. The mixture was stirred at 475 rpm in chemical hood overnight until chloroform evaporated thoroughly. The solution was filtered (filter pole size: 450 μm) to purify the sample.

3.2.3 Fluorescence intensity and lifetime measurement system

The measurement system was developed in our previous work.[63] Briefly, the excitation light was from a sub-nanosecond nitrogen-pumped dye-laser (OL-4300, dye laser: OL-401, both from Optical Building Blocks Corporation, Edison, NJ, USA). The laser dye (Optical Building Blocks Corporation, Edison, NJ) was selected at OD 655 so the output central wavelength was 655 nm. The claimed laser pulse width was ~ 0.8 ns. One band-pass interference filter (center wavelength: 650 nm, bandwidth: 60 nm) was placed in front of the laser output as the excitation filter. The nanocapsule sample (volume = 3 mL) was placed in a quartz cuvette (DLC-23-Q-10, White Bear Photonics, LLC, White Bear Lake, MN, USA) and submerged in a transparent glass tank filled with water. The temperature of the water was controlled via a temperature controller (PTC10, OMEGA Engineering, Inc., Stamford, CT, USA). The laser beam illuminated the fluorescence in the cuvette and the emitted fluorescence photons were captured through an optical collimation tube at a 90-degree angle from the laser beam. The collected photons were then detected by a photomultiplier tube (PMT, H10721-20, Hamamatsu, Japan) behind the collimation tube. One band-pass interference filter (center wavelength: 711 nm, bandwidth: 25 nm) was placed in the tube as the emission filter. Finally, the signal was acquired in a multichannel GHz oscilloscope (DPO 7254, Tektronix, Beaverton, OR, USA). The fluorescence pulses from the sample were recorded at different temperatures. The peak strength of the fluorescence pulse was counted as the fluorescence intensity. The excitation laser pulse was also measured when the cuvette was filled with DI water and the emission filter was removed. We adopted the measured laser pulse as an impulse response function (IRF) of the system. At each temperature, in order to calculate the fluorescence lifetime, we de-convolved the normalized fluorescence pulse from the normalized IRF and got an exponential decay function. The decay factor in the exponential function represented an averaged fluorescence lifetime of the sample.

3.2.4 Characterization of the nanocapsules

As mentioned previously, there are five parameters that quantifies the thermal switchable properties of fluorescence from the nanocapsules. As known, their fluorescence intensity/lifetime might change as a function of temperature. Referring to Figure 1.2 in Chapter 1, typically, the fluorescence intensity and/or lifetime is weak (short) when the temperature is below the T_{th}. When the temperature rises over T_{th}, the fluorescence intensity and/or lifetime increases significantly. When the temperature rises across the T_{BW}, the fluorescence becomes stabilized again. The fluorescence intensity and lifetime ratio between its on- and off- states are termed as I_{on}/I_{off} and τ_{on}/τ_{off}. When these nanocapsules are adopted as USF contrast agents, the excellence of their performance relies in (a) NIR λ_{ex} and λ_{em}, which is mainly determined by the fluorophore: ADP and ZnPc are two series of NIR fluorophores; (b) a high I_{on}/I_{off} and a high τ_{on}/τ_{off}; (c) an adjustable T_{th}; and (d) a narrow T_{BW}. When these nanocapsules are potentially used for temperature-sensing, they should have the same (a)–(c) described above, but meanwhile should instead have (d) an adjustable T_{BW}.

3.3 Results

3.3.1 The nanocapsules’ fluorescence intensity and lifetime as a function of temperature

As described in the *Methods*, we measured the nanocapsules’ fluorescence intensity and lifetime as a function of temperature and characterized the measurement results. Figure 3.1 shows two examples. In Figure 3.1 (a), it shows the measurement of ADP encapsulated in 5% pluronic F98 nanocapsule. It has a high I_{on}/I_{off} = ~ 1845, and a high

τ_{on}/τ_{off} = 2.86 (τ_{on} = 2.11 ns), which means both its fluorescence intensity and lifetime increased significantly when the temperature rose over its T_{th}. Its T_{th} = ~ 28 °C, and T_{bw} = ~ 6 °C. Figure 3.1 (b) show the measurement of ZnttbPc in 1% pluronic F68 nanocapsule. Similarly, it also has a high I_{on}/I_{off} = ~ 16395. Differently, its fluorescence lifetime slightly changes with a temperature rise. Its τ_{on}/τ_{off} = 1.06 (τ_{on} = 3.25 ns). Its T_{th} = ~ 56 °C, and T_{bw} = ~ 15 °C. Based on the two examples, we found their I_{on}/I_{off}, T_{th}, τ_{on}/τ_{off}, and T_{bw} all varied.

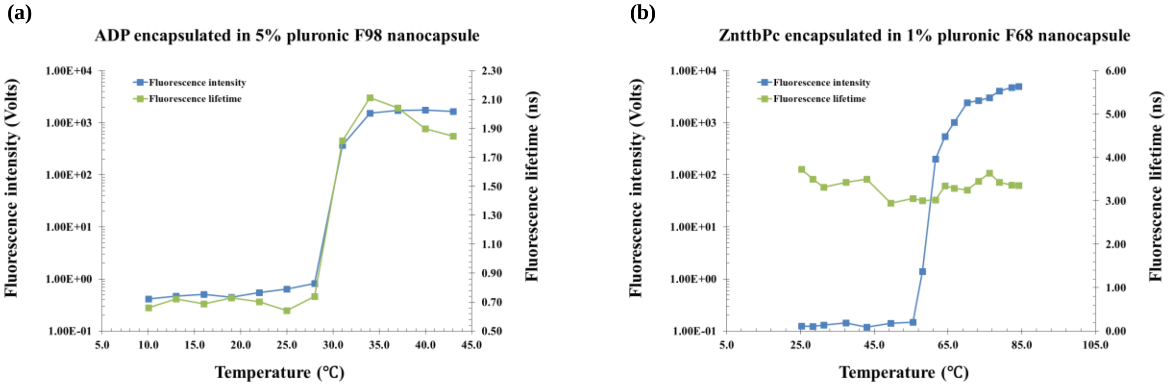

Figure 3.1 Fluorescence intensity and lifetime as a function of temperature of (a) ADP encapsulated in 5% pluronic F98 nanocapsule; and (b) ZnttbPc encapsulated in 1% pluronic F68 nanocapsule.

Characterizations of the two nanocapsules were also presented in Table 3.1. As mentioned, in this work we synthesized all the nanocapsules based on different combinations of fluorophore categories and pluronic categories as well as pluronic concentrations. Then, we characterized and selected these nanocapsules based on their thermos-switchable properties of fluorescence, from three perspectives: 1) those with a high I_{on}/I_{off}; 2) those with a high τ_{on}/τ_{off}; and 3) those with various T_{th}s. Note that some nanocapsules didn't show a thermal-switchable property (i.e., a low I_{on}/I_{off} and/or τ_{on}/τ_{off}) and thus were excluded. After selection, we studied several factors that affected the nanocapsules' T_{th}s. The results were presented and discussed in the next sections.

Table 3.1

	I_{on}/I_{off}	**T_{th} (°C)**	**τ_{on}/τ_{off}, τ_{on} (ns)**	**T_{bw} (°C)**
ADP in 5% F98 nanocapsule	1845	28	2.86, 2.11	6
ZnttbPc in 1% F68 nanocapsule	16395	56	1.06, 3.25	15

3.3.2 The fluorophore categories slightly affects the temperature threshold

In this section, we studied whether the fluorophore categories will affect the T_{th}s. Four polymer solutions were prepared based on different pluronic categories and concentrations: 1) 5% F127; 2) 5% F98; 3) 1% F68; and 4) 1% F38. In each polymer solution, different fluorophores were encapsulated and the nanocapsules were synthesized and characterized. In 1% F127 nanocapsule, four fluorophores (i.e., ADP, ADPCA, ADPOH_Bottom, and ZnttbPc) were encapsulated. Figure 3.2 (a) shows their normalized fluorescence intensity as a function of temperature. Their T_{th}s were ~ 22 °C, 22 °C, 20 °C, and 22 °C, respectively. It shows their T_{th}s were very close to each other (≤ 5 °C).

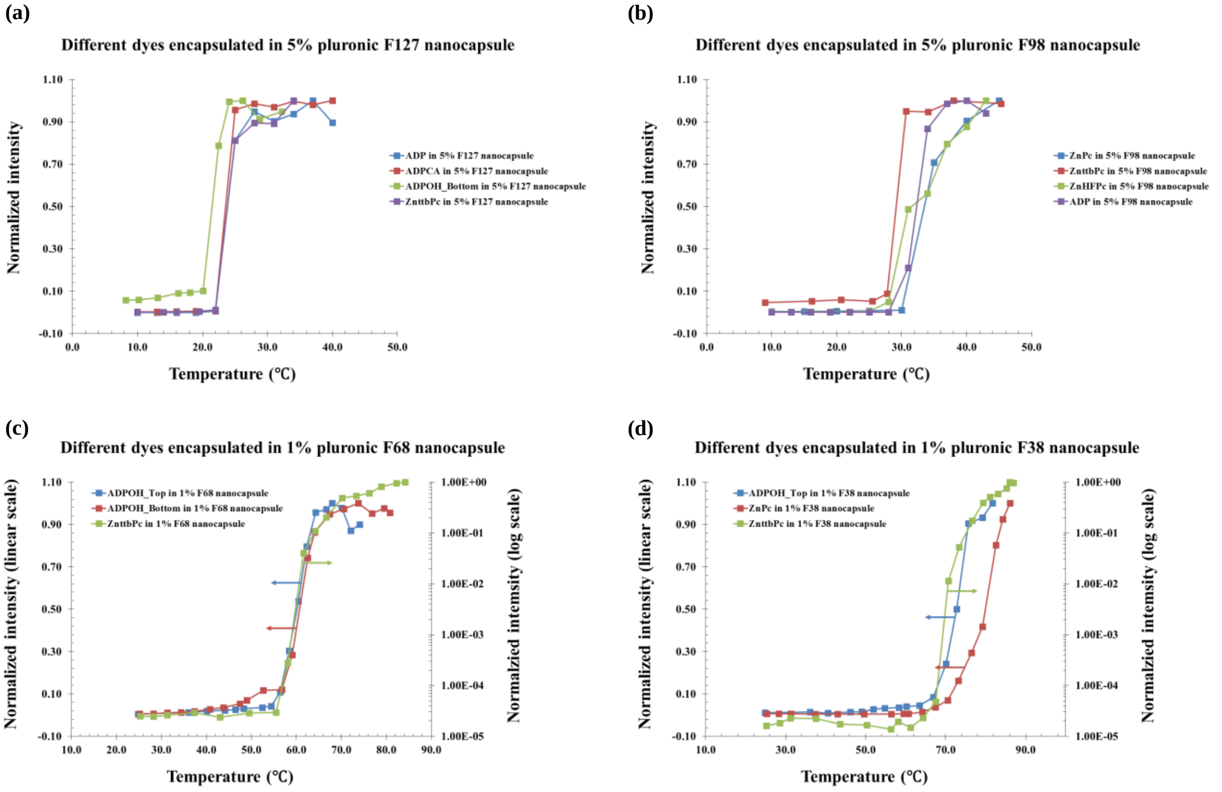

Figure 3.2 Fluorescence intensity as a function of temperature of (a) ADP, $ADP(CA)_2$, $ADP(OH)_2$_Bottom, and ZnttbPc encapsulated in 5% pluronic F127 nanocapsule; (b) ZnPc, ZnttbPc, ZnHFPc, and ADP encapsulated in 5% pluronic F98 nanocapsule; (c) $ADP(OH)_2$_Top, $ADP(OH)_2$_Bottom, and ZnttbPc encapsulated in 1% pluronic F68 nanocapsule; and (d) $ADP(OH)_2$_Top, ZnPc, and ZnttbPc encapsulated in 1% pluronic F38 nanocapsule.

Likewise, Figure 3.2 (b) shows the normalized fluorescence intensity as a function of temperature of four samples: ADP in 5% F98 nanocapsule, ZnPc in 5% F98 nanocapsule, ZnttbPc in 5% F98 nanocapsule, and ZnHFPc in 5% F98 nanocapsule. Their T_{th}s were ~ 28 °C, 30 °C, 28 °C, and 25 °C, respectively. Also, their T_{th}s were close to each other (≤ 5 °C). Similar results were also presented when different dyes were encapsulated in 1% F68 nanocapsules

(Figure 3.2 (c)) or 1% F38 nanocapsules (Figure 3.2 (d)). The T_{th}s were close to each other (≤ 5 °C) when the nanocapsules had the same pluronic category and concentration. All the nanocapsules showed excellent thermal-switchable properties of fluorescence (a high I_{on}/I_{off} and/or τ_{on}/τ_{off}). Their characterization results were summarized in Table 3.2. In this section, we conclude that the fluorophore categories slightly affected the nancapsules' T_{th}s (T_{th} difference ≤ 5 °C), when nanocapsules were synthesized based on the same pluronic solution (i.e., the same pluronic category and concentration).

Table 3.2

	I_{on}/I_{off}	**T_{th} (°C)**	**τ_{on}/τ_{off}, τ_{on} (ns)**	**T_{bw} (°C)**
ADP in 5% F127 nanocapsule	159	22	2.67, 2.69	6
ADPCA in 5% F127 nanocapsule	100	22	1.44, 1.25	3
ADPOH_Bottom in 5% F127 nanocapsule	10	20	1.14, 1.52	4
ZnttbPc in 5% F127 nanocapsule	69	22	9.69, 2.64	3
ADP in 5% F98 nanocapsule	1845	28	2.86, 2.11	6
ZnPc in 5% F98 nanocapsule	67	30	2.17, 2.44	5
ZnttbPc in 5% F98 nanocapsule	941	28	10.79, 2.55	3
ZnHFPc in 5% F98 nanocapsule	166	25	12.50, 1.61	9
ADPOH_Top in 1% F68 nanocapsule	22	54	1.48, 0.32	10
ADPOH_Bottom in 1% F68 nanocapsule	8	57	1.26, 1.38	11
ZnttbPc in 1% F68 nanocapsule	16395	56	1.06, 3.25	15
ADPOH_Top in 1% F38 nanocapsule	20	64	1.29, 0.26	12
ZnPc in 1% F38 nanocapsule	56	64	0.87, 3.17	18
ZnttbPc in 1% F38 nanocapsule	16887	64	0.92, 3.31	15

3.3.3 The temperature threshold depends on the pluronic categories

In the previous section, it also showed that when different pluronic categories were selected, the nanocapsules' T_{th}s varied significantly (by comparing the T_{th}s in Figure 3.2 (a)-(d) longitudinally). In this section, we studied whether the pluronic categories would affect the T_{th}. Thus, we encapsulated the same fluorophore in nanocapsules based on different pluronics. The nanocapsules were characterized and compared with each other. For example, Figure 3.3 (a) shows the characterization results of four samples: ADPOH_Top in 1% F127 nanocapsule, ADPOH_Top in 1% F98 nanocapsule, ADPOH_Top in 1% F68 nanocapsule, ADPOH_Top in 1% F38 nanocapsule. Based on their normalized fluorescence intensities as a function of temperature, their T_{th}s were ~ 24 °C, 34 °C, 54 °C, and 64 °C, respectively. Since the nanocapsules have encapsulated the same fluorophore (i.e., ADPOH_Top), and the pluronics' concentrations were kept the same, we concluded that the pluronic categories highly affected the nanocapsules' T_{th}s.

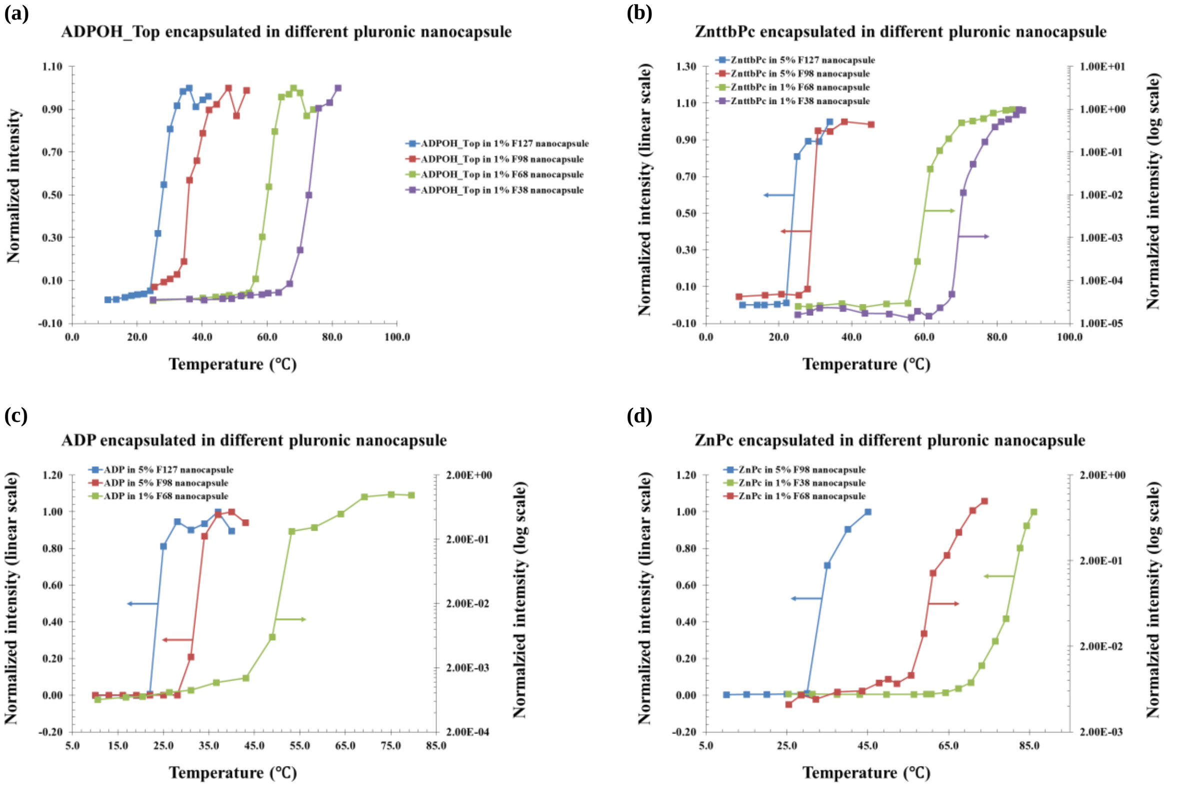

Figure 3.3 Fluorescence intensity as a function of temperature of (a) ADP(OH)$_2$_Top encapsulated in 1% pluronic F127, 1% pluronic F98, 1% pluronic F68, and 1% pluronic F38 nanocapsule; (b) ZnttbPc encapsulated in 5% pluronic F127, 5% pluronic F98, 1% pluronic F68, and 1% pluronic F38 nanocapsule; (c) ADP encapsulated in 5% pluronic F127, 5% pluronic F98, and 1% pluronic F68 nanocapsule; and (d) ZnPc encapsulated in 5% pluronic F98, 1% pluronic F68, and 1% pluronic F38 nanocapsule.

For more examples, Figure 3.3 (b)-(d) shows the similar results when a same fluorophore (i.e., ZnttbPc in Figure 3.3 (b), ADP in Figure 3.3 (c), and ZnPc in Figure 3.3 (d)) was encapsulated in nanocapsules with different pluronics. These examples indicate that the T_{th}s were affected by pluronic categories when more than one fluorophore was encapsulated. It is worth mentioning that, in these plots, some curves were presented in different scales (linear or log scale) for a better visualization, due to that the nanocapsules' I_{on}/I_{off}s varied significantly in scale (from tens to ten thousands of folds). All the nanocapsules in Figure 3.3 showed excellent thermal-switchable properties. Their characterization results were summarized in Table 3.3

Table 3.3

	I_{on}/I_{off}	T_{th} (°C)	τ_{on}/τ_{off}, τ_{on} (ns)	T_{bw} (°C)
ADPOH_Top in 1% F127 nanocapsule	17	24	1.03, 0.30	8
ADPOH_Top in 1% F98 nanocapsule	8	34	2.34, 0.77	8
ADPOH_Top in 1% F68 nanocapsule	22	54	1.48, 0.32	10
ADPOH_Top in 1% F38 nanocapsule	20	64	1.29, 0.26	12
ZnttbPc in 5% F127 nanocapsule	69	22	9.69, 2.64	3
ZnttbPc in 5% F98 nanocapsule	941	28	10.79, 2.55	3
ZnttbPc in 1% F68 nanocapsule	16395	56	1.06, 3.25	15
ZnttbPc in 1% F38 nanocapsule	16887	64	0.92, 3.31	15
ADP in 5% F127 nanocapsule	159	22	2.67, 2.69	6
ADP in 5% F98 nanocapsule	1845	28	2.86, 2.11	6
ADP in 1% F68 nanocapsule	152	49	1.85, 0.71	20
ZnPc in 5% F98 nanocapsule	67	30	2.17, 2.44	5
ZnPc in 1% F68 nanocapsule	16	56	0.93, 2.37	5
ZnPc in 1% F38 nanocapsule	56	64	0.87, 3.17	18

Based on the results in Figure 3.3 and Table 3.3, we conclude that the pluronic category is a main factor that significantly changes the T_{th}s of nanocapsules. Briefly, F127-based nanocapsule provided the lowest T_{th} and F38-based nanocapsule provided the highest. The pluronics' T_{th} sequence is F127 < F98 < F68 < F38. The possible mechanism[65,87] for this phenomenon is based on their different LCSTs: when the temperature rose over the LCST, the nanocapsule had a phase transformation and changed its cavity environment (where the fluorophores were encapsulated) from polar to non-polar state and/or non-viscous to viscous state. As a result, it significantly changed the quantum efficiencies of the fluorophores. Thus, the T_{th}s of nanocapsules were usually related to the LCSTs of pluronic categories.

3.3.4 The temperature threshold depends on the nanocapsules' concentrations

In this section, we studied another factor: the concentrations of the nanocapsules, which might also affect the T_{th}s. The nanocapsule solution were diluted to different concentrations and each solution was characterized. The concentration of nanocapsules was expressed by the pluronic concentration in the solution. As an example, we selected ADPOH_Bottom in 5% F98 nanocapsule as the original sample and diluted it by 5, 25, and 125 times correspondingly. Thus, we got ADPOH_Bottom in 1% F98 nanocapsule, ADPOH_Bottom in 0.2% F98 nanocapsule, and ADPOH_Bottom in 0.04% F98 nanocapsule, respectively. Figure 3.4 (a) shows their normalized fluorescence intensity as a function of temperature. Their T_{th}s were ~ 28 °C, 34 °C, 37 °C, and 41 °C, respectively. The result indicates that when the nanocapsules were diluted to a lower concentration, the T_{th} became higher.

Figure 3.4 (b)-(d) shows the similar measurement results of the other three nanocapsule samples when diluted: ADPOH_Bottom in 5% F127 nanocapsule, ADPOH_Top in 5% F68 nanocapsule, and ZnttbPc in 5% F98 nanocapsule. When each sample was diluted to a lower concentration, its T_{th}s increased correspondingly. Thus, it indicates that the nanocapsules with different fluorophore categories and pluoronic categories had the same phenomenon that their T_{th}s increased with the decrease of nanocapsules' concentration. We conclude that the nanocapsules' concentration was another factor that will change their T_{th}s. The possible mechanism is still under investigation. The characterization of all the nanocapsules in the section were summarized in Table 3.4.

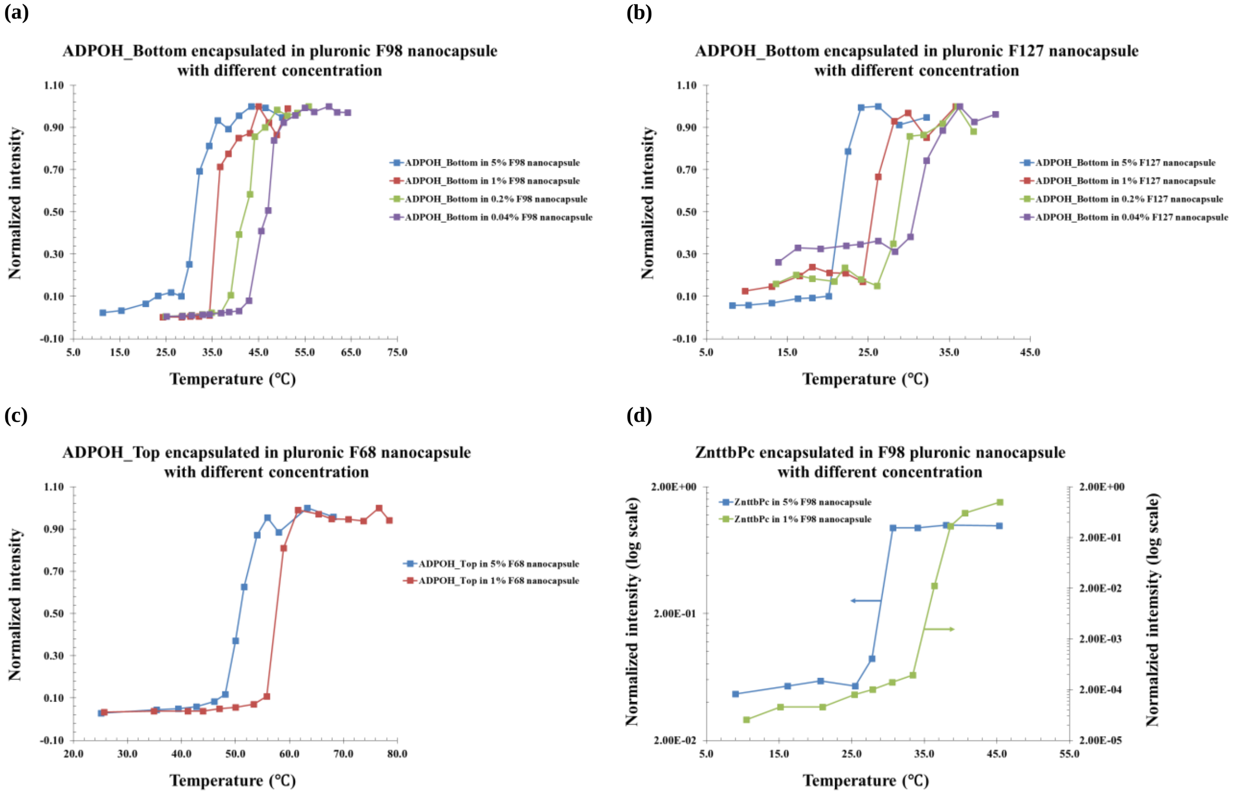

Figure 3.4 Fluorescence intensity as a function of temperature of (a) $ADP(OH)_2$_Bottom encapsulated in 5% pluronic F98, diluted to 1% pluronic F98, diluted to 0.2% pluronic F98, and diluted 0.04% pluronic F98 nanocapsule; (b) $ADP(OH)_2$_Bottom encapsulated in 5% pluronic F127, diluted 1% pluronic F127, diluted to 0.2% pluronic F127, and diluted to 0.04% pluronic F127 nanocapsule; (c) $ADP(OH)_2$_Top encapsulated in 5% pluronic F68, and diluted to 1% pluronic F68 nanocapsule; and (d) ZnttbPc encapsulated in 5% pluronic F98, and diluted to 1% pluronic F98 nanocapsule.

3.3.5 Different temperature-switching thresholds of nanocapsules under a camera

In order to verify whether the measurement results in the previous sections about different T_{th}s of nanocapsules are reliable, we can prepare the samples in several silicone tubes and measure their fluorescence intensities together under a camera. As an example, we measured the samples of $ADP(OH)_2$_Bottom encapsulated in 5% pluronic F98 nanocapsules and its diluted solutions (i.e., diluted to 1% pluronic F98, diluted to 0.2% pluronic F98, and diluted 0.04% pluronic F98) to see if we can repeat the results in Figure 3.4 (a). These four solutions were injected into four silicone tubes (*I.D.* = 760 μm) and fixed to a plastic holder. The plastic holder was attached to a piece of black board as background. Then, they were submerged into a water tank filled with water. The four tubes were submerged in the water so that their environment temperature stayed the same as that of water. The water temperature was controlled by a temperature controller. A 671nm laser was adopted as the excitation light and it was in DC mode.

Table 3.4

	I_{on}/I_{off}	T_{th} (°C)	τ_{on}/τ_{off}, τ_{on} (ns)	T_{bw} (°C)
ADPOH_Bottom in 5% F98 nanocapsule	9	28	1.29, 1.58	8
ADPOH_Bottom in 1% F98 nanocapsule	84	34	1.18, 1.52	6
ADPOH_Bottom in 0.2% F98 nanocapsule	40	37	1.21, 1.55	7
ADPOH_Bottom in 0.04% F98 nanocapsule	29	41	1.02, 1.31	10
ADPOH_Bottom in 5% F127 nanocapsule	10	20	1.14, 1.52	4
ADPOH_Bottom in 1% F127 nanocapsule	5	24	1.19, 1.77	4
ADPOH_Bottom in 0.2% F127 nanocapsule	6	26	1.24, 1.75	4
ADPOH_Bottom in 0.04% F127 nanocapsule	3	30	1.06, 1.85	6
ADPOH_Top in 5% F68 nanocapsule	7	48	1.30, 1.03	6
ADPOH_Top in 1% F68 nanocapsule	14	53	1.74, 0.43	8
ZnttbPc in 5% F98 nanocapsule	941	28	10.79, 2.55	3
ZnttbPc in 1% F98 nanocapsule	876	33	12.21, 2.50	5

An ICCD camera was placed on the top for fluorescence imaging of the four tubes. The camera was also in DC mode. Four long-pass interference filters (blocking band: 830 nm) and one absorption filter (blocking band: 830 nm) were placed in front of the camera lens as emission filters. The water temperature was increased gradually from room temperature = 22 °C to a high temperature = 50 °C. At different temperatures (step size: 1 °C), the ICCD camera recorded the fluorescence image of the tube tubes. Figure 3.5 (a) shows a white image of the four tubes under the camera with a selected FOV. From the top tube to the bottom, they were filled with $ADP(OH)_2$_Bottom encapsulated in 0.04% pluronic F98 nanocapsules, $ADP(OH)_2$_Bottom encapsulated in 0.2% pluronic F98 nanocapsules, $ADP(OH)_2$_Bottom encapsulated in 1% pluronic F98 nanocapsules, and $ADP(OH)_2$_Bottom encapsulated in 5% pluronic F98 nanocapsules correspondingly. Figure 3.5 (b) shows the normalized fluorescence image of the tubes in the same FOV, at room temperature = 22 °C. It is worth mentioning here that because of dilution, the absolute intensities of the fluorescence in the four tubes varied significantly. Typically, the more dilution meant the weaker the fluorescence intensity, because dilution meant a lower fluorophore concentration too. In order to provide a better visualization of the different T_{th}s, we measured the fluorescence of the four tubes at different temperatures and normalized the fluorescence as a function of temperature in each tube.

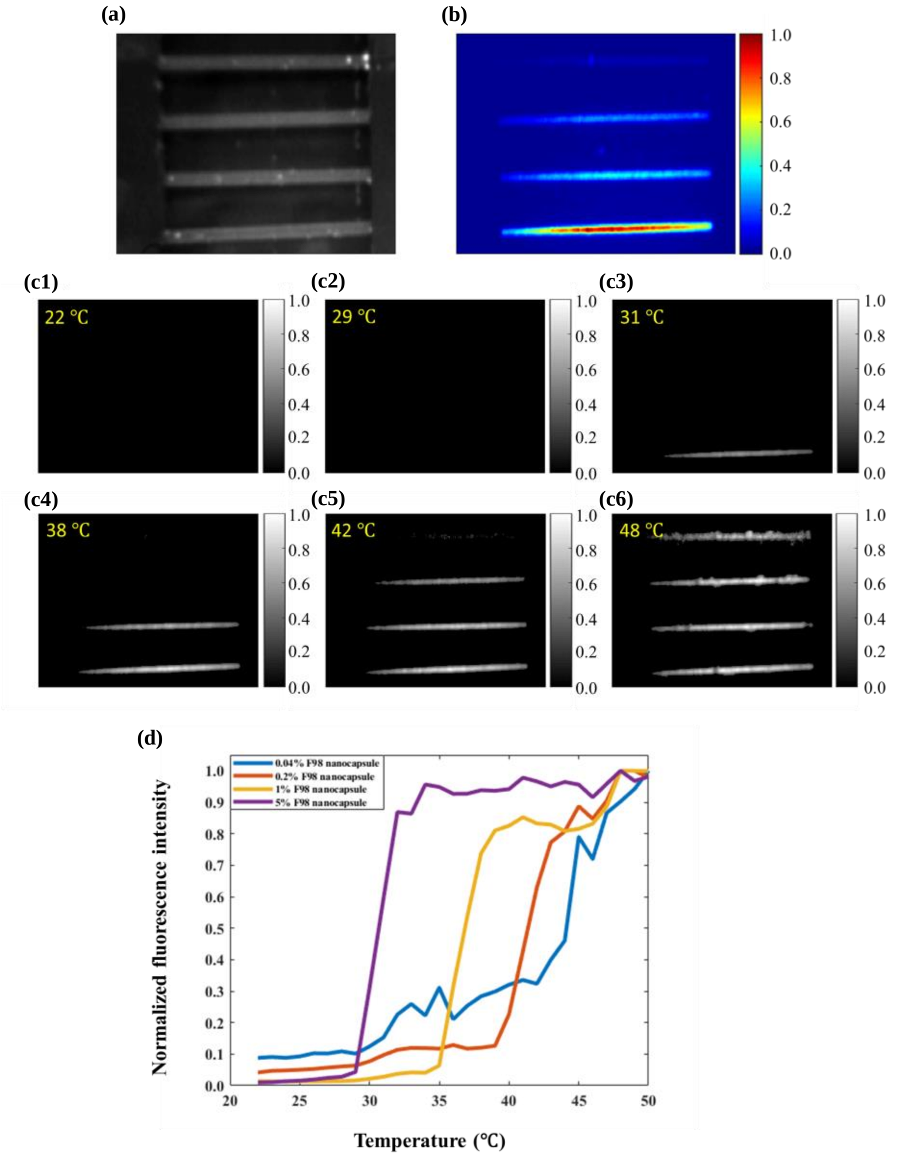

Figure 3.5 (a) A white image of the four silicone tubes. Each tube, from bottom to top, was filled with ADP(OH)$_2$_Bottom encapsulated in 5% pluronic F98, diluted to 1% pluronic F98, diluted to 0.2% pluronic F98, and diluted 0.04% pluronic F98 nanocapsule, correspondingly. (b) Normalized fluorescence image of the four silicone tube when the temperature = 22 °C. (c1-c6) Each tube was switched "on" one after another with the increase of temperature. Note that in each tube its fluorescence intensity was normalized as a function of temperature. A displaying threshold = 0.25 was applied in each image for visualization of either the fluorescence was still "off" or already switched "on". (d) Normalized fluorescence intensity in each tube plotted as a function of temperature.

Figure 3.5 (c1–c6) show the corresponding results. The images show their fluorescence intensities at different temperatures (22 °C, 29 °C, 31 °C, 38 °C, 42 °C, 48 °C). Note that the fluorescence intensity in each tube was normalized as a function of temperature. A displaying threshold = 0.25 was applied in each image for visualization of either the fluorescence was still "off" or already switched "on". Clearly, when the temperature = 22 °C or 29 °C (Figure 3.5 (c1) and (c2)), all the fluorescence tubes were at "off" state. This means the two temperatures were still below the T_{th}s of all samples. When the temperature rose to 31 °C (Figure 3.5 (c3)), the first bottom tube (filled with $ADP(OH)_2$_Bottom encapsulated in 5% pluronic F98 nanocapsules) was switched "on". When the temperature = 38 °C (Figure 3.5 (c4)), the second bottom tube (filled with $ADP(OH)_2$_Bottom encapsulated in 1% pluronic F98 nanocapsules) was switched "on". When the temperature = 42 °C (Figure 3.5 (c5)), the third bottom tube (filled with $ADP(OH)_2$_Bottom encapsulated in 0.2% pluronic F98 nanocapsules) was switched "on". Finally, when the temperature rose to 48 °C (Figure 3.5 (c6)), all the tubes were "on". Figure 3.5 (d) shows the normalized fluorescence intensity in each tube plotted as a function of temperature. The measurement results were similar to that in Figure 3.4 (a). This experiment clearly shows that measuring different T_{th}s of nanocapsules in our previous system[63] is reliable and also is repeatable in the camera-based fluorescence imaging system.

3.4 Discussion

3.4.1 The nanocapsules are appropriate for ultrasound switchable fluorescence (USF) imaging

Some pluronic nanocapsules have been selected and adopted as USF contrast agents in our previous work.[65-68] They have several advantages in USF imaging. First, the fluorophores (i.e., ADP or ZnPC series) are NIR dyes so their fluorescence has a good penetration in biological tissue. Second, comparing to other USF contrast agents, many nanocapsules show a high I_{on}/I_{off}, which helps improve the signal-to-noise ratio (SNR) of a USF image. For example, the ICG-NPs was a commonly used USF contrast agent in USF imaging[57,64], but its I_{on}/I_{off} is only ~ 5–10 folds. In contrast, some pluronic nanocapsules have an I_{on}/I_{off} up to tens of thousands of folds. A high I_{on}/I_{off} helps reduce the background fluorescence significantly and thus increase the SNR. Third, some nanocapsules also showed a high τ_{on}/τ_{off}. A high τ_{on}/τ_{off} could potentially help increase the SNR of a USF image in a time-domain USF imaging system.[58] Fourth, the nanocapsules provide a variety of T_{th}s and thus are appropriate for USF imaging in both *ex vivo* and *in vivo* scenarios. In conclusion, the nanocapsules have excellent thermal-switchable properties and are appropriate contrast agents for USF imaging.

3.4.2 The nanocapsules are appropriate for temperature sensing

In this work, we demonstrated that the nanocapsules' T_{th}s varied in a wide temperature range from ~ 20 °C to ~ 64 °C. Their T_{th}s could be adjusted by changing the pluronic categories and/or the nanocapsule concentrations. These nanocapsules usually had an excellent fluorescence intensity switching property (i.e., a high I_{on}/I_{off}) so that they should have a high sensitivity in temperature sensing. Also, these nanocapsules had a T_{BW} of a few to tens of Celsius degrees (from 3 °C up to 20 °C). Thus, the nanocapsules can be used as temperature sensors. Their temperature sensing range depends on the T_{BW}: when the temperature crosses the T_{BW}, the fluorescence increases significantly. For example, the ADP in 5% F98 nanocapsule has a fluorescence intensity increase most when the temperature rises from ~ 28 °C to ~ 34 °C (seen in Figure 2 (a)); it means this nanocapsule has a most efficient temperature sensing range from 28 °C to 34 °C. By combining these nanocapsules with different T_{th}s and T_{BW}s, we can develop temperature sensors covering a wide temperature range.

3.5 Conclusion

In this work, we successfully synthesized, characterized, and selected a series of NIR nanocapsules, by encapsulating two series of NIR fluorophores (ADP and ZnPc) in four pluronic polymers (F127, F98, F68, and F38). These nanocapsules showed excellent temperature-switchable properties of fluorescence intensity and/or lifetime. Also, we investigated that some factors (i.e., pluronic categories and nanocapsules' concentration) affected the nanocapsules' T_{th}s while other (i.e., fluorophore categories) did not. By selecting appropriate pluronic categories and adjusting the nanocapsule's concentration, we can synthesize the nanocapsules with a wide range of T_{th}s. These temperature-switchable fluorescence nanocapsules can be used for USF imaging and temperature sensing.

Chapter 4 Develop a time-domain USF imaging system based on a time-gated ICCD camera

4.1 Introduction

As described in the previous chapters, we used the following parameters[63] to quantify the performance of a USF contrast: an on-to-off ratio of fluorescence strength (I_{on}/I_{off}), an on-to-off ratio of fluorescence lifetime (τ_{on}/τ_{off}), an adjustable temperature threshold to switch on fluorophores (T_{th}), a narrow temperature transition bandwidth (T_{BW}), and the fluorophore's peak excitation (λ_{ex}) and peak emission (λ_{em}) wavelength, which determines the light penetration depth in a biological tissue. In our previous study[58], we showed that a contrast agent with a high ratio of τ_{on}/τ_{off} can help to improve signal-to-noise ratio (SNR) by adopting a time-domain system. In this study, we plan to implement this time-domain method via an intensified charge-coupled device (ICCD) camera[71], which can acquire two-dimensional (2D) fluorescence images compared with the previous single point detection via a single channel time-domain system using a photomultiplier tube (PMT). In addition, several experimental parameters (i.e., data acquisition time including CCD camera recording time and intensifier gate delay, FU power, and imaging depth) need to be optimized in the time-domain USF imaging and they can affect image qualities (i.e., SNR, spatial resolution, and temporal resolution).

We demonstrated the working principle of the time-domain USF imaging system, including how the ICCD imaging system measured the fluorescence lifetime, how to acquire a USF signal from fluorescence pulses, and how to scan a USF image in this system. Meanwhile, we adopted two near-infrared (NIR) USF contrast agents for the time-domain USF imaging: $ADP(OH)_2$-Bottom[86] in 5% pluoronic F98 nanocapsule and ZnttbPc in 5% pluoronic F98 nanocapsule. Details of the two fluorophores $ADP(OH)_2$-Bottom and ZnttbPc as well as the nanocapsules are described in Chapter 3. Both nanocapsules have excellent USF properties: excellent I_{on}/I_{off}, narrow T_{BW}, appropriate T_{th}, and NIR excitation and emission spectrum. The $ADP(OH)_2$-Bottom-based contrast agent has a nearly fixed fluorescence lifetime so that the ratio τ_{on}/τ_{off} is close to 1. Meanwhile, the ZnttbPc-based contrast agent has a high τ_{on}/τ_{off} ratio, which means its fluorescence lifetime significantly increases when the temperature is raised above its T_{th}. By comparing these two contrast agents, we have shown how τ_{on}/τ_{off} affects USF signals. Using this ICCD-based time-domain system and the two USF contrast agents, we have investigated how the USF image qualities (i.e., SNR, spatial resolution, and temporal resolution) are affected by the camera's recording time, FU driving voltage, sample thickness, and intensifier gate delay.

4.2 Methods

4.2.1 Chemical materials

Tetrabutylammonium iodide (TBAI), zinc 2,9,16,23-tetra-tert-butyl-29H,31H-phthalocyanine (ZnttbPc), and chloroform was purchased from Sigma-Aldrich Corporate (St. Louis, MO, USA). Pluronic F98 pastille was purchased from BASF Corporation (Vandalia, IL, USA). BF2-chelated [5-(4-hydroxyphenyl)-3-phenyl-1H-pyrrol-2-yl]-[5-(4-hydroxyphenyl)-3-phenylpyrrol-2-ylidene] amine ($ADP(OH)_2$-Bottom)[86] was synthesized at the Department of Chemistry, University of North Texas (Denton). All chemicals were used as received without further purification.

4.2.2 Synthesis protocols of USF contrast agents

The synthesis protocols of $ADP(OH)_2$-Bottom in 5% F98 nanocapsules and ZnttbPc in 5% F98 nanocapsules were the same as the protocol of synthesizing a nanocapsule described in Chapter 3. Basically, 0.4 mg $ADP(OH)_2$-Bottom dye or 1.2 mg ZnttbPc dye added with 4.8 mg TBAI were dissolved in 6 mL chloroform. 0.75 g pluoronic F98 was dissolved in 15 mL distilled water to get 5% F98 solution. The dye solution was then added dropwise to the 5% F98 solution with 600 rpm stirring. The mixture was under sonication (power: 40 Watts) for 4 mins to form nanocapsules. The mixture was stirred with 475 rpm overnight in a chemical hood until the chloroform evaporated totally. The solution was then filtered (membrane cut-off pore size: 450 μm) to obtain the purified sample.

4.2.3 Sample configuration protocol of silicon phantoms

The protocol of making a silicone phantom was the same as described in Chapter 2. The silicone kit was purchased from Factor II Inc. (VST-50: VerSilTal Silicone Elastomer). The kit includes two major components: silicone elastomer and catalyst. Basically, 4 mg titanium dioxide (TiO_2) was fully dissolved in 6 mL silicone catalyst by stirring for 20 mins and then mixed with 60 mL silicone elastomer. TiO_2 functions as light scatters in the silicone phantom; the estimated absorption coefficient $\mu_a = 0.03$, and the reduced scattering coefficient $\mu_{s'} = 3.5\ cm^{-1}$.[64,65,81] The mixture was poured into a plastic container, and the silicone tube was inserted through the container. The amount of the poured mixture could be adjusted so that the silicone tube was imbedded at an appropriate depth. Then the sample was placed in a vacuum hood to remove the bubbles in the mixture. The silicone was solidified at room temperature for 12 hours. After that, the plastic container was peeled off, and the silicone phantom was ready to use.

4.2.4 System setup

4.2.4.1 Principles of time-domain fluorescence measurement via a gated ICCD camera

When fluorophores are excited by a narrow light pulse, the emission of fluorescence is widely expanded compared with the width of the excitation light pulse (depending upon the fluorescence lifetime of the fluorophores). By measuring this dynamic decay of this fluorescence emission pulse, the lifetime of fluorescence can be quantified. Figure 4.1 schematically shows the measurement system. Briefly, a picosecond (ps) pulsed supercontinuum laser (SC-450, Fianium, Eugene, Oregon; with a broad illumination band) and a time-gated ICCD camera (Picostar HR, LaVision, Goettingen, Germany) were used. The manufacturer-claimed laser pulse width was ~5 ps, and the repetition rate was 20 MHz. The intensifier in ICCD camera was synchronizedly triggered by the laser followed with a delay unit, so that the intensifier was turned on in a selected time-gated window with the same repetition rate (20 MHz). The laser and ICCD camera were coupled into an inverted fluorescence microscope (Ti-U, Nikon). The excitation filter, dichroic mirror/beam splitter and emission filters were selected based on the specific fluorophores. The aqueous fluorescent sample was placed in a quartz cell and submerged in a quartz tank of water on the microscope stage for fluorescence measurement. The temperature of water was controlled and measured by a thermometer for monitoring the environment temperature of the sample.

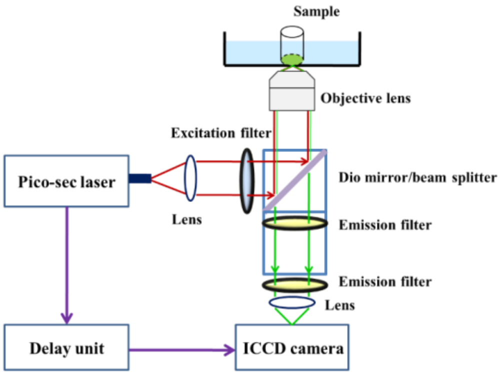

Figure 4.1 Set up of the time-domain fluorescence measurement system. [71]

Figure 4.2 displays a schematic diagram of the gated ICCD camera. Generally, three major parts are included: (1) a gated image intensifier, (2) relay coupling lenses, and (3) a CCD chip. The image intensifier functions as an optical amplifier. Briefly, the incoming photons are first converted into electrons via a photocathode, and then amplified by a short and gated high voltage. After that, the amplified electrons are converted into visible photons via a phosphor. These visible photons are delivered to the CCD chip for imaging via the coupling lens. The temporal resolution of a gated ICCD camera depends on the gate width of the applied high voltage, which, in this study, is down to 300 ps. It is this high temporal resolution that allows an ICCD camera to measure fast fluorescence decay. It is worth mentioning that, compared with the short gate width, the CCD chip usually responds much more slowly and the exposure time is around tens to hundreds of milliseconds. Therefore, the CCD chip is usually used to accumulate those repeated and fast optical signals for achieving an acceptable SNR.

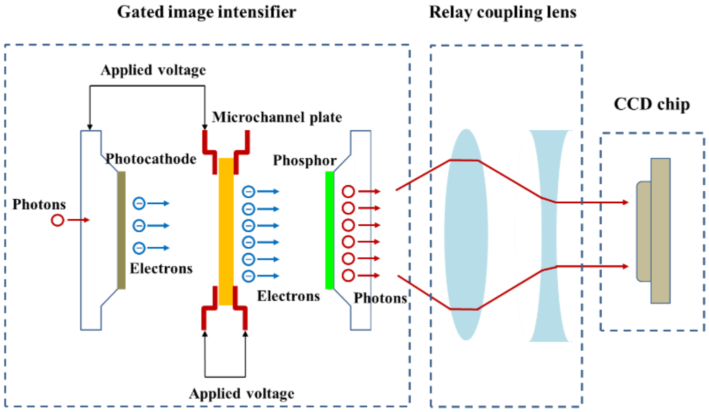

Figure 4.2 Schematic diagram of the gated ICCD camera.[71]

To measure the fast fluorescence decay signal after excitation by a short laser pulse via a gated ICCD camera, three steps are followed (see Figure 4.3): (1) selecting an appropriate gate width (t_w = 300 ps here) for the ICCD camera, fixing the time interval between the laser pulse and the gate voltage of the ICCD's intensifier, and firing multiple laser pulses (repetition rate: 20 MHz) to accumulate enough photons in the CCD chip (this step provides an image on the CCD chip corresponding to the fluorescence dynamic strength at a single time point (t in Figure 4.3); (2) increasing the time interval between the laser pulse and the intensifier gate voltage with a small step ($\Delta t = 100$ ps here), and repeating step (1); and (3) continuing step (2) until the entire fluorescence decay signal is completely scanned. Thus, a series of images are acquired as a function of the delay time interval (0, Δt, $2\Delta t$,…, nΔt). If an average of the signal strength is calculated for each image within a selected region of interest (ROI), the fluorescence dynamic decay curve can be reconstructed and plotted as a function of time. Figure 4.3 also shows an example of a series of recorded images. The blue dot in the third row represents the averaged fluorescence strength in the ROI. It is worth mentioning that because the ICCD camera provides a 2D fluorescence image, this system can measure fluorescence lifetimes at different locations if necessary.

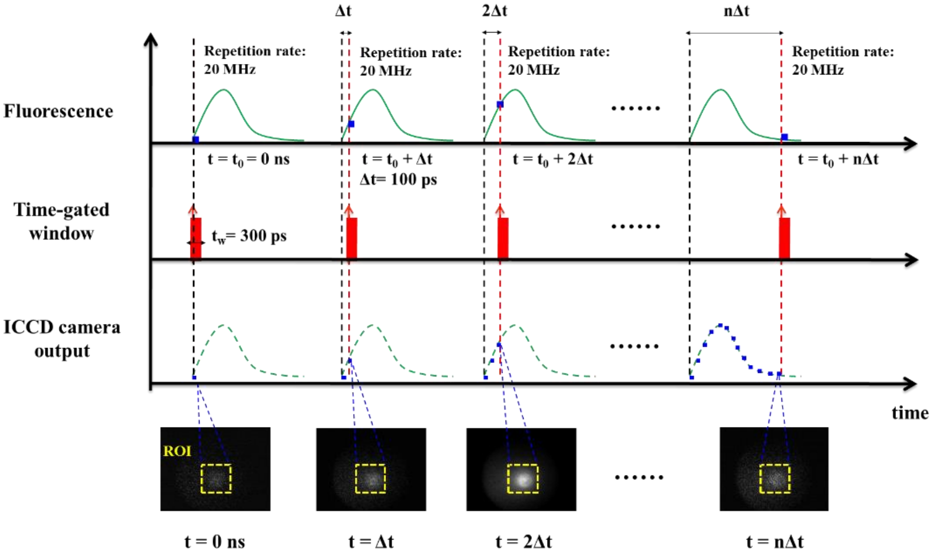

Figure 4.3 Principle of measuring the fast fluorescence decay signal after excited by a short laser pulse via the gated ICCD camera. [71]

4.2.4.2 Optical filter setup in the ICCD camera imaging system

The optical filter sets (Semrock, Rochester, New York) for fluorescence pulse measurement of the samples (i.e., ADP$(OH)_2$-Bottom dye in chloroform, ADP$(OH)_2$-Bottom in 5% F98 nanocapsule, and ZnttbPc in 5% F98 nanocapsule) included one band-pass interference filter (center wavelength: 650 nm, bandwidth: 60 nm) for excitation, one dichroic mirror (edge wavelength: 700 nm) for beam-splitting, and two long-pass interference filters (blocking band: 715 nm) for emission. The optical filter sets (Semrock, Rochester, New York) for laser pulse measurement included one band-pass interference filter (center wavelength: 650 nm, bandwidth: 60 nm) for excitation and one 50% beam splitter; no emission filter was used. The objective lens was 4× magnification, and the FOV size was ~ 3.2 mm in diameter.

4.2.4.3 ICCD camera-based time-domain USF imaging system

By adding an ultrasonic system to the fluorescence lifetime imaging system (i.e., Figure 4.1), we can set up an ICCD camera-based time-domain USF system. Figure 4.4 shows the schematic diagram of the system. Compared with Figure 4.1, a FU transducer (central frequency: 2.5 MHz) and its driving system were added. A function generator (33220A, Agilent, Santa Clara, CA, USA) was triggered by the ICCD camera via an internal trigger and used to generate the driving signal (i.e., a 2.5 MHz sinusoidal wave). This signal was further amplified by a radiofrequency power amplifier (325LA, E&I, Rochester, NY, USA) and delivered to a FU transducer (H-108, Sonic Concepts Inc, Bothell, WA, USA) to generate an ultrasonic wave. The FU transducer was mounted on a motorized three-dimensional translation stage (Velmex Inc. Bloomfield, NY, USA; not shown in the diagram). Because the whole system was built on the inverted fluorescence microscope, excitation photons were delivered to and emission photons were collected from the bottom of the sample. The ultrasound was delivered from the top and focused inside the sample to generate a temperature rise for switching fluorescence.

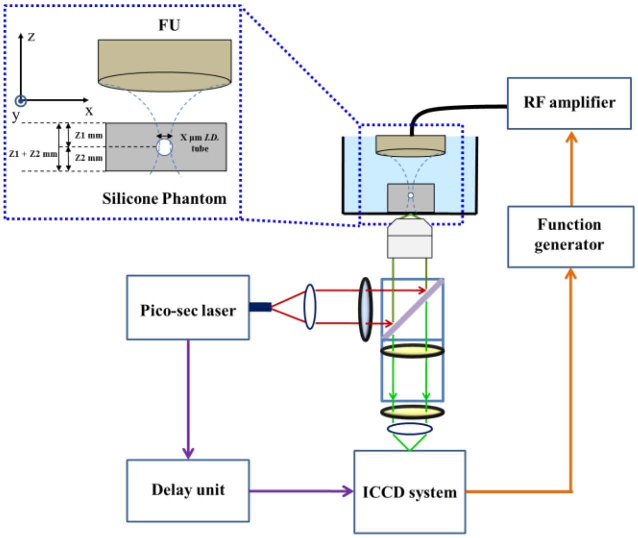

Figure 4.4 Schematic diagram of ICCD camera-based time-domain USF system. [71]

Figure 4.4 also shows the configuration of the silicone phantom and the FU transducer (top left). A silicone tube was inserted into the silicone phantom, which was then placed in a quartz tank. The tank was filled with water for coupling the ultrasound wave into the sample and placed on the microscope's sample stage. TiO_2 was dissolved in the silicone phantom to make it a scattering medium to mimic biological samples. As mentioned in the previous section 4.2.3, the reduced scattering coefficient μ_s' was 3.5 cm^{-1}; the absorption coefficient μ_a was 0.03 cm^{-1}.[64,65,81] The tube in the phantom was filled with USF contrast agents and used as an imaging target. The inner diameter (*I.D.*) and the location of the tube were variable in different experiments. The distance from the top surface of the phantom to the tube center was denoted as Z1 (mm in unit), the distance from the bottom surface of the phantom to the tube center was termed Z2, and the total thickness was (Z1 + Z2). The *I.D.* of the tube was termed X (μm in unit). For USF imaging, the FU transducer was initially focused on the silicone tube (FU position: x = 0.00 mm, y = 0.00 mm, z = 0.00 mm).

Figure 4.5 displays the time sequences of different events to show how the USF signal was acquired. Note that in this figure the time scale was at a level of nanoseconds, as discussed before. The first row represents the excitation light pulses (the repetition rate was 20 MHz; i.e., the time interval between any two adjacent pulses was t_i = 50 ns). The second row indicates the background fluorescence pulses before applying ultrasonic pulses, which had the same repetition rate. The background signal might mainly came from laser leakage, phantom autofluorescence, and background fluorescence from the USF contrast agents that were not 100% off. The third row shows the fluorescence signal after applying ultrasonic pulses (i.e., the sum of USF signal and background signal). The fourth row indicates the gating setup of the ICCD intensifier. Here, the gate was delayed a small amount of time (t_0) compared with the excitation laser trigger (i.e., the time interval between the black and the first red dash lines) to avoid acquiring the background fluorescence but to acquire the USF signal roughly starting from the peak of the pulse. The gating width was 3 ns with the 20 MHz repetition rate. Thus, only the photons within the gate could be detected. The fifth row indicates the acquired USF signal in the gated window. Theoretically, the USF signal in each gate can be extracted by subtracting the background signal from the total signal (the shadowed area). Practically, this subtraction was not conducted in each individual gate. Instead, depending on the CCD exposure time (at a level of hundreds of milliseconds in this study), the subtraction was conducted between two CCD images that have accumulated many pulses (i.e., the CCD image without ultrasound exposure was subtracted from the other one with ultrasound exposure; see Figure 4.6). Depending on how fast the curves would decay in the background and USF signals, varying the delay time t_0 may optimize the SNR of USF imaging, which was investigated in the *Results*.

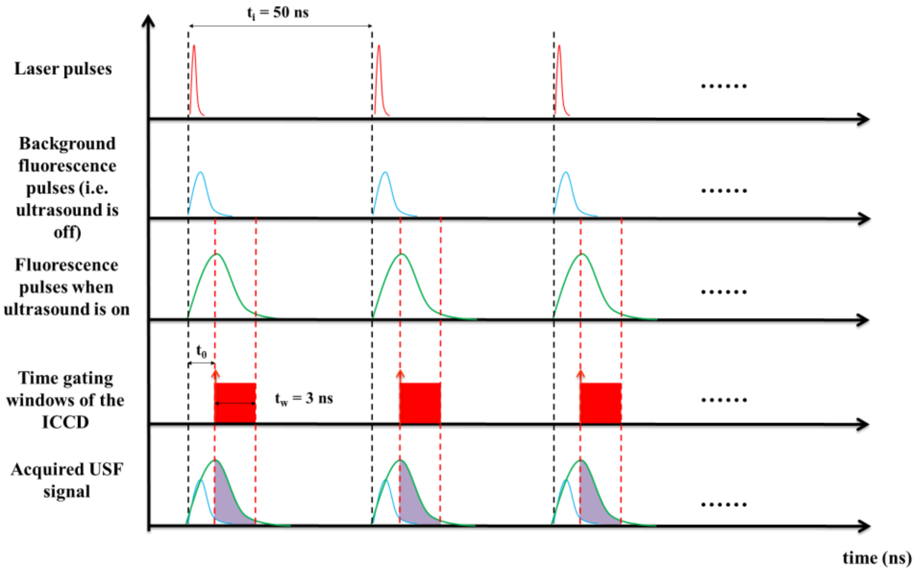

Figure 4.5 Time sequences of different events to show how USF signal was acquired at a time scale level of nanoseconds.[71]

Figure 4.6 shows the time sequence of the CCD camera, FU exposure, and acquired USF signals on the CCD camera. The CCD camera continuously took frames with a fixed exposure time of 400 ms (see the light yellow region) and a readout time of 200 ms (see the light green region). Before the FU was triggered, the camera acquired several frames (here, number of frames = 3) as the background baseline. Then, the FU transducer was triggered on via the internal trigger from the CCD camera (t = 1.8 s). The FU exposure duration was also 400 ms. The driving peak-to-peak voltage from the function generator was 130 mV and was amplified with a 50 dB gain via the power amplifier. As an example, a series of CCD frames acquired at different times (t = 0.6 s, 1.2 s, … 6.0 s) are shown in the figure. The silicone phantom adopted in this experiment had a thickness of 12 mm (Z1 = 6 mm, Z2 = 6 mm) and a tube *I.D.* X = 310 µm. ADP(OH)$_2$-Bottom encapsulated 5%-F98 pluronic nanocapsule solution was filled in the tube as the USF contrast agent. This USF signal was acquired when the FU was focused on the tube (FU position x = 0.00 mm, y = 0.00 mm, z = 0.00 mm). To extract the USF signal, one background frame acquired at t = 1.8 s (which was right before the FU signal) was subtracted from each frame acquired after the FU exposure (i.e., the frames acquired at t = 2.4 s, 3.0 s, … 6.0 s). The figure also shows the resulting frames (last row). To represent the USF signal strength as a single value, we adopted the simple approach of summing up the counts of all the pixels in each frame. The purple squares in the third row represent the calculated USF strength as a function of time using this method.

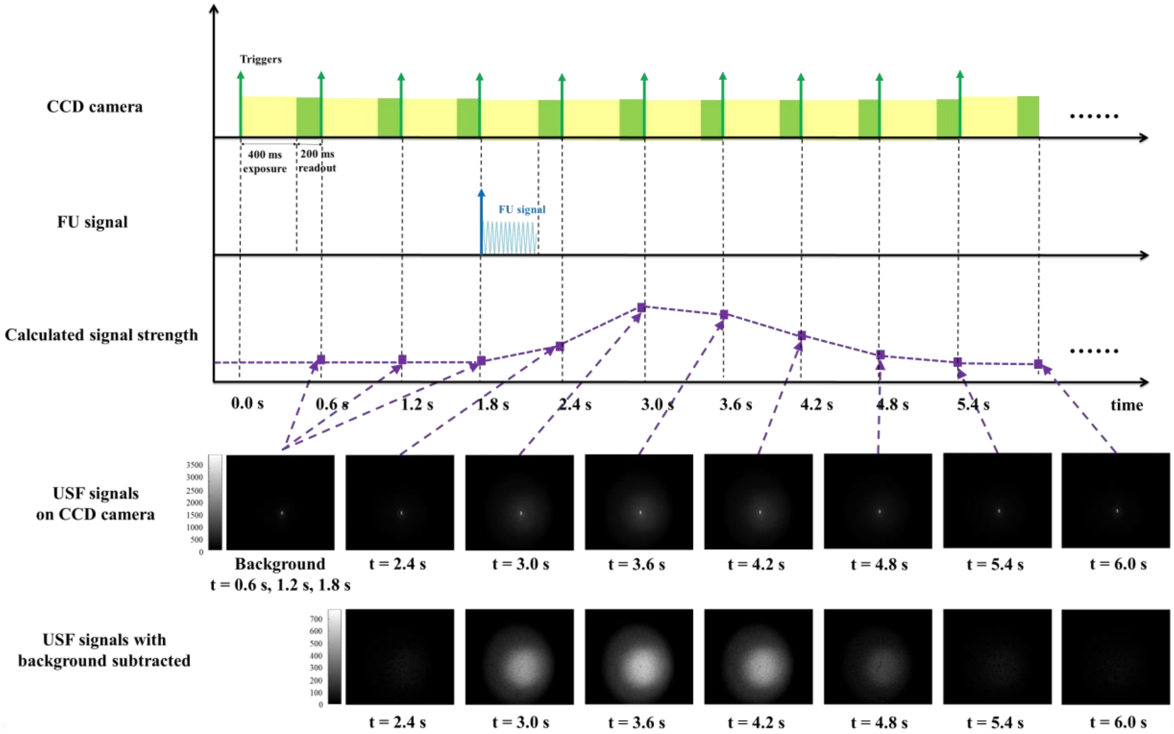

Figure 4.6 Time sequence of the CCD camera, FU exposure, and acquired USF signals on CCD camera.[71]

Because of scattering, the USF photons displayed on the CCD camera frames were spatially scattered as a spot. The full width at half maximum (FWHM) of the spot here was ~ 2.0 mm, which was much larger than the tube *I.D.* (X = 310 μm) and the lateral focal size of the FU transducer at half-amplitude (~ 0.8 mm). In addition, the purple dash line in Figure 4.6 clearly shows that the FU exposure can induce USF photons. After the FU exposure, USF signal strength reached the maximum. After that, the signal strength gradually decreased. This procedure can be understood based on the following mechanism. The FU exposure led to the temperature rising in the ultrasound focal volume. The USF agents in this volume where the temperature was above the switching threshold (T_{th} = 31 °C) were switched on to emit fluorescence. This volume expanded after the FU exposure, then gradually decreased and eventually vanished.

4.3 Results

4.3.1 Fluorescence intensity and lifetime measurement of fluorophores and USF contrast agents

Based on the principles of time-domain fluorescence measurement (see the *Methods*, section 4.2.4.1), we measured fluorescence lifetimes of the fluorophores used in this study in different formats (fluorophores of ADP$(OH)_2$-Bottom in chloroform, ADP$(OH)_2$-Bottom encapsulated 5%-F98 pluronic nanocapsule, and ZnttbPc encapsulated 5%-F98 pluronic nanocapsules). Figure 4.7 (a)–(e) show the measurement results. All the data are normalized. The blue line in each figure represents the measured excitation laser pulse in each experiment, which represents the system's impulse response function (IRF). The solid red or green line represents the measured fluorescence pulse. The dashed red or green line represents the calculated exponential decay function, calculated by deconvolving the IRF from the measured fluorescence emission signal (after normalization). The decay factor in the exponential function represents an averaged fluorescence lifetime of each fluorophore. Note that for simplicity we selected an exponential function with a single decay factor. Although this simplification may miss some detailed information when the fluorophore has multiple lifetimes, it is good enough for us to demonstrate the principle of time-domain USF imaging and implement this idea for different fluorophores. Figure 4.7 (a) shows that the fluorescence lifetime of the fluorophore of ADP$(OH)_2$-Bottom in chloroform was ~1.70 ns. Figure 4.7 (b)–(e) show the fluorescence lifetimes of two USF contrast agents: 1) ADP$(OH)_2$-Bottom in 5% pluoronic F98 nanocapsule and 2) ZnttbPc in 5% pluoronic F98 nanocapsule at two temperatures: 20 °C and 40 °C. Both USF contrast agents were thermal-sensitive, and their temperature switching thresholds were ~ 28–31 °C. Figure 4.7 (b) and (c) represent the measured fluorescence lifetimes of ADP(OH)$_2$-Bottom in 5% pluoronic F98 nanocapsule at 20 °C and 40 °C, respectively. The results indicate that its fluorescence lifetime slightly increased from 0.97 ns to 1.02 ns when temperature rose from 20 °C to 40 °C. If we denote the lifetime as τ_{off} when temperature is below the threshold and τ_{on} when temperature is above it, the ratio of τ_{on} to τ_{off} is only 1.05 (i.e., 1.02/ 0.97).

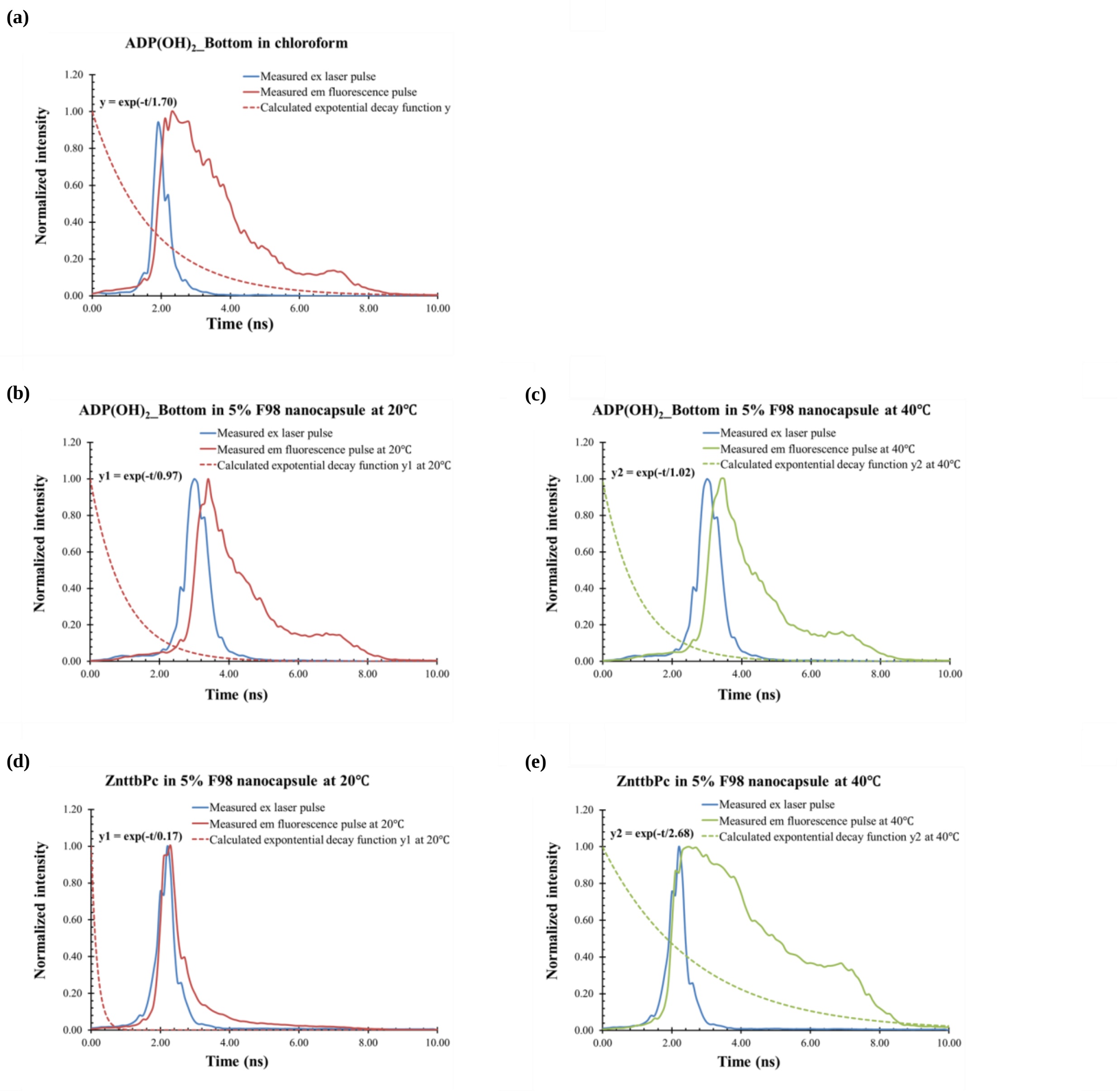

Figure 4.7 (a) The measured fluorescence lifetime of the fluorophore of ADP(OH)$_2$-Bottom in chloroform. (b) The measured fluorescence lifetimes of ADP(OH)$_2$-Bottom in 5% pluoronic F98 nanocapsule at 20 °C. (c) The measured fluorescence lifetimes of ADP(OH)$_2$-Bottom in 5% pluoronic F98 nanocapsule at 40 °C. (d) The measured fluorescence lifetimes of ZnttbPc in 5% pluoronic F98 nanocapsule at 20 °C. (e) The measured fluorescence lifetimes of ZnttbPc in 5% pluoronic F98 nanocapsule at 40 °C. [71]

Figure 4.7 (d) and (e) represent the measured fluorescence lifetime of ZnttbPc in 5% pluoronic F98 nanocapsule at 20 °C and 40 °C, respectively. In contrast, its fluorescence lifetime changed significantly (τ_{on}/τ_{off} =15.76; i.e., 2.68/0.17). This result was beneficial for USF imaging for achieving high SNR in time-domain and was one of the motivations in this study. It is worth mentioning that both USF contrast agents showed a significant increase in fluorescence strength when temperature rose above the threshold. Similarly, if we denote the peak fluorescence strength when temperature is below (T = 20 °C) and above (T = 40 °C) the threshold as I_{off} and $I_{on,}$ respectively, a ratio (I_{on}/I_{off}) can be calculated. For ADP(OH)$_2$-Bottom in 5%-F98 nanocapsules, its I_{on}/I_{off} is ~ 17 folds ($I_{on} = 5.74 \times 10^3$ counts; the average strength in the selected ROI). For ZnttbPc in 5%-F98 nanocapsules, its I_{on}/I_{off} is ~ 46 folds ($I_{on} = 0.55 \times 10^3$ counts; the average strength in the selected ROI). The measurement results of these two nanocapsules were similar to that measured in the fluorescence intensity and lifetime measurement system[63] (see the *Results* in Chapter 2). Therefore, taking advantage of the significant changes in both fluorescence strength and lifetime may help improve USF image quality compared with only using strength change.

4.3.2 Different lifetimes of fluorescence and laser pulse on 2D ICCD camera images

In the previous section 4.3.1 it shows that the laser pulse can be much shorter (usually its lifetime < 500 ps) than some fluorescence pulses that have long fluorescence lifetimes (> 1.0 ns). In this section we demonstrated that this ICCD camera imaging system was capable of measuring different lifetimes on the same FOV. Figure 4.8 (a) left shows the experiment sample setup. A silicone phantom ($\mu_s' = 3.5$ cm^{-1}, $\mu_a = 0.03$ cm^{-1}, total thickness Z = 3 mm) imbedded with a silicone tube (*I.D.* = 760 μm, Z1 = Z2 = 1.5 mm) was placed on a plastic Petri dish, and they were placed on the microscope stage for imaging (with a 4× objective lens). When the laser beam was focused on the bottom surface of the phantom, near the tube, the plastic Petri dish gave laser reflection and generated autofluorescence on the pathway. CCD images captured the corresponding signal spot (the round red spot in Figure 4.8 (a) left). This signal should have a short lifetime. Meanwhile, the silicone tube was filled with ZnttbPc in 5% F98 nanocapsule. The Petri dish was filled with hot water at 40 °C so that the phantom was heated and the contrast agent inside the tube was switched on and presented a long lifetime. CCD images also captured the scattered fluorescence signal from the tube (the green line in Figure 4.8 (a) left). Figure 4.8 (a) right shows one real example image from the experiment.

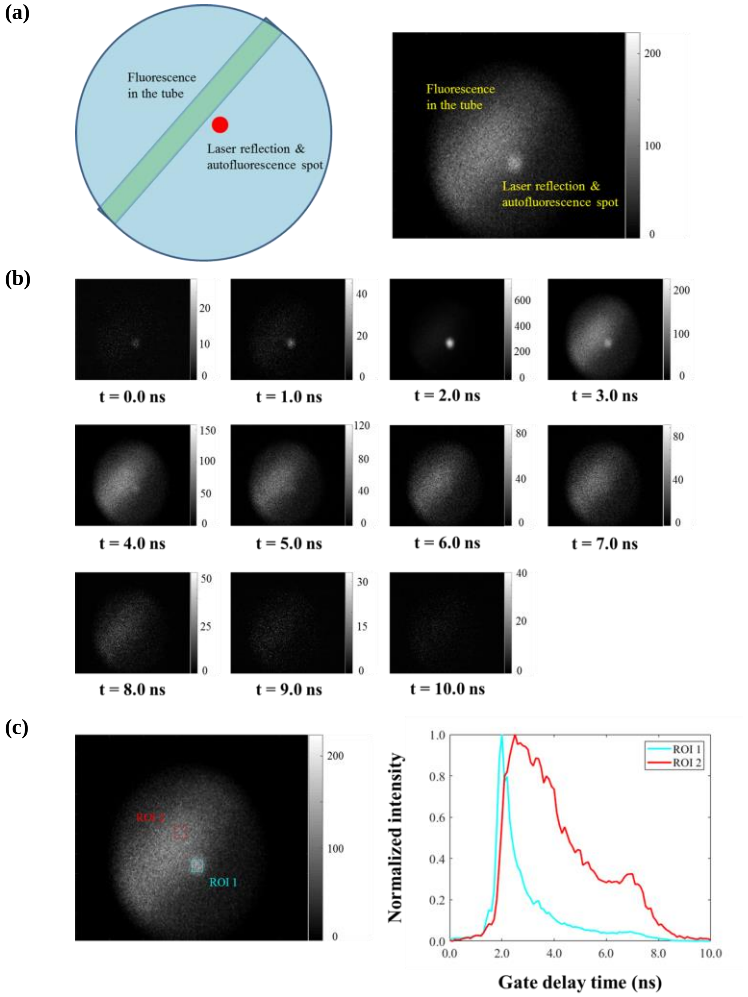

Figure 4.8 (a) Experiment sample set-up (left plot) and one real example image from the experiment (right plot). (b) A series of CCD images captured at different gate delay t. (c) Different measured lifetimes (seen in the right plot) when different region of interest (ROI) was selected: ROI 1 was selected on the round beam spot and ROI 2 was selected on the tube (seen in the left plot). [71]

Figure 4.8 (b) shows a series of CCD images captured at different gate delay t; t was counted from the start time of the gate, and the gate width was fixed at t_w = 300 ps as previously (seen in Figure 4.3). Figure 4.8 (b) clearly shows that the round beam spot appeared first but disappeared fast and that the fluorescence in the tube appeared later but disappeared much more slowly because of its long lifetime. Figure 4.8 (c) shows the different lifetimes measured when different ROIs were selected. ROI 1 was selected on the round beam spot, so it showed a relatively short lifetime of laser leakage plus plastic autofluorescence. Its decay time (down to 37%, without deconvolution from impulse response function (IRF), same below) was ~ 0.49 ns. On the other hand, ROI 2 was selected on the tube so it showed a long lifetime of fluorescence signal. Its decay time was ~ 3.87 ns.

4.3.3 USF imaging of a silicone tube in the silicone phantom

Following the example of USF imaging of a silicone phantom (Z1 = 6 mm, Z2 = 6 mm; the tube *I.D.* X = 310 μm; ADP(OH)$_2$-Bottom encapsulated 5%-F98 pluronic nanocapsule was filled in the tube) described in the *Methods* section 4.2.4.3 (refer to Figure 4.6), by scanning the FU transducer focus and acquiring USF signals at each location, a USF image was formed. Figure 4.9 shows the normalized USF profile of the tube. The FU transducer scanned across the tube along the x-axis with a total scanning range of 3.96 mm and a step size of 76.2 μm (i.e., 53 scanning points along the x-axis). Here, we counted the USF signal at t = 2.4 s with background subtracted as the signal strength. The FWHM of the USF profile is 0.80 mm, when the tube *I.D.* is 0.31 mm. The SNR is 72.3. To calculate SNR, the peak USF strength was divided by the standard deviation of the background strength. The background region was selected as those data points that were far away from the peak signal (i.e., the data points on the left of the left green cross and those on the right of the right green cross in Figure 4.9). The same rule was adopted for other examples in this study.

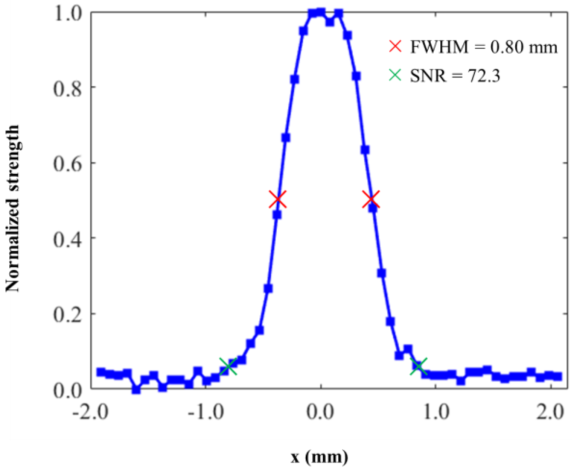

Figure 4.9 Normalized USF profile of the silicone tube. [71]

4.3.4 The effect of experimental parameters on USF image qualities

4.3.4.1 The effect of CCD camera recording time on USF imaging

When the FU transducer scanned along both x-axis and y-axis, a 2D USF image was acquired. Following the previous section, we adopted the same silicone phantom (Z1 = 6 mm, Z2 = 6 mm, X = 310 μm) for 2D USF imaging. The FU transducer scanned across the tube along the x-axis at three y-axis positions (y = 0.00 mm, 1.01 mm, 2.03

mm). Likewise, we counted the USF signal at t = 2.4 s with background subtracted as the signal strength. The image in the first row and the first column in Figure 4.10 (a) shows the corresponding normalized 2D USF image. The average FWHM of the USF image of the tube is 0.82 mm, and the average SNR is 89.9. Other images in Figure 4.10 (a) represent the USF images of the same tubes but we counted the USF signal from other frames (i.e., t = 3.0 s, 3.6 s, … 6.0 s) with background subtracted. Here, the time of t indicates the CCD camera recording time.

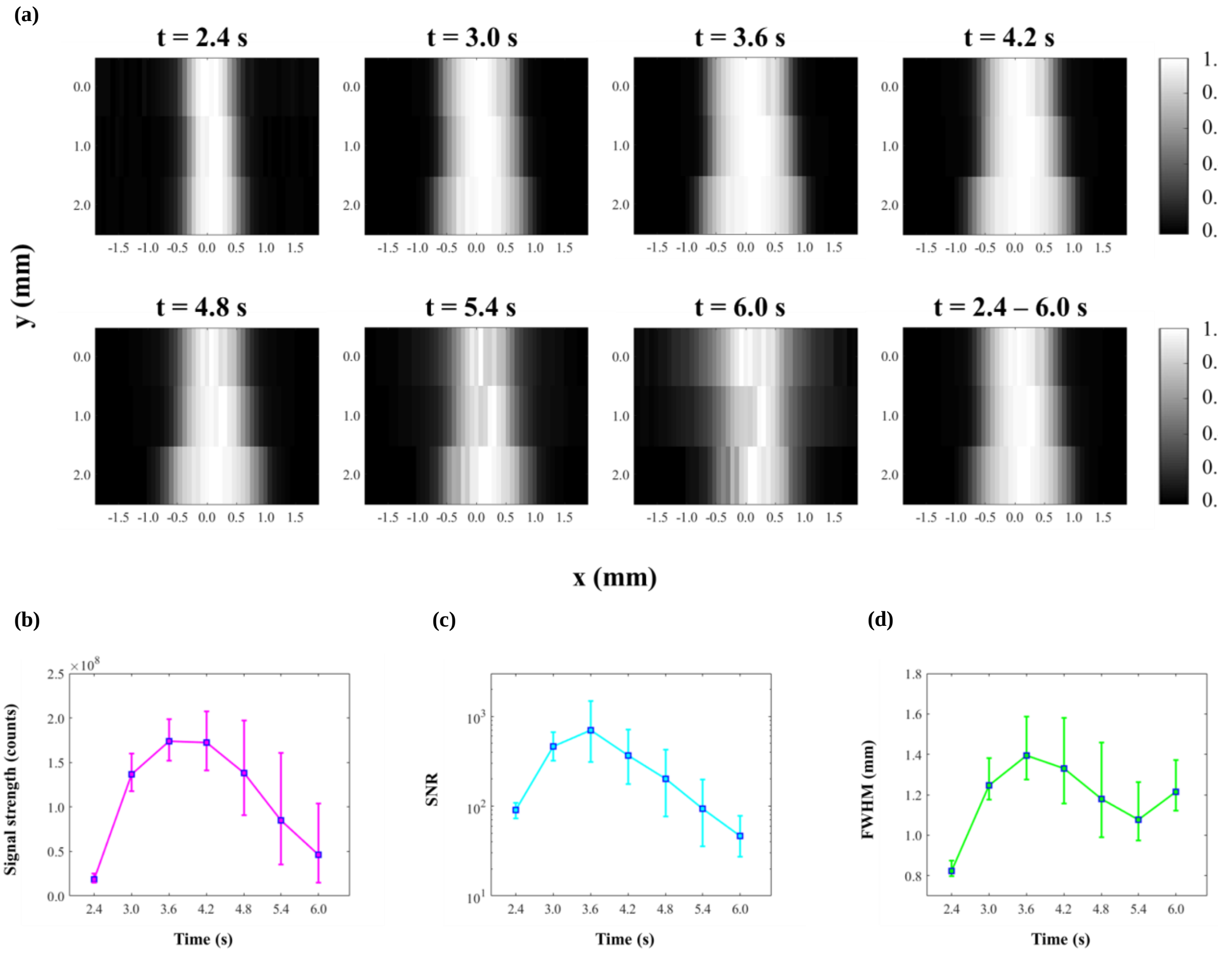

Figure 4.10 (a) USF images of the silicone tube when counting USF signal from different CCD camera recording time t = 2.4 s, 3.0 s, … 6.0 s. (b) Relationship between USF signal strength acquired on the center of the tube and CCD camera recording time. (c) Relationship between the signal-to-noise ratio (SNR) of USF images and CCD camera recording time t. (d) Relationship between the full width at half maximum (FWHM) of imaged tube and CCD camera recording time t. [71]

On each USF image in Figure 4.10 (a), we calculated the average of the three USF signal strengths acquired at the center of the tube (i.e., at x = 0.00 mm, while y = 0.00 mm, 1.01, and 2.03 mm) and plotted them as a function of time t in Figure 4.10 (b). The blue squares represent the average strength, and the error bar represents the upper and lower values. The plot shows that the signal strength increases first and then decreases, which agrees with the result shown in Figure 4.6. Similarly, Figure 4.10 (c) shows the relationship between the averaged SNR and t. SNR reaches 89.9 when t = 2.4 s and increases to 700.0 when t = 3.6 s. After that, SNR gradually decreases to 46.6 when t = 6.0 s. Figure 4.10 (d) shows the relationship between the FWHMs of the USF images in Figure 4.10 (a) and t. At t = 2.4 s, FWHM is as small as 0.82 mm, which represents the highest spatial resolution. When t = 3.6 s and 6.0 s, FWHM degrades to 1.40 mm and 1.21 mm, respectively.

Figure 4.10 (b) and (c) indicate that a higher signal strength provided a higher SNR of image, because background noise should all be similar in this experiment. Figure 4.10 (b–d) indicate that USF signal strength, SNR, and FWHM increase first and then decrease. This means that adopting an early frame (t = 2.4 s) or a late frame (t = 5.4 s or 6.0 s) for calculating the USF strength enables achievement of a relatively higher spatial resolution at the expense of signal strength and SNR. On the other hand, adopting a middle frame (t = 3.6 s) enables achievement of a relatively higher signal strength and SNR at the expense of spatial resolution. This tradeoff consists with the fact that a larger voxel can generate a stronger signal but provide lower spatial resolution. On the other hand, increasing the CCD exposure time over the entire signal duration can help to collect more USF photons to increase the signal strength and SNR, but may degrade the spatial resolution because of possible thermal diffusion. This has been demonstrated in the last image in Figure 4.10 (a). This image is the mathematical sum of all images from t = 2.4 s to t = 6.0s and gives a relatively high SNR (245.3) but a relatively large FWHM (1.26 mm). These results indicate that SNR and spatial resolution depend on the CCD camera recording time when the USF signal is acquired and that these two parameters may need to be balanced.

4.3.4.2 The effect of FU driving voltage on USF imaging

In this section, we studied the relationship between FU driving voltage and imaging qualities (i.e., signal strength, SNR, and resolution). Theoretically, the square of the driving voltage of the FU transducer is proportional to the ultrasound exposure power. In the experiments, it was difficult to quantify the actual power in the focal area. Therefore, we selected the FU driving voltage from the function generator as the experimental variable. The same silicone phantom was adopted (Z1 = 6 mm, Z2 = 6 mm, X = 310 μm) for USF imaging. ADP(OH)$_2$-Bottom encapsulated 5%-F98 pluronic nanocapsule solution was filled in the tube as the USF contrast agent. Similarly, the FU transducer scanned across the tube (i.e., along the x-axis) with a total scanning range of 3.05 mm and a step size of 76.2 μm (i.e., 41 scanning points along the x-axis) to achieve a line scan at one FU driving voltage. The same line scan was then conducted with a different FU driving voltage. In this experiment, the driving peak-to-peak voltages (Vpps) were 70 mV, 100 mV, 130 mV, and 160 mV, respectively. All other experimental parameters and data processing remained the same as in the previous experiment.

Figure 4.11 (a) shows the USF signals acquired at x = 0.00 mm (i.e., FU was focused on the center of the tube) with different Vpp (i.e., Vpp = 70 mV, 100 mV, 130 mV, and 160 mV). The left plot shows that the USF signal strength increased with Vpp. Peak signal strengths were 0.25, 0.79, 1.70, and 2.12 ($\times 10^8$) counts, respectively. The right plot shows the normalized signal strengths over time, respectively. It shows the USF signal duration also increased with the increase of Vpp. The rise time was 0.42 s, 0.41 s, 0.97 s, and 2.16 s, and the fall time was 0.54 s, 0.94 s, 1.86 s, and 2.87 s, respectively. The definition of rise or fall time here is the time duration from 37% to 100% signal strength increase or from 100% to 37% signal strength decrease. This agrees with the fact that the ultrasound-heated volume in which the temperature was above the switching threshold of the agent increases with the Vpp (i.e., FU exposure power).

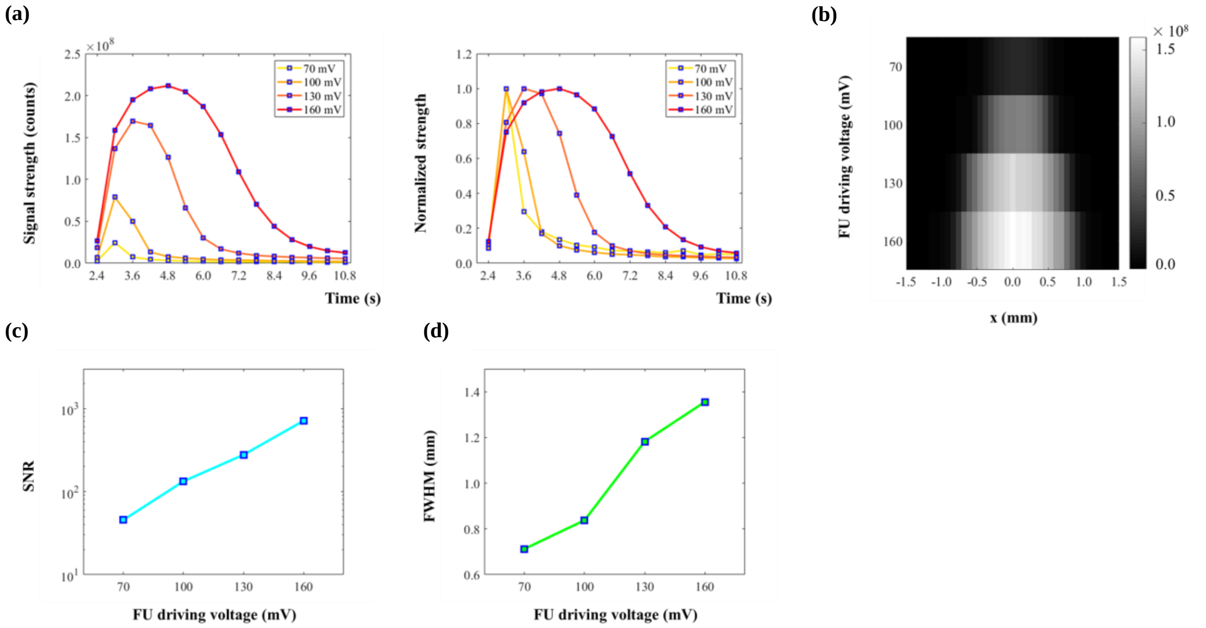

Figure 4.11 (a) The USF signals acquired at x = 0.00 mm (i.e., FU was focused on center of the tube) with different Vpp (i.e., Vpp = 70 mV, 100 mV, 130 mV and 160 mV). In the left plot, it shows the USF signal strength increased with Vpp. In the right plot, it shows the normalized signal strengths over time: USF signal duration also increased with the increase of Vpp. (b) 2D USF image representing the relationship between image profile and FU power. (c) Relationship between SNR of imaged tube and FU power. (d) Relationship between FWHM of imaged tube and FU power. [71]

A 2D image was plotted to further show the effect of the Vpp on USF signal in Figure 4.11 (b). USF signals acquired at the frame t = 3.0 s (with background subtracted) were used to represent the strength. The horizontal axis represents the FU scanning range across the tube (i.e., along the x-axis at y = 0.00 mm). The vertical axis represents the corresponding Vpp. The maximum USF strength at each Vpp was 0.26, 0.82, 1.37, and 1.59 (× 10^8) counts, respectively. It is worth mentioning that the maximum USF strength here was not necessarily the same as the peak strength in Figure 4.11 (a) because 1) the maximum USF strength here was not necessary at x = 0.00 mm, and 2) the USF strength acquired here at the frame t = 3.0 s was not necessary at the same frame when USF signal reached peak: Figure 4.11 (a) shows USF signal reached peak at frame t = 3.0 s, 3.0 s, 3.6 s, and 4.8 s when Vpp = 70 mV, 100 mV, 130 mV, and 160 mV, respectively. At the same time, as the Vpp rose, the USF image of the tube broadened. Figure 4.11 (c) and (d) represent the corresponding changes of SNR and FWHM at the four driving voltages. For the four Vpps, the SNR is 45.5, 133.0, 277.1, and 712.7, and the FWHM is 0.71 mm, 0.84 mm, 1.18 mm, and 1.36 mm, respectively. This indicates that increasing Vpp can improve SNR but degrade spatial resolution. Accordingly, SNR and spatial resolution may need to be balanced when selecting appropriate Vpp.

4.3.4.3 The effect of the sample thickness on USF imaging

This section discusses the relationship between sample thickness and imaging qualities (i.e., signal strength, SNR, and resolution). In this experiment, we made four phantoms with different thicknesses. Specifically, Z2 varied from 6, 9, 12 to15 mm, respectively, but Z1 remained at 6 mm, and the *I.D.* of the tube remained at 310 μm for all the Z2. The Vpp was 130 mV. In the 2D USF imaging of each phantom, the FU transducer scanned across the tube along the x-axis with a total scanning range of 3.96 mm and a step size of 76.2 μm (i.e., 53 scanning points along the x-axis) at three y-axis positions (y = 0.00 mm, 1.01 mm, 2.03 mm). Other experimental parameters remained the same as before. Figure 4.12 (a) represents the USF signals acquired at x = 0.00 mm, y = 0.00 mm, in the four phantoms with Z2 = 6, 9, 12, and 15 mm, respectively. The left plot shows that the USF signal strength significantly decreased as Z2 increased. Their peak strengths were 14.58, 1.45, 0.15, and 0.09 (× 10^7) counts, respectively. Meanwhile, the right plot displays the respective normalized signal strengths over time and shows that the USF signal duration changed slightly when Z2 increased. The rise time was 0.96 s, 0.96 s, 1.08 s, and 0.90 s, and the fall time was 1.17 s, 1.79 s, 1.81 s, and 2.03 s, respectively.

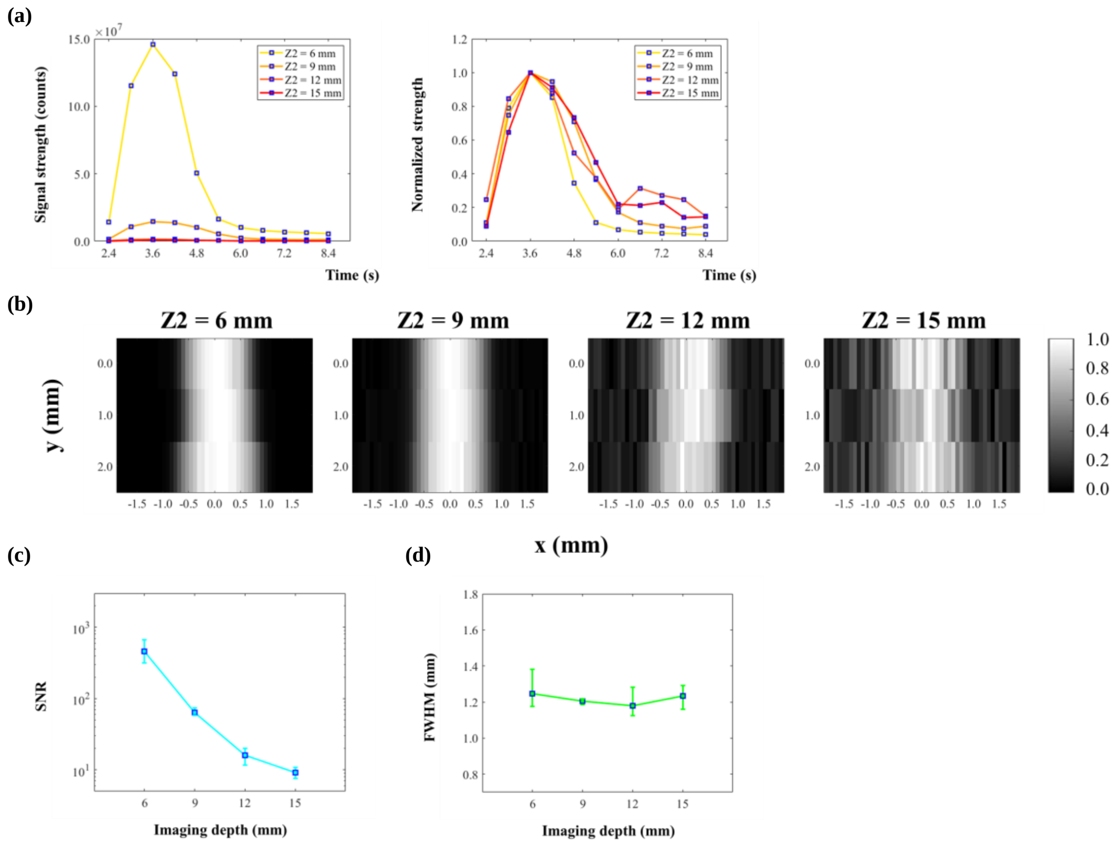

Figure 4.12 (a) USF signals acquired at x = 0.00 mm, y = 0.00 mm, in the four phantoms with different Z2 = 6, 9, 12 and 15 mm. In the left plot, it shows the USF signal strength significantly decreased with the increase of Z2. In the right plot it shows the normalized signal strengths over time: the USF signal duration changed slightly when the Z2 increased. (b) Normalized 2D USF images acquired at different imaging depth Z2 = 6, 9, 12 and 15 mm. (c) Relationship between SNR of imaged tube and imaging depth Z2. (d) Relationship between FWHM of imaged tube and imaging depth Z2. [71]

Figure 4.12 (b) shows the normalized 2D USF images acquired at different Z2. Here, we used USF signals acquired at frame t = 3.0 s (with background subtracted) to represent the signal strength. The results also indicate that the SNR decreased very quickly when Z2 increased. However, the imaged tube did not obviously broaden or narrow (i.e., the FWHM remained stable). Figure 4.12 (c) and (d) represent the relationships of SNR and FWHM with Z2, respectively. The blue square represents the average strength, and the error bar represents the upper and the lower values. The SNR = 459.0, 63.9, 16.0, and 9.2 (average value), and the FWHM = 1.25 mm, 1.21 mm, 1.18 mm, and 1.23 mm when, correspondingly, Z2 = 6, 9, 12 and 15 mm.

The results show that the SNR decreased quickly (Figure 4.12 (c)) as the sample thickness increased. This is understandable because the thicker the sample was, the more excitation and emission photons were lost due to the scattering and absorption. However, the signal duration (the right plot in Figure 4.12 (a)) and the FWHM (Figure 4.12

(d)) appeared independent of the thickness. This is because they were mainly determined by the size of the ultrasound-heated volume where the temperature was above the switching threshold of the agent, which was independent of Z2 in this study. Note that the FU Vpp in this experiment remained at 130 mV, and the ultrasound penetration depth remained at Z1 = 6 mm.

4.3.4.4 The effect of gating delay on USF imaging

In the ICCD camera-based, time-domain USF imaging system, the gate delay of the ICCD camera relative to the laser pulse can be well controlled. This capability provides a way to further improve SNR based on the following assumptions. First, the laser leakage and the sample autofluorescence usually have shorter lifetimes compared with that of the USF signal. Thus, they may be removed by appropriately delaying the intensifier gate. If the gate is delayed to a time point when the laser leakage and autofluorescence are low (because of their short lifetimes) but the USF signal is still strong (because of its long lifetime), it is possible to have a higher signal-to-background ratio (SBR) and therefore a higher SNR. Second, when a USF contrast agent has a high ratio of τ_{on}/τ_{off}, appropriately delaying the gate may also potentially reduce the background noise generated by non-100% off USF contrast agents. When the USF contrast agent is not 100% off, it may emit some fluorescence even without ultrasound. If the fluorescence lifetime of this background noise (denoted as τ_{off}) is much shorter than that of the ultrasound-switched on contrast agents (denoted as τ_{on}), the gating method may be very helpful to remove this type of noise as well. The new USF contrast agent of ZnttbPc encapsulated 5%-F98 pluronic nanocapsules has shown a high value of τ_{on}/τ_{off}.

To demonstrate the above ideas via the time-domain system, a new phantom was set up, as Figure 4.13 (a) shows. We adopted a silicone phantom with a thickness of 4 mm for USF imaging. Other parameters were similar to the ones used before. A silicone tube with an *I.D.* X = 760 μm was embedded in the middle of the phantom and filled with one of the two types of USF contrast agents (see the details in Table 4.1). For USF imaging, the FU transducer was initially focused on the silicone tube (FU position: x = 0.00 mm, y = 0.00 mm, z = 0.00 mm). The contrast agents in the tube were considered as the imaging target. A quartz cuvette was placed under the silicone phantom and filled with one of the two types of USF contrast agents (see the details in Table 4.1). Thus, the contrast agents in the cuvette generated a strong fluorescence emission that was considered background noise. Three combinations of different USF contrast agents were filled in the silicone tube and the cuvette.

Table 4.1[71]

	Tube (Target: τ_{on})	**Cuvette (Background: τ_{off})**	**τ_{on}/τ_{off} (T/B)**
Case 1	$ADP(OH)_2$-Bottom NC (τ_{on}=1.02 ns)	$ADP(OH)_2$-Bottom NC (τ_{off}=0.97 ns)	1.05 (=1.02/0.97)
Case 2	$ADP(OH)_2$-Bottom NC (τ_{on}=1.02 ns)	ZnttbPc NC (τ_{off}=0.17 ns)	6.00 (=1.02/0.17)
Case 3	ZnttbPc NC (τ_{on}=2.68 ns)	ZnttbPc NC (τ_{off}=0.17 ns)	15.76 (=2.68/0.17)

NC: Nanocapsules. In Case 1, both the tube and the cuvette were filled with $ADP(OH)_2$-Bottom encapsulated 5%-F98 pluronic nanocapsules. In Case 2, the tube was filled with $ADP(OH)_2$-Bottom encapsulated 5%-F98 pluronic nanocapsules and the cuvette with ZnttbPc encapsulated 5%-F98 pluronic nanocapsules. In Case 3, both the tube and the cuvette were filled with ZnttbPc encapsulated 5%-F98 pluronic nanocapsules. For $ADP(OH)_2$-Bottom based contrast agent: τ_{on} = 1.02 ns and τ_{off} = 0.97 ns. For ZnttbPc based contrast agent: τ_{on} = 2.68 ns and τ_{off} = 0.17 ns.

Based on Figure 4.7 (b) and (c), the $ADP(OH)_2$-Bottom-based agent had a fluorescence lifetime of τ_{off} = 0.97 and τ_{on} = 1.02 ns, respectively, which gave a ratio of τ_{on}/τ_{off} = 1.05. On the other hand, based on Figure 4.7 (d) and (e), the ZnttbPc-based agent had a lifetime of τ_{off} = 0.17 and τ_{on} = 2.68 ns, respectively, which gave a ratio of τ_{on}/τ_{off} = 15.76. In Case 1, the $ADP(OH)_2$-Bottom-based agent was in both the target and the background, and $\tau_{on}/\tau_{off} \approx 1$, which simulated a situation in which the target had a lifetime similar to that of the background. This scenario may occur when the adopted USF agent does not change its fluorescence lifetime much before and after being switched on (i.e., only the emission strength increases). In Case 2, the ZnttbPc-based agent was in the background and was not switched on. Therefore, τ_{off} = 0.17 ns was considered the background fluorescence lifetime. In contrast, the $ADP(OH)_2$-Bottom-based agent was in the target and was switched on by the ultrasound. Accordingly, τ_{on}=1.02 ns was considered the target fluorescence lifetime. Thus, Case 2 mimicked a situation of τ_{on}/τ_{off} = 6.00 (i.e., 1.02/0.17), meaning that the target had a relatively longer lifetime than the background. This scenario may occur when the laser leakage or sample autofluorescence dominates the background noise. Case 3 had a ratio of τ_{on}/τ_{off} = 15.76, which mimicked a situation in which the target had a much longer lifetime than that of the background. This scenario may occur when the background noise is mainly generated from the non-100% off USF agents. Accordingly, we expect that the method of delaying the gate may affect the SNR in Case 2 and 3 but may not in Case 1.

Figure 4.13 (b) schematically shows three modes of delaying the imaging gate for the three different cases. Note that the time scale was at a level of nanoseconds here (similar to Figure 4.5). The left panel represents Case 1, in which both the background and the USF signal had similar lifetimes and decayed at a similar speed. The right panel represents Case 2 and 3, in which the background had a short lifetime and decayed fast while the USF signal had a long lifetime and decayed slowly. Mode 1 indicates that the gate was slightly delayed compared with the laser pulse so that the fluorescence emission peak was located within the gate. Mode 2 means that the gate was delayed 3 ns (in this study) more than Mode 1. Mode 3 was delayed 3 ns more than Mode 2 (i.e., 6 ns more compared with Mode 1). The gate width was 3 ns in all three modes.

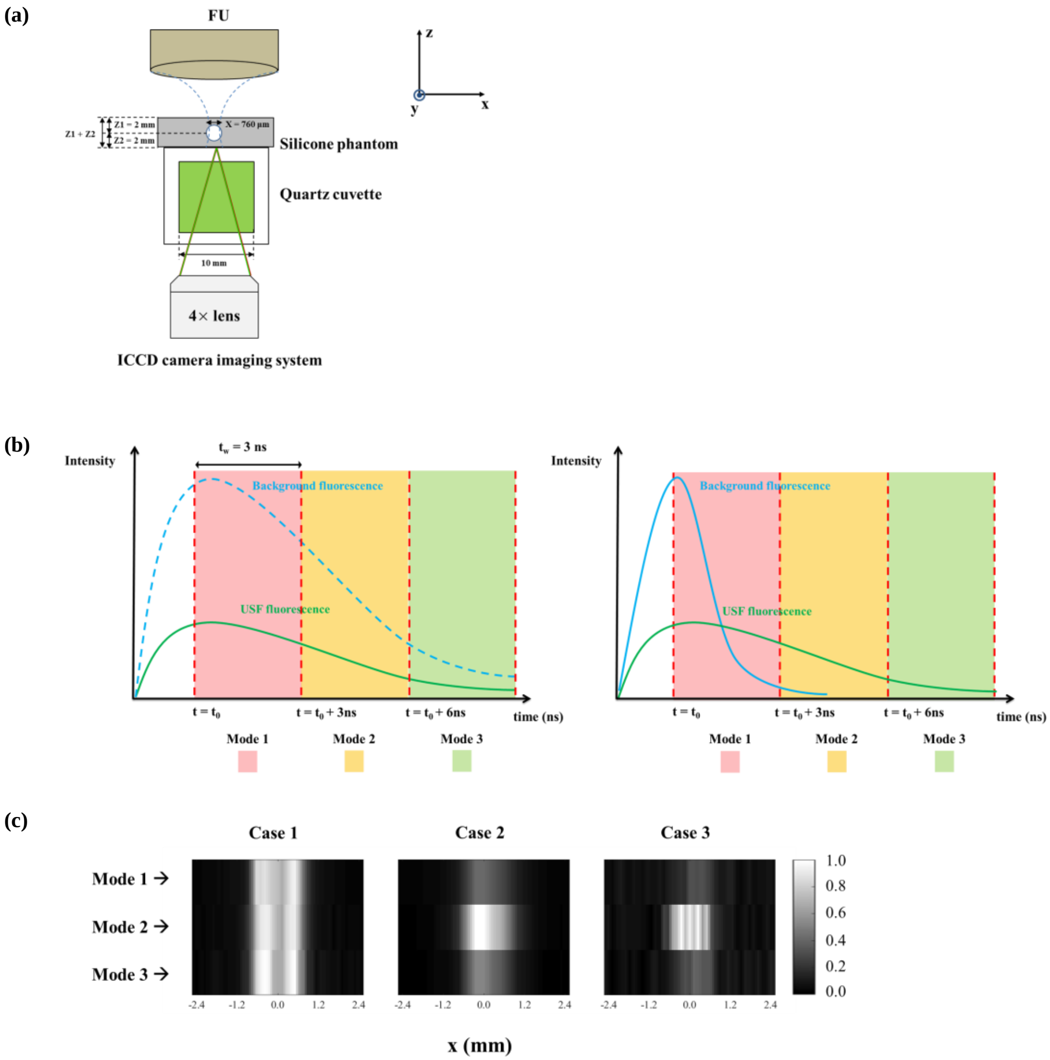

Figure 4.13 (a) Silicone phantom and USF signal measurement setup. (b) Scheme of the three selected time-gated window (i.e., mode 1, mode 2, and mode 3) for the three cases: the left panel represents Case 1 in which both the background and the USF signal had similar lifetimes and decayed at a similar speed; the right panel represents Case 2 and 3 in which the background had a short lifetime and decayed fast while the USF signal had a long lifetime and decayed slowly. (c) USF images acquired at the three modes for the three cases.[71]

Figure 4.13 (c) shows the USF images acquired at the three modes for the three cases. In all USF images, FU was scanned across the tube (i.e., along the x-axis) with a total scanning range of 5.08 mm and a step size of 127.0 µm (i.e., 41 scanning points). The Vpp was 130 mV. To make the USF images directly comparable, the ICCD camera intensifier gain in each experiment was tuned to keep the background signal at the same level. To increase the sensitivity, the CCD camera exposure time was increased to 3 seconds so that the USF signal was acquired in one frame after FU exposure, an idea discussed in the previous section (represented in the last image in Figure 4.10 (a)). The data were linearly interpolated to achieve smooth images. All other experimental parameters remained the same. Table 4.2 summarizes the SNR and FWHM of the USF images. From both this table and the images in Figure 4.13 (c), we find that in Case 2 and 3 the USF images achieved the highest SNRs when Mode 2 was adopted. This result validates the idea that the SNR can be optimized by adjusting the delay time of the ICCD's gate when the target's fluorescence lifetime is longer than that of the background noise. On the other hand, in Case 1, all three modes provided USF images with similar SNRs. This result validates the idea that the method of adjusting the delay time of the ICCD's gate does not increase the SNR when the target's lifetime is similar to that of the background noise. Meanwhile, the FWHMs of the imaged tube in the three modes remained similar in each case (see Table 4.2), which indicates that spatial resolution was independent of gating delay.

Table 4.2[71]

	Case 1		**Case 2**		**Case 3**	
	SNR	**FWHM (mm)**	**SNR**	**FWHM (mm)**	**SNR**	**FWHM (mm)**
Mode 1	46.4	1.48	37.1	1.31	7.8	0.76
Mode 2	47.3	1.46	**53.7**	1.25	**34.1**	1.11
Mode 3	47.5	1.45	36.3	1.22	8.0	0.98

In Case 1, Mode 1-3 provided USF images with similar SNRs; in both Case 2 and Case 3, USF images achieved the highest SNRs when the Mode 2 was adopted. In all cases, FWHMs remained similar in the three modes.

Note that the switched-on fluorescence lifetimes (τ_{on}) discussed here and shown in Figure 4.7 (c) and (e) were measured by immersing the USF agents in a hot water bath with a temperature above the switching threshold of the agent (i.e., $T = 40\ °C > T_{th}$). We also developed a method to directly measure the τ_{on} when using ultrasound to switch on the agent (instead of using the hot water bath). The next section shows the measurement methods and results. The results indicate that the measured switched-on fluorescence lifetimes (τ_{on}) via the two methods were similar.

4.3.5 USF signal lifetime measurement

In the previous section it shows that it is feasible to select a proper time-gated window of signal acquisition to improve SNR in USF imaging. This is based on the assumption that the USF signal has a longer lifetime than that of the background. Although it was shown that both ADP(OH)$_2$-Bottom nanocapsule and ZnttbPc nanocapsule demonstrated a long lifetime when the samples were tested in the cuvette in a high temperature environment (i.e., $T > T_{th}$), a question remained whether the USF signal itself had a long lifetime. In the previous section, we assumed that the USF signal came from the contrast agents that were thermally "switched-on" due to a temperature rise by FU heating. In this experiment, we measured the fluorescence lifetime of a USF signal, in order to demonstrate whether the "ultrasonically switched-on" fluorescence had a lifetime similar to that of the "thermally switched-on" fluorescence. The sample configuration and the experimental setup was the same as that in Figure 4.13 (a). In this experiment, we tested the USF signal from ADP(OH)$_2$-Bottom in 5% F98 nanocapsule. The silicone tube was filled with ADP(OH)$_2$-Bottom in 5% F98 nanocapsule, and the cuvette was filled with ZnttbPc in 5% nanocapsule. Thus, the background had a strong-intensity but short-lifetime fluorescence. The FU transducer was focused on the silicone tube for acquiring the USF signal. We adopted a long exposure time (3 s) to get the USF signal. The experimental setup was basically the same as that in Figure 4.13 (a), Case 2, except that the FU transducer did not scan across the tube but acquired the USF signals from the tube at different time-gated windows.

This experiment followed three steps. In step 1, the ICCD camera measured the IRF of the system (when the cuvette and tube were first filled with water). The measurement principle is presented in Figure 4.3. The difference here is, the gate width t_w = 400 ps, the delay time interval Δt = 200 ps, and the measured gate time range t = 0 – 10 ns. In Figure 4.14, the solid blue line represents the normalized IRF of the system (i.e., the measured excitation laser pulse). In step 2, the system measured the strong-intensity background fluorescence (BF) pulse from the cuvette filled with ZnttbPc in 5% nanocapsule, which is the solid red line (normalized) in Figure 4.14. Its calculated lifetime is 0.26 ns (function y1, dash red line in Figure 4.14). Step 3 repeated the measurement in step 2, with the difference that a FU signal (Vpp = 130 mV, FU exposure time = 400 ms) came in. The FU signal was synchronized with each camera frame (camera exposure time = 3 s) that captured the fluorescence pulse within the designed time-gated window as in step 2. Thus, in step 3, the measured fluorescence pulse represents the BF pulse (from the cuvette) plus the USF pulse (from the tube). Then, this measured pulse in step 3 was subtracted from the BF pulse in step 2; the remainder was only the USF pulse from the tube. In Figure 4.14, the solid green line represents the normalized USF pulse after subtraction. Its calculated lifetime is 1.10 ns (function y2, dash green line in Figure 4.14). The result shows that the USF signal has a relatively long lifetime compared with that of the background (τ = 1.10 ns > 0.26 ns). It also shows the USF signal lifetime of ADP(OH)$_2$-Bottom nanocapsule is similar to the lifetime of the nanocapsule (τ = 1.02 ns as seen in Figure 4.7 (c)) in a high-temperature (i.e., $T = 40$ °C $> T_{th} = 31$ °C) water-bath environment.

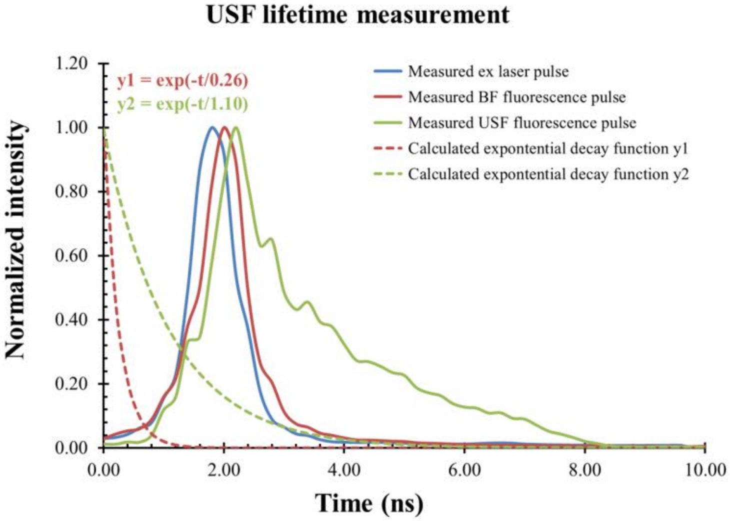

Figure 4.14 The measured lifetimes of the background fluorescence pulse, as well as the USF pulse which came from ADP(OH)$_2$-Bottom in 5% pluoronic F98 nanocapsule in the tube. [71]

4.4 Discussion

4.4.1 Experimental parameters vs. USF image quality

Based on the above results, we summarize how the experimental parameters affected the USF image qualities (signal strength, SNR, spatial resolution, and temporal resolution) in Table 4.3. Clearly, the increase (or optimization) of all the listed experimental parameters (except the sample thickness) can improve (or optimize) the signal strength and SNR, which is helpful to achieve high-quality USF images. However, care should be taken when manipulating these parameters because most of them may lead to degradation of spatial resolution (except for the gating delay and the sample thickness). The same conclusion obviously holds for the temporal resolution, although we have not discussed it much here. These experimental parameters can be classified into three groups: optical, acoustic, and sample-related parameters, all of which are either directly adjustable or related to specific experiments and therefore must be balanced or optimized to achieve a desired USF image.

Table 4.3[71]

Img. Para. / **Exp. Para.**	**Sig. Str. & SNR**	**Spa. Resl.**	**Temp. Resl.**
(optical) CCD camera recording time ↑	↑↓	↓↑	↓
(acoustic) FU power ↑	↑	↓	↓
(sample) Thickness ↑	↓	×	×
(optical) Gating delay ↑	↑↓ or ×	×	×
(optical) Total CCD exposure time ↑	↑	↓	↓

Exp. Para.: experimental parameters; Imag. Para.: image parameters; Sig. Str.: signal strength; Spa. Resl.: spatial resolution; Temp.Resl.: temporal resolution. ↑: increase; ↓: decrease; ↑↓: increase and then decrease; ↓↑: decrease and then increase; ×: not correlated;

4.4.2 Selecting appropriate USF contrast agents

Besides balancing and optimizing different experimental parameters, selecting appropriate USF contrast agents is also important in time-domain USF imaging. An excellent time-domain USF contrast agent may include high on-to-off ratios of both fluorescence strength (I_{on}/I_{off}) and lifetime (τ_{on}/τ_{off}) as well as USF signal strength itself (I_{on}). Similar to other USF imaging modes (such as continuous wave and frequency domain modes), an adjustable switching temperature threshold (T_{th}), a narrow temperature transition bandwidth (T_{BW}), and near-infrared excitation and emission wavelength (λ_{ex} and λ_{em}) are also desirable. These factors may be considered together rather than singly. For example, for time-domain USF imaging, I_{on}/I_{off}, τ_{on}/τ_{off} and I_{on} should be considered together. We have demonstrated that the ZnttbPc-based agent has a high ratio for both I_{on}/I_{off} (= ~ 46 folds) and τ_{on}/τ_{off} (= 15.76). Thus, the ZnttbPc-based agent is suitable for time-domain USF imaging because the background noise can be efficiently reduced via the gating delay method. However, this does not mean that the ZnttbPc-based agent would be a better choice than the ADP(OH)$_2$-Bottom-based agent in all cases. Although the ADP(OH)$_2$-Bottom-based agent has a relatively lower I_{on}/I_{off} (= ~ 17 folds) and a slightly changed lifetime (τ_{on}/τ_{off} = 1.05), it has a higher I_{on} than that of the ZnttbPc-based agent (I_{on}: 5.74×10^3 counts > 0.55×10^3 counts, based on the results in the previous section). Thus, the ADP(OH)$_2$-Bottom-based agent has a higher detection sensitivity. Although it may not benefit much for time-domain USF imaging, the ADP(OH)$_2$-Bottom-based agent is a good choice in those cases where the USF signal strength might be highly attenuated and hard to detect, such as in deep biological tissue.

4.4.3 Additional discussions for current USF imaging

The current USF system was built on a fluorescence microscope. The adopted objective lens was a 4× Nikon lens, which limited the field of view (FOV) to ~3.2 mm in diameter. This FOV was relatively small. If the USF signal comes from a sample with a thickness of a few millimeters or the scattering is not significant, this FOV may be enough to collect most USF photons emitted from the sample surface (see the USF scattering spot in Figure 4.6). However, when the USF photons are coming from a much thicker sample and/or the scattering is significant, a larger FOV should be adopted for maximal coverage of the USF scattering area, which would therefore increase collection efficiency. This can be achieved by adopting a new lens system and will be investigated in future.

Another consideration regarding time-domain USF imaging is the possible temporal expansion of the excitation and emission pulses caused by sample scattering effect. For example, although the ZnttbPc-based agent's fluorescence lifetime significantly increases from hundreds of picoseconds to a few nanoseconds after the fluorophores are switched on, the emission pulse will eventually be convolved with the optical impulse response function of the scattering medium after passing throughout. Thus, the emission pulse might broaden to a level when $\tau_{\mathrm{on}}/\tau_{\mathrm{off}}$ becomes low, which matters especially when implementing USF imaging in centimeter-deep biological tissue. How this scattering effect affects the gating method should be investigated in future. If this effect is significant, this potential issue may be addressed in two ways: (1) develop new USF contrast agents that not only have a high $\tau_{\mathrm{on}}/\tau_{\mathrm{off}}$ but also have a large τ_{on}; (2) use a model to quantify and/or deconvolve this scattering effect.

4.5 Conclusion

In this work, we developed an ICCD camera-based, time-domain USF imaging system. Using this system, we demonstrated its features and advantages for USF imaging. We also described the tradeoffs in USF imaging using this system and suggested strategies for improvement, including balancing the tradeoffs by changing experimental parameters (CCD camera recording time, FU power, imaging depth, and gate delay of ICCD camera) and selecting an appropriate USF contrast agent.

Chapter 5 Investigate signal identification algorithms to improve USF imaging qualities

5.1 Introduction

In Chapter 4, we demonstrated that the USF signal acquired in the ICCD camera-based time-domain USF imaging system was presented as a function of CCD camera recording time and also as a function of 2D spatial scattering spot. In the *Results* section 4.3.4.1 we presented the effect of CCD camera recording time on USF imaging quality (i.e., the recording time affected the spatial resolution and SNR of a USF image). However, we did not analyze the shape of a USF signal over the total recording time, which we term the temporal information of a USF signal. There is a possibility the temporal information provides extra details about the contrast agents' distribution in USF imaging and thus it could be utilized to further improve the USF image qualities (such as spatial resolution and SNR). For example, if we analyze the experimental data about USF imaging of a silicone tube in the phantom (referring to the experiments in Chapter 4), the shape of the USF signal acquired when FU was focused on the center of the tube might be different from that when FU was focused the edge of the tube. If a difference exists, we can investigate its underlying mechanisms and improve the USF imaging qualities based on the analysis. In addition, we have not taken advantage of the spatial information of a USF signal distributed on the tissue surface (i.e., the 2D scattering spot acquired in the camera). In the previous work in Chapter 4, we simply summed up all the USF photons acquired in the camera frame to present the USF signal intensity. However, the 2D scattering spot of the USF signal might also provide extra information about the imaging targets (i.e., the distribution of the contrast agents) and could be adopted for analysis and imaging quality improvement.

In this chapter, we investigated several signal identification algorithms, based on the temporal and spatial information of the USF signals acquired, to improve the image qualities (i.e., the spatial resolution and SNR of a USF image). First, we demonstrated that using the temporal information of the USF signals, the SNR of USF images could be improved by a correlation method.[65] Second, we characterized the shape of the normalized USF signal's temporal information in in three parameters: (1) the ascending slope; (2) the descending slope; and (3) the full-width-at-half-maximum (FWHM). By adopting an ascending-slope-weighted method, we improved the spatial resolution of USF images. Third, using the spatial information of the USF signals, we developed a completely new algorithm to plot a USF image: spatial back projection of USF scattering spots. By adopting this method, the spatial resolution was significantly improved.

We started analyzing the experimental data and investigated these algorithms from the USF imaging of a single silicone tube imbedded in the phantom presented in Chapter 4. Then, we conducted USF imaging experiments of more complicated silicone phantoms and tissue phantoms with multiple tubes (targets) as well as 2D structures. By these studies, we verified the feasibilities of applying these algorithms to improve USF imaging qualities. Overall, this chapter is focused on developing USF signal identification algorithms and improving the USF image qualities based on these algorithms. All the USF imaging experiments were conducted in the ICCD camera-based, time-domain USF imaging system developed in Chapter 4.

5.2 Methods

5.2.1 Sample configuration of silicon phantoms

The protocol of making a silicone phantom was the same as described in Chapter 2 and Chapter 4. The silicone kit was purchased from Factor II Inc. (VST-50: VerSilTal Silicone Elastomer). The kit includes two major components: silicone elastomer and catalyst. Basically, 4 mg titanium dioxide (TiO_2) was fully dissolved in 6 mL silicone catalyst by stirring for 20 mins and then mixed with 60 mL silicone elastomer. TiO_2 functions as light scatters in the silicone phantom; the estimated absorption coefficient $\mu_a = 0.03$, and the reduced scattering coefficient $\mu_{s'} = 3.5$ cm^{-1}.[64,65,81] The mixture was poured into a plastic container, and the silicone tube was inserted through the container. The amount of the poured mixture could be adjusted so that the silicone tube was imbedded at an appropriate depth. Then the sample was placed in a vacuum hood to remove the bubbles in the mixture. The silicone was solidified at room temperature for 12 hours. After that, the plastic container was peeled off, and the silicone phantom was ready to use.

In this study, we adopted several silicone phantoms for USF imaging and data analysis. The first one is a silicone phantom imbedded with a small *I.D.* (310 μm) tube, and its imaging depth is Z2 = 6 mm (i.e., the distance from the tube center to bottom surface where the camera is focused). This experiment was conducted in Chapter 4 and we analyzed the experimental data for imaging qualities improvement. The second one is a silicone phantom imbedded with a large *I.D.* (760 μm) tube, and its imaging depth is Z2 = 6 mm. The third one is a silicone phantom with two adjacent small *I.D.* (310 μm) tubes, and their imaging depth Z2 = 5 mm. The distance from the two tube centers is around ~ 800 μm. The fourth is a silicone phantom with three tubes (*I.D.* = 310 μm) with a shape of a triangle 2D structure. Their imaging depth Z2 = 5 mm. The last phantom we adopted is a porcine muscular tissue phantom attached to three tubes (*I.D.* = 310 μm) located on the surface of a silicone phantom, also with a shape of a triangle 2D structure. The imaging depth of the tube (i.e., the thickness of the porcine muscular tissue) is Z2 = 5 mm. The reduced scattering coefficient of the porcine tissue should be larger than $\mu_{s'}$ = 3.5 cm^{-1} so that the acquired USF signal would be more scattered in space in the FOV of the camera. This phantom was used to investigate that whether the signal identification algorithms would be feasible to improve USF imaging qualities when imaging a more highly-scattered medium.

5.2.2 Field of view of the camera

As described in Chapter 4, we adopted a 4× objective lens for USF imaging in previous experiments. Its FOV = ~ 3.2 mm. In this study, we changed the camera's FOV by adopting different objective lens. Correspondingly, a 2× objective lens provides a FOV = ~ 6.4 mm, and a 1× objective lens provides a FOV = ~ 12.8 mm. The different FOVs were adopted based on USF imaging of the size of different silicone phantoms and the size of the USF 2D scattering spots (which is related to the reduced scattering coefficient $\mu_{s'}$). The selection of a FOV will be described in the *Results* of each experiment.

5.2.3 Temporal information of a USF signal

As mentioned, the USF signal acquired in the ICCD camera was a function of CCD camera recording time. The different recording times not only provided different spatial resolutions of a USF image, but also provided the temporal information of a USF signal at a single scan point. For example, in Chapter 4 Figure 4.9 shows the USF profile of the silicone tube embedded in the silicone phantom. As stated previously, in this figure the USF strength at each scan point was counted from t = 1.8 s so the profile got the highest resolution. If we analyze the temporal information (i.e., t = 1.8 s, 2.4 s, 3.0 s, … 6.0 s) of these USF signals at different scan points (i.e., different x), we may find and utilize some temporal information to improve the USF image quality.

5.2.3.1 Correlation of a USF signal

First, the temporal information of a USF signal could be utilized to improve the SNR of a USF image by a correlation method.[65] When a USF signal was acquired, typically it increased and decreased with a few to tens of seconds in duration (based on the data in Chapter 4). When the noise was acquired, its shape was random and usually not correlated to the shape of a USF signal. Thus, by the correlation method, the background noise could be significantly removed. Figure 5.1 shows an example of the comparison between the non-correlated USF profile and the correlated USF profile from the same data in Figure 4.9. Figure 5.1 (a) shows the correlation coefficients at different x. The reference signal for correlation is from x = 0.00 mm. Figure 5.1 (b) is the non-correlated USF profile (which is the same as Figure 4.9), its SNR = 72.3, and FWHM = 0.80 mm. Figure 5.1 (c) is the correlated USF profile. In this figure at each x the correlation coefficient was multiplied with the signal strength. Its SNR = 137.4, and FWHM = 0.80 mm. Comparing Figure 5.1 (b) and (c) we found the SNR of the USF profile was significantly improved but the spatial resolution was the same. Thus, by the correlation method, it could help improve the SNR of a USF image.

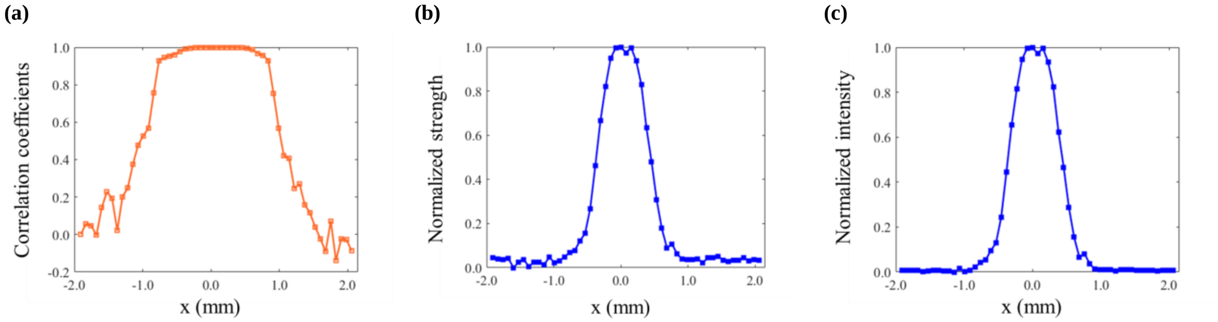

Figure 5.1 (a) Correlation coefficients at different x. The reference signal is the USF signal at x = 0.00 mm. (b) Non-correlated USF profile. (c) Correlated USF profile.

5.2.3.2 Characterization of a USF signal's temporal information

Meanwhile, we found the shapes of the USF signals were also different. Figure 5.2 shows the difference. In Figure 5.2 (a), it shows the normalized USF profile of the silicone tube, which is the same as Figure 5.1 (b). The three circles (in red, orange, and green color) represents the three scan points we analyzed. The red circle represents on the center of the profile (or tube), the orange one represents some distance away from the center (i.e., the scan point is nearby the FWHM of the profile), and the green one represents on the edge of the profile. If the USF signals as a function of recording time on these three scan points are normalized and put together, we could find their shapes are different. Figure 5.2 (b) shows their normalized curve. When the USF signal was acquired at x = 0.00 mm (i.e., the red circle on the center), the USF signal increased fast but decreased slow, and its duration was the longest. In the opposite, when the USF signal was acquired at x = -0.61 mm (i.e., the green circle on the edge), the USF signal increased slow but decreased fast, and its duration was the shortest. At x = -0.38 mm (i.e., the orange circle nearby the FWHM), the USF signal had a medium increase, decrease and duration. The result clears shows that the shape of a

USF signal was highly correlated to the location of the FU signal (i.e., the scan point). Thus, the shape of a USF signal should be utilized to improve a USF image.

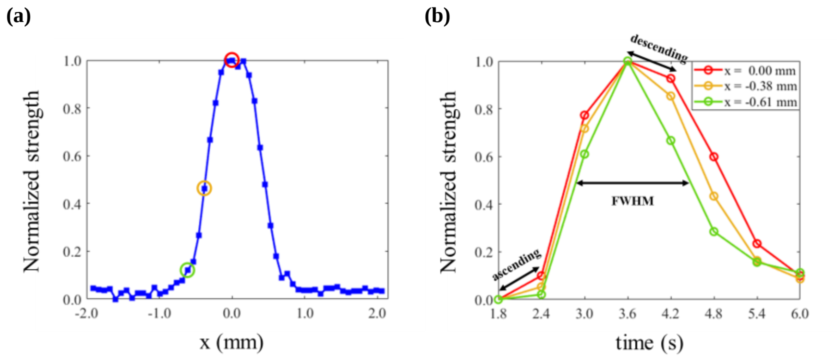

Figure 5.2 (a) Non-correlated USF profile. (b) The normalized USF signals at different x.

We characterized the shape of the normalized USF signal in three parameters: (1) the ascending slope of the start of the signal. Typically, it is the slope from t = 1.8 s to t = 2.4 s, as shown in Figure 5.2 (b); (2) the descending slope when the signal starts to decrease. Typically, it is the slope from the time at peak (t_{peak}) to the next camera recording time. As shown in Figure 5.2 (b), in this example it is the slope from t = 3.6 s to t = 4.2 s; and (3) the FWHM of the signal, which represents the duration of the USF signal. Figure 5.3 shows (a) the ascending slope, (b) the descending slope, and (c) the FWHM of the USF signals as a function of x (the different scan points). Correspondingly, Figure 5.3 (d), (e), and (f) shows the normalized USF profiles after it was multiplied with (a), (b), and (c) as well as the correlation profile (Figure 5.1 (a), with a correlation threshold ≥ 0.8). Thus, Figure 5.3 (d) represents the ascending-slope-weighted correlated USF profile; Figure 5.3 (e) represents the descending-slope-weighted correlated USF profile; and Figure 5.3 (f) represents the FWHM-weighted correlated USF profile. The results show that compared with correlated USF profile (Figure 5.1 (c)), the ascending-slope-weighted correlated USF profile and the FWHM-weighted correlated USF profile increased their spatial resolution, while the descending-slope-weighted correlated USF profile provided a worse spatial resolution. Their FWHM was 0.66 mm, 0.87 mm, 0.76 mm, correspondingly. To summarize, we conclude that the ascending-slope-weighted correlated USF profile provides the best spatial resolution as well as the SNR. Thus, utilizing the temporal information of a USF signal, we adopted the ascending-slope-weighted correlated USF profile, in order to improve the USF imaging quality to the best. More examples of this improvement would be demonstrated in the *Results* section.

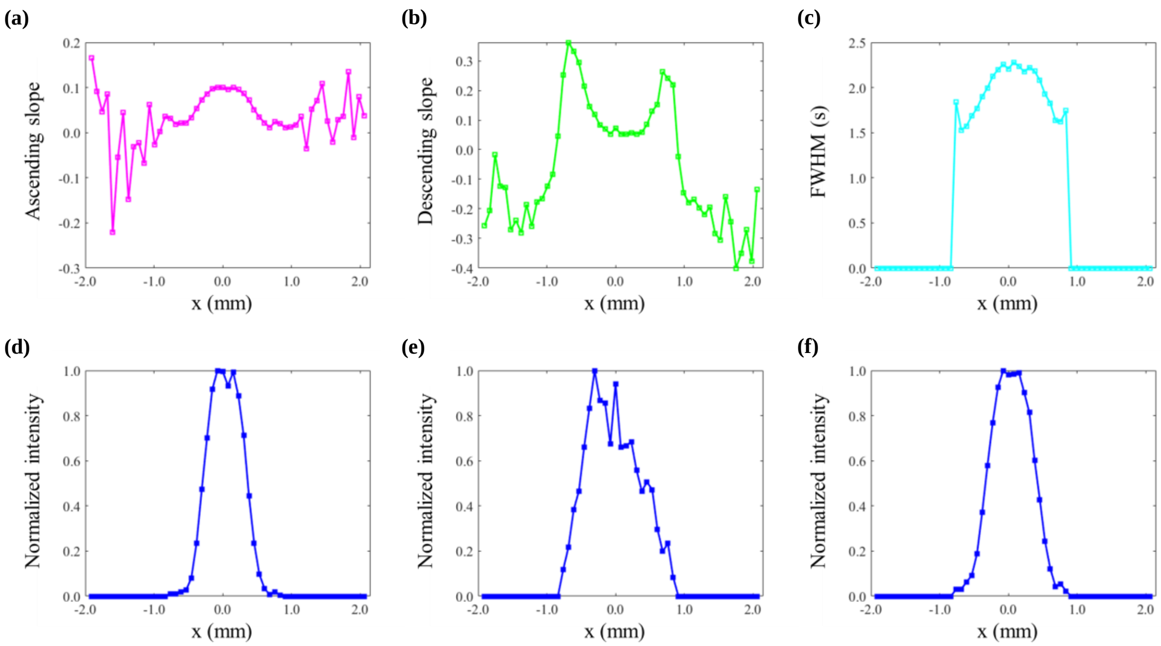

Figure 5.3 (a) Ascending slopes of normalized USF signals at different x. (b) Descending slopes of normalized USF signals at different x. (c) FWHMs of normalized USF signals at different x. (d) Ascending-slope-weighted correlated USF profile. (e) Descending-slope-weighted correlated USF profile. (f) FWHM-weighted correlated USF profile.

5.2.4 Spatial information of a USF signal

In chapter 4, it shows the USF signal acquired in the ICCD camera was represented as a 2D spatial scattering spot because the emitted USF photons came from the scattering phantom with a few millimeters to centimeters imaging depth. It is worth mentioning that the USF signal strength was calculated by summing up the USF photons from the 2D scattering spot and the spatial coordinate of each USF signal was determined by the HIFU transducer, due to that the USF imaging adopted a point-to-point scan method. However, in our previous work, the spatial information of the USF signal from the ICCD camera was not fully utilized. In this section, we focused on how to use the 2D spatial information of the USF scattering spot for USF imaging.

5.2.4.1 Spatial back projection of a USF signal’s spatial information

We started analyzing the 2D scattering spots (i.e., the USF signals) from the same silicone phantom in the previous section. Figure 5.4 (a) shows the set up diagram of the FU transducer and the silicone phantom, which is similar to that in Figure 4.4 (Z1 = Z2 = 6 mm). The FU transducer had a scanning step size = 76.2 μm with a total scanning range = 3.962 mm (i.e., the total number of scan points = 53). The red crosses represent the scanning points. HIFU central position is initially localized at the center of tube (x = 0.00 mm). We analyzed the USF signals acquired at t = 3.0 s (i.e., the second camera frame recorded after FU signal was sent, with background subtracted) at different scan points. Figure 5.4 (b) shows the USF signals acquired (in form of 2D scattering spots, t = 3.0 s with background subtracted) at these scanning points. It is easy to understand that when the FU transducer was focused on the tube (x = 0.000 mm) or nearby the tube (e.g., x = -0.152 mm), there was a USF signal. When the FU transducer was far away from the tube (e.g., x = -1.095 mm), there was no USF signal. While the FU transducer scanned across the tube and the USF profile of the tube was acquired with a FWHM around hundreds of microns up to more than 1 mm (at least 0.80 mm when t = 2.4 s was counted, as discussed in chapter 4) due to the size of the thermal volume generated by the FU focus (which is usually a few hundreds of microns), it was found that the scattering spots barely moved in the center of the camera frame.

To better understand this, we assume that the size of the tube *I.D.* (310 μm) was relatively small compared to the size of thermal volume (the lateral focal size of the 2.5 MHz FU transducer at half-amplitude = ~ 0.8 mm), so that the tube could be viewed as a point source in this experiment. As a result, when the FU transducer switched on the fluorescence in the tube wherever the transducer was located (either focused on the tube or on the edge of the tube), the switched-on fluorescence from tube did not move along with the transducer since it was a point source and its location was fixed in the phantom. Thus, the scattering spots (i.e., the USF signals) did not move along with the transducer too. If the phantom has a uniformed distribution of scattering coefficient as well as an even surface (which is true in this case), we assumed those switched-on agents are located right below the geographical center of the scattering spot (i.e., the point source), with no spatial shifts on x-y plane. Correspondingly, if we back project all the geographical centers of the scattering spots, they should be located on the tube.

In a more realistic case, the tube had a finite size (*I.D.* = 310 μm in this case) so that the back-projected centers should have a spread-function across the tube (along x-axis). Here we term the spread-function as the spatially back-projected USF image. It is worth mentioning here that the size of spatially back-projected USF profile depends on the size of the tube. Instead of adopting the FU transducer scanning steps as the spatial coordinate, this method provides an algorithm to acquire a USF image, with a new spatial coordinate metric, based on the spatial information acquired in the ICCD camera.

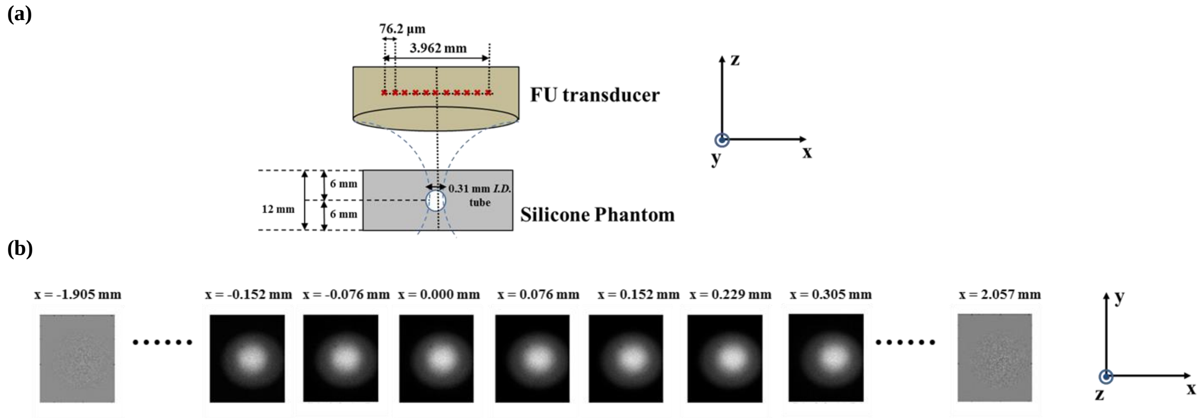

Figure 5.4 (a) Set up diagram of the FU transducer and the silicone phantom. The FU transducer had a scanning step size = 76.2 µm with a total scanning range = 3.962 mm (i.e., the total number of scan points = 53). (b) USF signals acquired at these scanning points.

5.2.4.2 Identification of a single scattering spot

When USF imaging of a phantom with multiple tubes or a 2D structure, some scattering spots from different targets (tubes) would overlap with each other. Thus, it requires segmentation of these overlapped spots before we back-project their centers. It is difficult to determine the threshold and the contour of a separate scattering spot during segmentation. A typical way is that we adopted a standard USF scattering spot from a single tube as the reference, and used the reference to determine the separation of overlapped contours. The temporal information of a USF signal in the 2D space would also help in identification of USF signals from multiple targets (tubes). More discussion will be presented in the *Results* based on several imaging phantoms. It is worth mentioning here that, we did not conclude a universal method for the identification algorithm. The thresholding and segmentation algorithms in this work varied case by case, based on our data analysis in each case. In the future, in order to develop the spatially back-project USF imaging technique, USF tomography should be investigated which includes the forward simulation model and the backward imaging model. We will investigate this in our future work.

5.2.4.3 Deviation of back projection

A back-projected center is not always located the position of the emitted fluorophores because of deviation. The deviation depends on four parameters: the heterogeneity of the scattering in the phantom, the roughness of the surface, the scattering coefficient, and the imaging depth. Typically, if there is the more heterogeneity, the more roughness, the higher scattering coefficient, and the larger imaging depth, there is a large deviation. In this study, we adopted the silicone phantom which has a good homogeneity, a flat top surface, a relatively low scattering coefficient ($\mu_s' = 3.5$ cm^{-1}, $\mu_a = 0.03$ cm^{-1}) and a relatively small imaging depth (5-6 mm) for a first-step investigation. The deviation of a back-projected center from the silicone phantom was calculated by counting the deviation of the centers of the repetitively acquired USF signals when FU signal was focused on the center of tube. The deviation is ~ 10 μm in the silicone phantom. After the deviation was calculated, the spread function of the centers was convolved with the deviation and a final spatially back-projected USF image was acquired. Figure 5.5 shows an example of the spatially back-projected USF imaging profile of the silicone tube in the silicone phantom adopted in the section. In the experiments, we also adopted a porcine tissue phantom for study, its deviation should be larger and will be discussed in the *Results*.

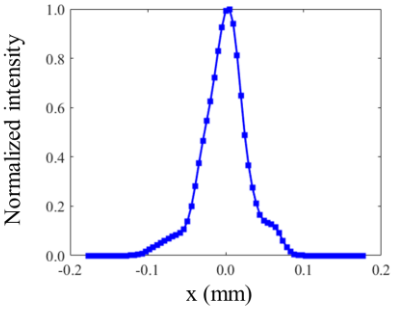

Figure 5.5 Spatially back-projected USF imaging profile of the silicone tube.

5.3 Results

5.3.1 USF imaging of a silicone phantom imbedded with a small *I.D.* (310 μm) tube

In this section, we first presented the improvements of the USF image of the silicone phantom imbedded with a small *I.D.* (310 μm) tube, same as the example described in the *Methods*. Figure 5.6 shows the USF profiles processed by different algorithms. The first line represents the regular USF profile (equivalent to that in Figure 4.9). Its SNR = 72.3, and FWHM = 0.80 mm. The second line represents the correlated USF profile (equivalent to that in Figure 5.1 (c)), and its SNR was better than that of the regular one. Its SNR = 137.4, and FWHM = 0.80 mm. The third line represents the ascending-slope-weighted correlated USF profile (equivalent to that in Figure 5.3 (d)), and its spatial resolution was better than that of the first two. Its FWHM = 0.66 mm. The fourth line represents the spatially back-projected USF profile. The signal strength was presented in log compression for a better visualization. It shows its spatial resolution was significantly improved compared with the previous three. In the analysis of the spatial back-projected USF profile, it is more reasonable to use the bottom width to represent the measured size of the tube. Its full-width-at-one-percent-of-the-maximum (FWPM) = 0.19 mm. The fifth line represents the real size of the tube (*I.D.* = 0.31 mm). All profiles were normalized.

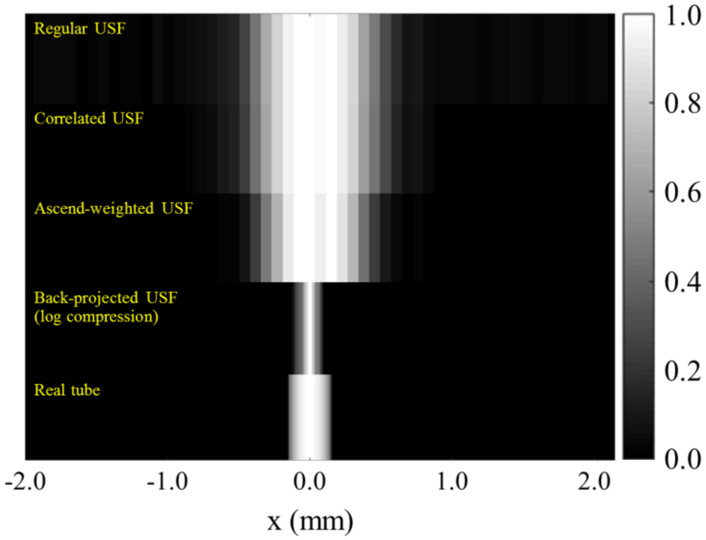

Figure 5.6 USF profiles of the silicone tube (*I.D.* = 0.31 mm) processed by different algorithms.

From this figure, we find the correlation method improved the SNR of the USF image, and the ascending-slope-weighted helped improve its spatial resolution. The spatially back-projection algorithm provides the highest resolution, and its size was even smaller than the real size of the tube. This is probably because when only the fluorophores nearby the edge of the tube were switched on and provided a USF signal, the signal intensity was usually very weak and could not be detected as a scattering spot. Thus, those fluorophores nearby the edge of the tube could not be back-projected and the width of the spread function was smaller than the width of the real tube.

5.3.2 USF imaging of a silicone phantom imbedded with a large *I.D.* (760 µm) tube

In the *Methods*, we proposed that the size of back-projected USF profile (i.e., the spread function) is dependent of the size of the silicone tube. In order to verify this and the reliability of all the algorithms, in this experiment we analyzed USF imaging of a silicone phantom imbedded with a large *I.D.* (760 µm) tube. The sample configuration of the silicone phantom was similar to that which was imbedded a small *I.D.* (310 µm) tube in the previous section. Its imaging depth is also the same (Z1 = Z2 = 6 mm). Its $\mu_s' = 3.5\ cm^{-1}$ and $\mu_a = 0.03\ cm^{-1}$. In USF imaging, the FU transducer scanned across the tube with a scanning step size = 127 µm with a total scanning range = 6.604 mm (i.e., the total number of scan points = 53). The FU power Vpp = 130 mV.

Figure 5.7 shows the corresponding USF imaging profiles processed by different algorithms. Similarly, the first line represents the regular USF profile. Its SNR = 90.9, and FWHM = 1.24 mm. The second line represents the correlated USF profile, and its SNR was better than that of the regular one. Its SNR = 320.6, and FWHM = 1.23 mm. The third line represents the ascending-slope-weighted correlated USF profile, and its spatial resolution was better than that of the first two. Its FWHM = 1.03 mm. The fourth line represents the spatially back-projected USF profile. The signal strength was presented in log compression. Its FWPM = 0.55 mm. The fifth line represents the real tube. All profiles were normalized.

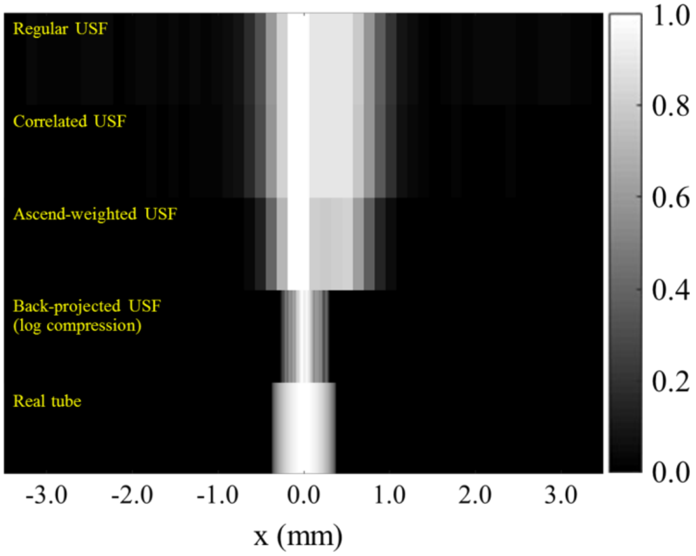

Figure 5.7 USF profiles of the silicone tube (*I.D.* = 0.76 mm) processed by different algorithms.

The results were similar to that in *Section* 5.3.1. When adopting the temporal information of the USF signals, the ascending-slope-weighted correlated USF profile achieved the best SNR and spatial resolution. When adopting the spatial information of the USF signals, the spatially back-projected USF profile provides a highest spatial resolution. Its width (i.e., FWPM = 0.55 mm) was larger than that of imaging a small *I.D.* (310 µm) tube (i.e., FWPM = 0.19 mm, see the fourth line in Figure 5.6). This result verified that the size of back-projected USF profile (i.e., the spread function) is dependent of the size of the silicone tube and this algorithm is trustworthy. Of course, its size was also smaller to the size of the real tube (760 µm) due to the weak USF signal when it was only from nearby the edge of the tube.

5.3.3 USF imaging of a silicone phantom imbedded with two adjacent tubes

As described in the *Methods*, when applying the spatially back-projected algorithm in USF imaging, it is a challenge to identify a signal scattering spot (which should be from one fluorescence point) when there are multiple imaging targets (e.g., multiple tubes). We proposed that segmentation of the overlapped scattering spots can be achieved by adopting a standard reference signal (e.g., a 2D USF scattering spot from a single small *I.D.* tube) and also by using the temporal information of the 2D USF scattering spots. In this section, we conducted USF imaging of a silicone phantom imbedded with two adjacent tubes (both their *I.D.* = 310 μm) to investigate the proposed method. Also, other algorithms (correlated USF and ascend-weighted correlated USF) were carried out to verify that they could improve the USF imaging qualities (spatial resolution and/or SNR) as well. The sample configuration of the silicone phantom was similar to the previous except that it was imbedded with two adjacent tubes (both their *I.D.* = 310 μm). Its imaging depth is Z1 = 6 mm (on the FU transducer side), and Z2 = 5 mm (on the detector side). Its $\mu_s' = 3.5$ cm^{-1} and $\mu_a = 0.03$ cm^{-1}. In USF imaging, the FU transducer scanned across the tube with a scanning step size = 76.2 μm with a total scanning range = 5.563 mm (i.e., the total number of scan points = 74). The FU power Vpp = 130 mV. The USF imaging results were verified with a B-mode ultrasound image of the two tubes (when filled with air) in the phantom.

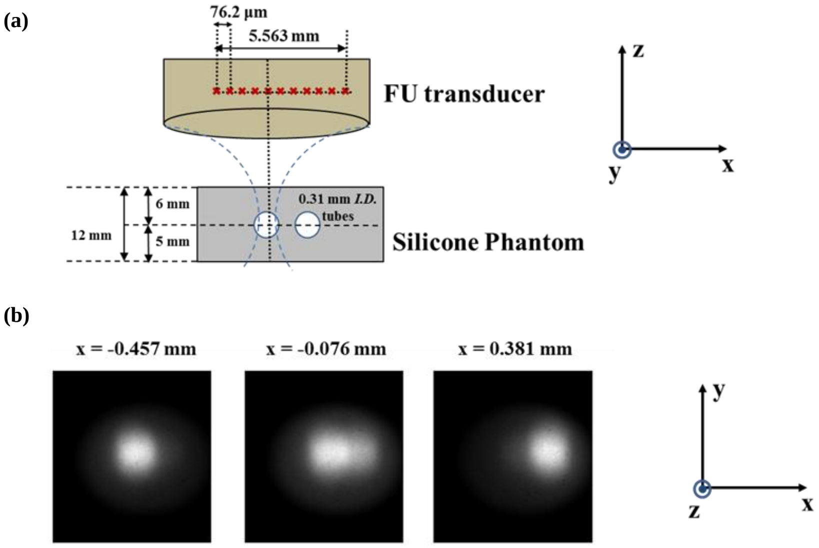

Figure 5.8 (a) Set up diagram of the FU transducer and the silicone phantom. The FU transducer had a scanning step size = 76.2 µm with a total scanning range = 5.563 mm (i.e., the total number of scan points = 74). (b) USF signals acquired at three scanning points: 1) when FU was focused on the first tube; 2) when FU was focused in between two tubes (x = -0.076 mm); 3) when FU was focused on the second tube.

Figure 5.8 (a) shows the sample configuration of the silicone phantom and the set-up of the FU transducer. Figure 5.8 (b) shows examples of the USF signals acquired. These images represent the USF signals were acquired at a CCD recording time = 3.0 s (i.e., the second frame after FU signal was sent, with background subtracted). The first image was acquired when FU was focused on the first tube (x = -0.457 mm), the second image was acquired when FU was focused in between two tubes (x = -0.076 mm), and the third image was acquired when the FU was focused on the second tube (x = 0.381 mm). The images clear show that the 2D scattering spots moved from the left (where the first tube was located) to the right (where the second tube was located) when the FU scanned across. When the FU was focused in between the two tubes, the USF signal (i.e., the second image) has two scattering spots which came from both tubes. It shows that the two spots partially overlapped with each other. If we count this overlapped USF signal as one large scattering spot and back-project its overall center using the spatially back-project algorithm (i.e., without a segmentation method), we can still get a USF imaging profile of the two tubes. Figure 5.9 (a) shows the USF imaging profile of the two tubes by the spatially back-projection algorithm without overlapped-spots-segmentation.

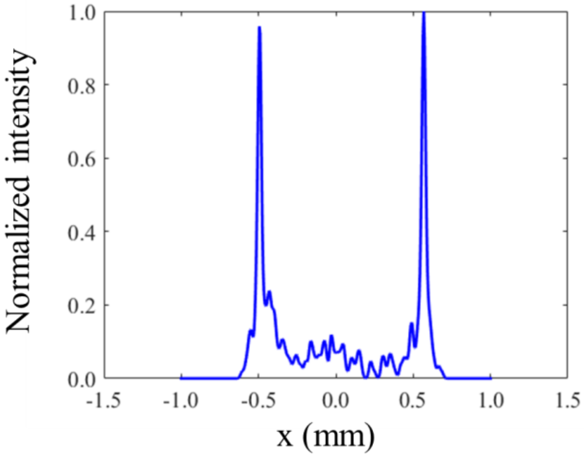

Figure 5.9 USF imaging profile of the two tubes in the silicone phantom by the spatially back-projection algorithm without overlapped-spots-segmentation.

Figure 5.9 shows that the two tubes are still separated by adopting the spatially back-projection algorithm. However, some back-projected centers fall in between the two tubes. This is reasonable because the USF signals acquired in between them had signals from both tubes and their 2D scattering spots were overlapped. Without segmentation of the overlapped spots, these back-projected centers did not contribute to each tube but instead fell in between the two tubes. To address this issue, we analyzed the contours of the overlapped spots for the purpose of segmentation. As known, we first picked up a standard reference USF signal acquired when FU was focused on the first tube (i.e., the first image acquired at x = -0.457 mm in Figure 5.8 (b)). Second, we determined the size (diameter) of the standard signal. In addition, we introduced the temporal information of the USF signal in 2D space. Figure 5.10 (a) shows an example of one overlapped USF signal acquired at x = -0.076 mm (at t = 3.0 s). This image is the same as the second image in Figure 5.8 (b) except it that multiplied with a mask of the temporal information FWHM (unit: s). It clearly shows that although the two spots from the two tubes were overlapped with each other, their signal durations (i.e., FWHM) were totally different since the FU focus (at x = -0.076 mm) was a little closer to the first tube (at x = -0.457 mm) than to the second tube (at x = 0.381). Thus, by the difference in temporal information, and also by using the standard reference signal, we could separate the two fluorescence spots from the two tubes. Thus, each spot is segmented and its center could be back-projected to each tube. Figure 5.10 (b) shows USF imaging profile of the two tubes by the spatially back-projection algorithm with an overlapped-spots-segmentation method.

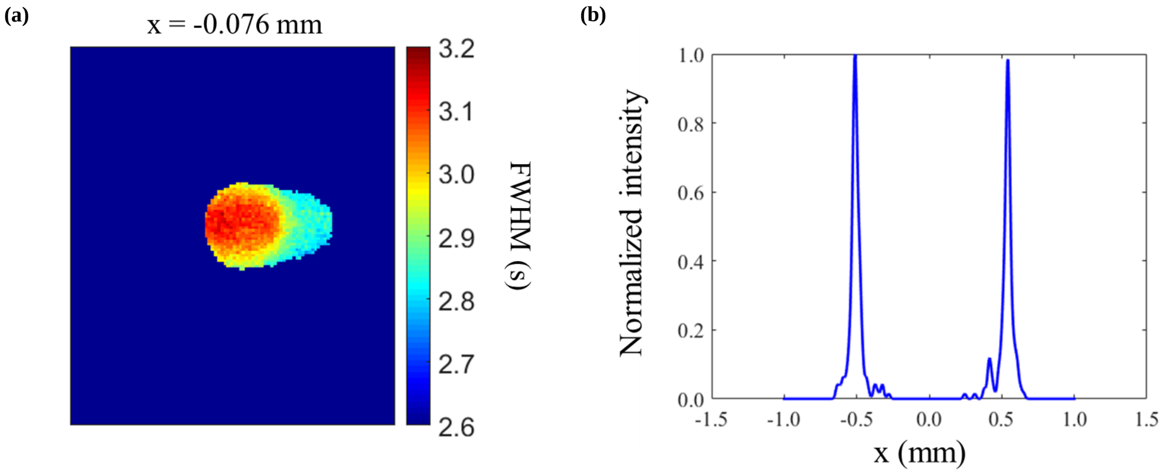

Figure 5.10 USF imaging profile of the two tubes in the silicone phantom by the spatially back-projection algorithm without overlapped-spots-segmentation.

In Figure 5.10 (b), it clearly shows that by adopting the segmentation method, the overlapped USF signals acquired in between the two tubes are spatially separated and their centers are back-projected to each tube on the side rather than back-projected in the center between the tubes (comparing to Figure 5.9). Using the segmentation method in spatially back-projection algorithm provides a more realistic USF imaging profile of the two tubes.

Figure 5.11 shows the corresponding USF imaging profiles together, processed by different algorithms. Similar to previously, the first line represents the regular USF profile. We used the first tube's USF profile to present the spatial resolution of this image, which has a FWHM = 0.59 mm. The SNR of the overall profile is 35.2. The second line represents the correlated USF profile, and its SNR was better than that of the regular one, which is 88.7. The first tube's USF profile in this image has a FWHM = 0.56 mm, similar to the previous. The third line represents the ascending-slope-weighted correlated USF profile, and its spatial resolution was better than that of the first two. The first tube's USF profile has a FWHM = 0.36 mm. The fourth line represents the spatially back-projected USF profile without adopting the segmentation method. The signal strength was presented in log compression. The fifth line represents the spatially back-projected USF profile with the segmentation method. The signal strength was presented in log compression. It shows the two imaged tubes were separated compared to that in the fourth line. The first tube's USF profile in this image has a FWPM = 0.24 mm. The sixth line represents the ultrasound image of the two tubes when they were filled with air. The same FU transducer was adopted for the ultrasound image. The seventh line represents the real tube. All profiles were normalized.

Figure 5.11 clearly shows that by adopting the correlation method (the second line) and the ascending-slope-weighted method (the third line), there was improvement of the SNR (by the correlation method) and also the spatial resolution (by the ascending-slope-weighted method) in the USF image. Meanwhile, adopting a spatially back-projected algorithm, the USF imaging achieved the highest resolution (FWPM of the imaged first tube is 0.24 mm). Similar to previously, the width of the imaged tube is still smaller than its real size (0.31 mm).

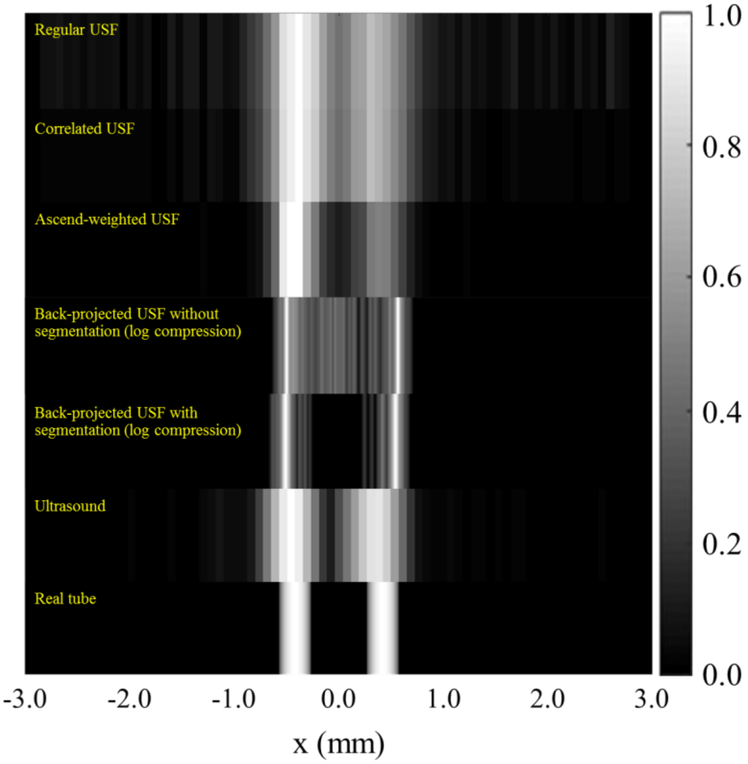

Figure 5.11 USF profiles of the two adjacent silicone tubes (*I.D.* = 0.31 mm) in the silicone phantom, processed by different algorithms, and also ultrasound image when the two tubes were filled with air.

5.3.4 USF imaging of a silicone phantom imbedded with multiple tubes in 2D

In this section, we conducted 2D USF imaging of a silicone phantom imbedded with multiple tubes in a 2D structure. Figure 5.12 (a) shows the sample configuration of the tubes from top view. Three silicone tubes (shown as white lines, their *I.D.* = 0.31 mm) were placed in a 2D triangle structure at the same z position and imbedded in the silicone phantom. The tubes' depths are Z1 = 5 mm (detector side) and Z2 = 6 mm (FU transducer side). The FU was focused on the tube on z direction for USF imaging. The FU scanning step size is 0.381 mm on both x and y direction. The scanning area is x = 4.572 mm (i.e., 13 points) and y = 5.334 mm (i.e., 15 points). The red dots represent the USF scanning points in 2D. Figure 5.12 (b) shows the cross-section top view of micro-CT image of the silicone phantom when the tubes were filled with the CT contrast agent solution ExiTron nano 12000. The dark dots were the hollow caves caused by the needles that were used to anchor the tubes when making the silicone phantom. The needles were already removed. Figure 5.12 (c) represents the diffusive fluorescence image detected from the surface of the phantom by the camera. The USF contrast agent solution ADP(OH)$_2$_Bottom in 5% pluronic F98 nanocapsule was filled in all three tubes. It shows the fluorescence was diffusive and three tubes could be separated. Note that we used a 2× objective lens (FOV = ~ 6.4 mm) for fluorescence imaging and USF imaging. Figure 5.12 (d) represents the ultrasound image of the three tubes when they were filled with air. The same FU transducer was adopted for ultrasound imaging. The three hollow needle caves on the side of the tubes were also visible in Figure 5.12 (d) (comparing to 5.12 (b)). The ultrasound image was normalized and presented in grey colorbar.

In USF imaging, the FU power was Vpp = 130 mV, and the FU exposure time was 400 ms. The CCD camera exposure time was 200 ms in this experiment. All other experimental parameters were kept the same as previous. Figure 5.12 (e) represents the regular USF image of the phantom. The USF signals acquired at the first recorded camera frame after FU signal was sent (t = 1.5 s here, with background subtracted) was counted as the signal strengths, which provides the highest spatial resolution of a regular USF image (i.e., Figure 5.12 (e)). If we count the lower left corner area of the image (4 × 4 pixels) as the background, the SNR of this image is 78.7. Figure 5.12 (f) represents the correlated USF image. Its SNR is 91.7. Comparing Figure 5.12 (e) and (f), it shows the correlation method improve the SNR of the USF image. However, its spatial resolution remains similar. Figure 5.12 (g) represents the ascending-slope-weighted correlated USF image. It shows the spatial resolution is some better than the previous two (the tubes' profiles are narrower). Due to the fact that the three tubes were difficult to separate in the three USF images, here we did not compare their spatial resolution based on the FWHM of each imaged tube. The last image (h) in Figure 5.12 represents the spatially back-projected USF image. The back-projected centers were convolved with a deviation mask (i.e., 2D Gaussian function, sigma = ~ 10 μm, similar to previously in processing 1D USF profiles). The signal intensity in the image is presented in log compression for a better visualization. This image provides a best spatial resolution and a good separation of the tubes in visualization (FWHM is not calculated here too). All the USF images (Figure 5.12 (e) – (h)) were normalized and presented in hot colorbar.

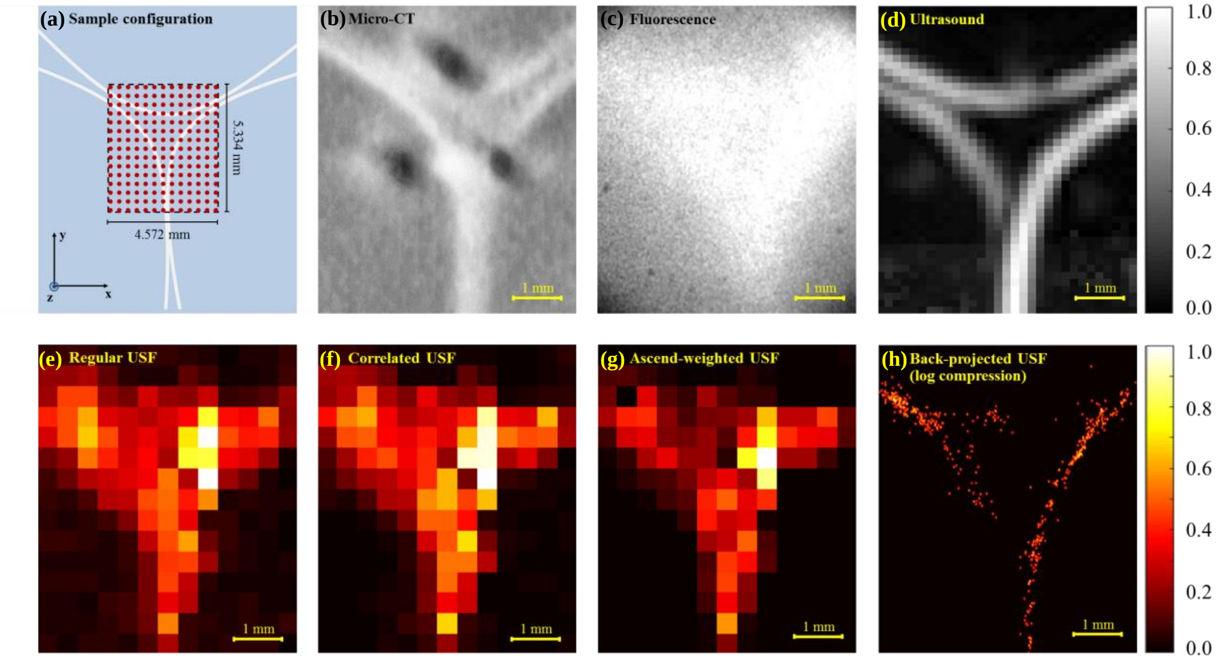

Figure 5.12 (a) Sample configuration of the silicone phantom. (b) Cross-section top view of micro-CT image of the silicone phantom when the tubes were filled with the CT contrast agent solution (ExiTron nano 12000). The dark dots were the hollow caves caused by the needles that were used to anchor the tubes when making the silicone phantom. The needles were already removed. (c) Diffusive fluorescence image detected from the surface of the phantom by the camera. (d) Ultrasound image of the three tubes when they were filled with air. (e) – (h) USF images of the three silicone tubes (*I.D.* = 0.31 mm) in a 2D triangle structure in the silicone phantom, processed by different algorithms.

5.3.5 USF imaging of a tissue phantom imbedded with multiple tubes in 2D

In this section, we conducted 2D USF imaging of a porcine muscular tissue phantom attached with multiple silicone tubes in a 2D structure. Figure 5.13 (a) shows the sample configuration of the phantom. Three silicone tubes (shown as white lines, their *I.D.* = 0.31 mm) were placed in a 2D triangle structure at the same z position and imbedded on top surface of a silicone phantom (μ_s' = 3.5 cm^{-1}, μ_a = 0.03 cm^{-1}.). A piece of porcine muscular tissue with a thickness of 5 mm was attached to the silicone phantom on the detector side. Thus, the fluorescence from the tube scattered into the tissue until it was detected by the camera on the other surface of the tissue. On the FU transducer side, the silicone has a thickness of 6 mm. In a simple word, the three tubes' depths are: Z1 = 5 mm on the detector side with a porcine muscular tissue medium, and Z2 = 6 mm on the FU transducer side with a silicone medium. Usually, the porcine muscular tissue has a higher scattering coefficient and the fluorescence would be more diffusive. We adopted a 1× objective lens (FOV = ~ 12.8 mm) for fluorescence imaging and USF imaging. Figure 5.13 (b) shows the diffusive fluorescence image of the phantom (on porcine tissue side) when the three tubes were filled with the USF contrast agents. Compare to Figure 5.12 (c), it shows the porcine tissue was a more scattering medium (with the same thickness = 5 mm) and the fluorescence from the three tubes could not be separated from each other totally.

In USF imaging, the FU power was Vpp = 130 mV, and the FU exposure time was 400 ms. The CCD camera exposure time was 100 ms in this experiment. All other experimental parameters were kept the same as previous. Figure 5.13 (c) represents the regular USF image of the phantom. The USF signals acquired at the first recorded camera frame after FU signal was sent (t = 0.75 s here, with background subtracted) was counted as the signal strengths, which provides the highest spatial resolution of a regular USF image (i.e., Figure 5.13 (c)). If we count the upper right corner area of the image (4 × 1 pixels) as the background, the SNR of this image is 70.4. Figure 5.13 (d) represents the correlated USF image. Its SNR is 76.9, which is slightly improved comparing to that of Figure 5.13 (c). The improvement is not significant because the counted background area is very close to the tubes (although that's the farthest area we could select) and their signals (as a function of time) were still some correlated to a standard USF signal. Meanwhile, its spatial resolution remains similar. Figure 5.13 (e) shows the ascending-slope-weighted correlated USF image. It shows the spatial resolution is some better than the previous two (the tubes' profiles are narrower). Here we did not compare their spatial resolution based on the FWHM of each imaged tube. The last image (Figure 5.13 (f)) is the spatially back-projected USF image. The back-projected centers were convolved with a deviation mask (i.e., 2D Gaussian function, sigma = ~ 40 μm, calculated based on the standard deviation of repetitive USF spots in this experiment). Due to the fact the porcine muscular tissue scatters more than the silicone phantom, the USF 2D spots have a large size (FWHM = ~ 8 mm) and so does the deviation of the back-projected centers (sigma = ~ 40 μm). Also, the highly scattering effect makes the USF signal from different targets (i.e., tubes) more difficult to separate in space as well as in time. Here we term this phenomenon as USF signal chaos. Although we may still apply the spatially back-projection algorithm to acquire a USF image (i.e., Figure 5.13 (f)), in this case its spatial resolution was usually worse than that in the previous case (i.e., Figure 5.12 (h)) as well as the regular USF images (i.e., Figure 5.13 (c)–(e)).

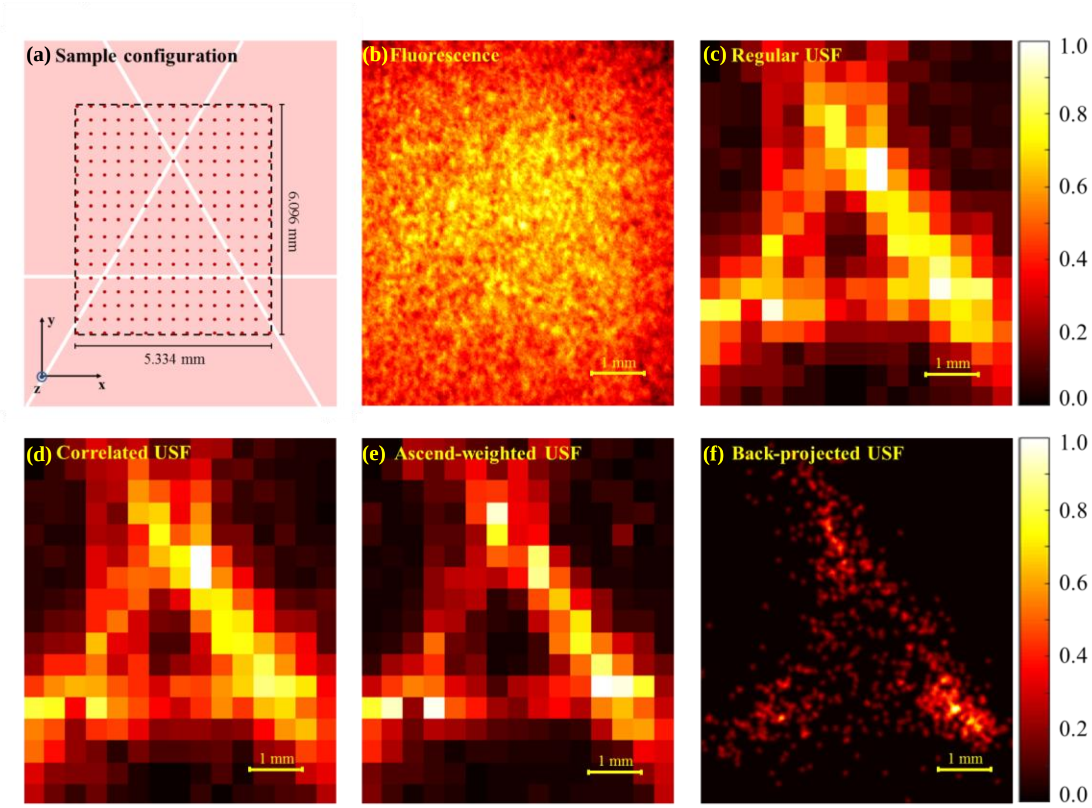

Figure 5.13 (a) Sample configuration of the porcine muscular tissue phantom. The three silicone tubes imbedded in the phantom has a 2D triangle structure and their *I.D.* = 0.31 mm. (b) Diffusive fluorescence image detected from the surface of the phantom by the camera. (c) – (f) USF images of the three silicone tubes in the tissue phantom, processed by different algorithms.

5.4 Discussion

5.4.1 USF imaging qualities

In this study we mainly investigated several algorithms to improve USF imaging qualities, especially spatial resolution and imaging contrast (SNR), based on the temporal and spatial information of the USF signals acquired in the ICCD camera-based time-domain USF imaging system. The results show that the correlation method could improve the SNR of a USF image and the ascending-slope-weighted method could improve the spatial resolution of a USF image in all cased presented. The results also show that the spatially back-projection method provides a significantly improved spatial resolution of a USF image, especially in the silicone phantom with a relatively small

μ_s' (= 3.5 cm^{-1}) as well as a small imaging depth (~ 5–6 mm). The requirement of applying all these algorithms is that it is necessary to acquire a complete USF signal over time (i.e., acquire a USF signal until its intensity decreases back to the background level) so that it has sufficient temporal information and also spatial information (i.e., statistically-enough USF 2D spots). Nevertheless, in USF imaging, typically, we do acquire a USF signal until its intensity decreases back to the background level before moving to the next scan point. It is worth mentioning that in Chapter 4, we discussed several tradeoff relationships about balancing the USF imaging qualities (i.e., spatial resolution, temporal resolution, and SNR) by adjusting different experimental parameters. Unlike Chapter 4, Chapter 5 developed several algorithms to improve one USF imaging quality parameter (either the spatial resolution or SNR) without sacrificing another, because these algorithms simply depend on the already-acquired data rather than the adjustment of the experimental settings. In other words, this work provides extra benefits for improving a USF image.

5.4.2 Limitations

In Chapter 4, for the first time we talked about acquiring a USF signal represented in 2D information in a camera-based USF imaging system. In Chapter 5, we talked about spatial back-projection algorithm which uses the spatial information and sometimes also the temporal information (see Figure 5.10 (a)) of the USF signals to require a USF image. Based on the several experiments we presented in this work, apparently, a spatially back-projected USF image usually has an improved spatial resolution. However, because of signal chaos in spatial and temporal information, this algorithm shows limited improvement about the spatial resolution (see Figure 5.13 (f)) when applied in a more scattered medium or with a larger imaging depth (e.g. centimeters). Furthermore, this algorithms usually adopts different values (such as a different threshold for signal segmentation) in various cases. As a result, currently this algorithm does not apply as a universal method that works for each experiment. Note that we adopted the algorithm based on a case-by-case analysis in each experiment in this work. Despite the limitations of the current spatial back-projection algorithm, in this work we investigated and presented that the spatial information of USF signals was very useful to improve a USF image.

5.5 Conclusion

In this study, we investigated several signal identification algorithms based on the temporal and spatial information of the USF signals. By adopting a correlation method, we improved the SNR of USF images. By adopting an ascending-slope-weighted method, we improved the spatial resolution of USF images. By using the spatial information of the USF signals, we developed a spatial back-projection algorithm and the USF imaging's spatial resolution was significantly improved based on this algorithm.

Chapter 6 *In vivo* USF imaging

6.1 Introduction

As introduced in Chapter 1, *in vivo* USF imaging in live animals is an important step in developing the USF imaging technique. The previous chapters describe the development of this technique regarding to the new USF contrast agents (Chapter 2 and Chapter 3) and the new USF imaging system (Chapter 4) as well as the new algorithms to improve USF imaging qualities (Chapter 5). All these results were demonstrated in tissue-mimic phantoms or tissue samples. In order to achieve the success of *in vivo* USF imaging, three technical issues should be addressed: 1) develop a USF contrast agent suitable for *in vivo* USF imaging; 2) study its bio-distribution and bio-stability; 3) develop an appropriate *in vivo* USF imaging system.

In Chapter 2, we developed the new generation Indocyanine green (ICG)-encapsulated poly(N-isopropylacrylamide) (PNIPAM) nanoparticles (ICG-NPs), which is potentially an appropriate USF contrast agent for *in vivo* study. ICG-NPs have excellent USF properties (i.e., NIR λ_{ex} and λ_{em}, a good I_{on}/I_{off}, an adjustable $T_{th;}$ and a narrow T_{BW}) and also a long-term stability. In addition, ICG-NPs are likely to have good bio-stability because of its long shelf life. Of course, investigations about its *in vivo* stability should be conducted. Adopting ICG-NPs, very recently, *in vivo* USF imaging has been successfully achieved in mice.[70] The experiments were carried out in the frequency domain USF imaging system.[65] The results showed the feasibility of USF imaging in live mice.

In this chapter, for the first time we demonstrated *in vivo* USF imaging in a camera-based USF imaging system. The advantages of implementing USF imaging via a camera-based USF imaging system were the improved photons collection efficiency and the exactly known scanning area, because the 2D spatial information was provided. Furthermore, in this work *in vivo* USF imaging with multiple imaging targets (i.e., spatially separate clusters of contrast agents) in the mouse's tumor via local injection were demonstrated. Also, this work demonstrated that when the USF contrast agents were designed different particle sizes (70 nm and 330 nm), they would bio-distribute to the mouse's various organs through intravenous injection. The results showed the fluorescence from some organs (spleen and liver) remained high USF properties. Consequently, *in vivo* USF imaging at various organs (spleen or liver) were successfully achieved. All USF imaging results was validated by a commercial micro-CT. In conclusion, this chapter verified the success of *in vivo* USF imaging in a camera-based USF imaging system and demonstrated its advantages.

Also, by this work, designing different particle sizes of USF contrast agents made it possible for *in vivo* USF imaging at various organs via intravenous injection. This work will push this technology forward for future applications.

6.2 Methods

6.2.1 Chemical materials

N-isopropylacrylamide (NIPAM), acrylamide (AAm), 4-4'-Azobis(4-cyanopentanoic acid) (ACA), sodium dodecyl sulfate (SDS), N,N'-methylenebisacrylamide (BIS), N-tert-butylacrylamide (TBAM), and indocyanine green (ICG) were purchased from Sigma-Aldrich (St. Louis, MO, USA). All chemicals were used without further purification.

6.2.2 USF contrast agent and CT imaging contrast agent preparation

In USF imaging, we adopted Indocyanine green (ICG)-encapsulated poly(N-isopropylacrylamide) (PNIPAM) nanoparticles (ICG-NPs, the 2nd generation) as USF contrast agents.[64] The protocols were described in Chapter 2. Three sub-types were used in the experiments: (1) ICG-NPs with its temperature threshold (T_{th}) = ~26 °C and particle size = ~ 330 nm. It is suitable for *ex vivo* USF imaging. (2) ICG-NPs with T_{th} = ~36 °C and particle size = ~ 330 nm. It is suitable for *in vivo* USF imaging in tumor via local injection. Also, it is suitable for *in vivo* USF imaging in mouse's spleen via intravenous injection. (3) ICG-NPs with T_{th} = ~39 °C and particle size = ~ 70 nm (Note that Mr. Yang Liu helped develop the synthesis protocol). It is suitable for *in vivo* USF imaging in mouse's liver via intravenously injection. The T_{th} of ICG-NPs was controlled by adjusting the quantity and ratio of N-isopropylacrylamide (NIPAM), N-tert-butylacrylamide (TBAM), and acrylamide (AAm). The particle size of ICG-NPs was controlled by adjusting the quantity of surfactant sodium dodecyl sulfate (SDS). We adopted ICG-NPs (1) and (2) in local injection experiments because it had a relatively large size (~ 330 nm) and could stay in tissue or tumor up to a few hours without a significant change in distribution. In intravenous injection, we controlled the ICG-NPs' bio-distribution to the mouse's different organs by adjusting their particle sizes: ICG-NPs (2) (T_{th} = ~36 °C, particle size = ~ 330 nm) would most accumulate in mouse's spleen; in contrast, ICG-NPs (3) (T_{th} = ~39 °C, particle size = ~ 70 nm) would most accumulate in mouse's liver and kidney. In micro-CT imaging, we adopted a commercial CT contrast agent ExiTron nano 12000. ExiTron nano 12000 could stay in tissue or tumor up to a few hours without much change in distribution when locally injected. When intravenously injected, ExiTron nano 12000 would most accumulate in mouse's spleen and liver after a few hours. In the experiments, we adopted an aqueous mixture of USF contrast agents and CT contrast agents and injected the mixture solution locally in the tumor or intravenously through the mouse's lateral tail vein. The mixture ratio and volume differed in each experiment and was described in the *Results*. By doing this, we had the same imaging target in both USF imaging and CT imaging. By 3D co-registration of a USF image and a CT image, we can compare the two modalities.

6.2.3 Animal preparation

6.2.3.1 Mouse species

The animal protocols were approved by the University of Texas at Arlington's Animal Care and Use Committee. In this study, two mouse species were adopted: 1) nude mouse (NU/J, female, Jackson Laboratory) and 2) BALB/cJ mouse (BALB/cJ, female, Jackson Laboratory).

6.2.3.2 Tumor implantation in the nude mice

The nude mice were used for USF imaging in tumors. At age of 7 weeks, they were implanted glioblastoma tumors on their left hind legs. The number of implanted tumors was one or adjacent two. The size of one tumor should have a maximum diameter < 2.0 cm; and if two tumors were implanted adjacent, their joint diameter should have a maximum < 3.5 cm.

6.2.3.3 Anesthesia preparation

During USF imaging, the mouse (NU/J or BALB/cJ) was anesthetized by isoflurane (ISOSOL ISOFLURANE, Miller Veterinary Supply, Ft. Worth, TX, USA) with a 1.8% concentration and a flow rate at 0.8 liter/min. The mouse's respiratory rate was controlled at ~ 1 breath/second under anesthesia condition. Also, the mouse's body temperature was maintained at ~ 35–36 °C by a tank of warm water at a temperature of 38 °C.

6.2.3.4 Animal preparation for USF imaging and CT imaging

At age of 11–14 weeks (body weight: 20–30 grams), the nude mice were performed 3D USF imaging and 3D CT imaging when the contrast agents were locally injected in their tumors. The BALB/cJ mice (6–8 weeks, body weight: 15–20 grams) were used for USF imaging in organs. They were removed hair and performed 3D USF and CT imaging after the contrast agents were intravenously injected through the lateral tail vein and accumulated in some organs (i.e., spleen and liver). After USF imaging, the mouse was sacrificed. Then, the dead mouse was performed 3D CT imaging in a commercial micro-CT system.

6.2.4 A camera-based *in vivo* USF imaging system

6.2.4.1 System setup

In this work, we carried out USF imaging experiments in an ICCD camera-based imaging system. The system set-up was similar to an EMCCD camera-based imaging system developed in our previous work.[69] Figure 6.1 shows schematic diagram of the system. The tissue sample (or animal subjects) was placed on a platform for imaging. The platform was fixed above a water tank. An FU transducer (its central frequency = 2.5 MHz) was submerged in the water tank and sent a FU beam into the tissue sample. The FU transducer was mounted on a motorized 3D translation stage. The sample was illuminated by a diode laser (wavelength: 785 nm; total power: 2 Watts) through a bifurcated fiber bundle. The laser was working on direct-current (DC) mode. One band-pass interference filter (F1, center wavelength: 785 nm, bandwidth: 62 nm) was adopted for excitation filtering. On the top, an ICCD camera with a lens system captured the emitted fluorescence. The camera was also working on DC mode. The camera was placed at two different height so two fields of view (FOVs) were available for imaging: FOV 1 and FOV 2. FOV 1 had a size of 6.5 cm in diameter, which was relatively large and appropriate for imaging the mouse's whole body in bio-distribution study. FOV 2 had a size of 2.6 cm in diameter, which was appropriate for USF imaging. In FOV 1, four long-pass interference filters (F3-F6, blocking band: 830 nm) were placed in front of the lens for emission filtering. In FOV 2, in total five long-pass interference filters (blocking band: 830 nm) were placed behind (F2) or in front of (F3-F6) the lens for emission filtering. A pulse delay generator (PDG 1) followed by a function generator (FG) was triggered by the camera via its internal trigger (i.e., the image trigger) and used to generate an ultrasound driving signal (i.e. a 2.5 MHz sinusoidal wave). The signal was further amplified by a radiofrequency power amplifier (RF AMP, 50 dB amplification) and delivered to the FU transducer (with a matching network, MNW) to generate an ultrasonic wave. A second pulse delay generator (PDG 2) was triggered by PDG 1 and sent a pulse to the translation stage for FU scanning. It is worth mentioning here that, the location of the FU focus on x-y plane (i.e., its x, y position) could be detected, by acquiring a USF signal from a single silicone tube under the camera.

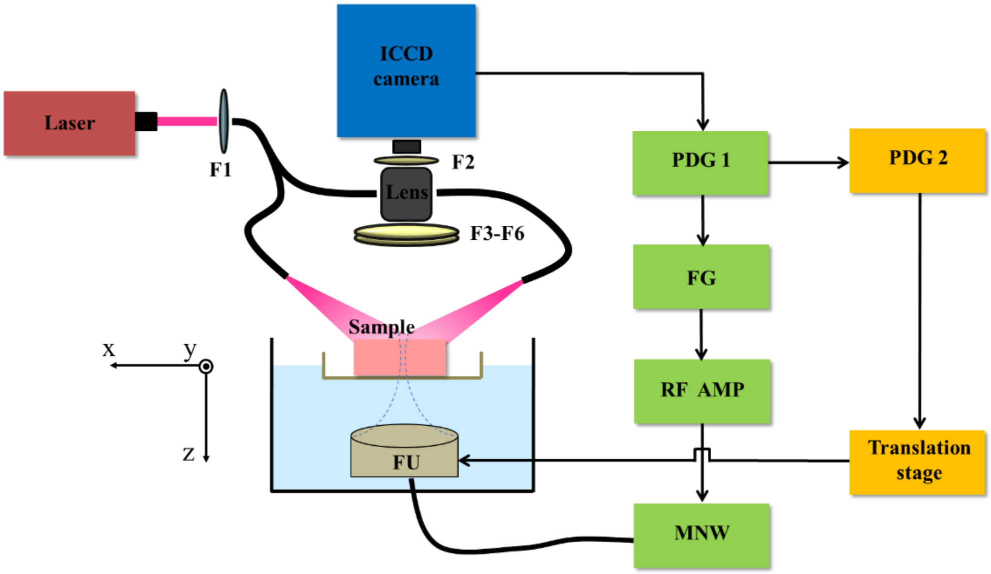

Figure 6.1 Schematic diagram of the ICCD camera-based USF imaging system. Note that Mr. Tingfeng Yao helped during the development of this system.

6.2.4.2 USF signal acquisition, identification, and 3D USF imaging

Figure 6.2 shows the time sequence diagram of acquiring a USF signal (in FOV 2). In the first row, it shows that the camera acquired two images. The time interval between two images was 5.0 s (i.e., the camera trigger rate = 0.2 Hz). The camera exposure time (yellow region) was 1.0 s with a readout time of 0.5 s (green region). The first image (acquired at t = 1.5s) was considered as background since it was acquired before an FU was sent. In the second row, an ultrasound driving signal was generated and sent to the FU transducer with a delay of 4.6 s from the start. The duration of the FU signal was 0.4 s, so it ended right before the start of acquiring the second image. Thus, the second image (acquired at t = 6.5 s) was a fluorescence image after a FU signal was sent to the sample, and was considered as an image of background plus a USF signal. The first image was then subtracted from the second and the remainder was considered as an image of the USF signal only. The USF photons in the subtracted image were collected and summed within a selected region of interest (ROI) based on the location of FU focus, and the summation was counted as the USF signal intensity. Typically, the selected ROI was a circled region with its center at the FU focus and its diameter is 10 mm. In the third row, another trigger was sent to the translation stage after 7.0 s from the start. It was used to move the FU transducer to the next scan point. After 30.0 s from the start, the camera repetitively followed the same time sequence to acquire the USF signal at the next point. By raster scanning of the FU transducer and acquiring USF signals at each scan point, a 3D USF image was acquired based on a point to point scanning method. The 3D USF image was normalized and interpolated.

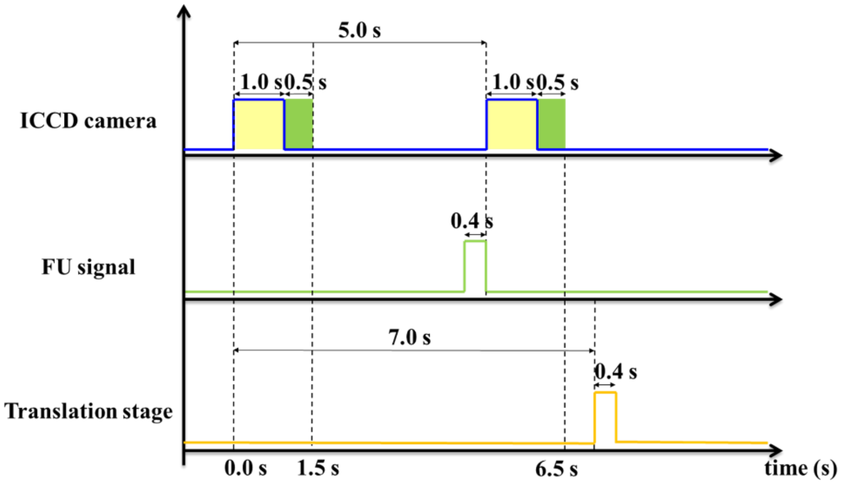

Figure 6.2 Time sequence diagram of acquiring a USF signal.

6.2.5 An X-ray micro-CT imaging system

The 3D CT image was acquired in the commercial micro-CT system (Skyscan high-speed X-ray *in vivo* micro-CT, Bruker, Billerica, MA). The images were reconstructed and processed via the software provided by the manufacturer of the system (NRecon and CTAn). The 3D CT image was presented in maximum intensity projection mode.

6.2.6 3D co-registration

In this section, there are two main tasks. The first one is to quantify the distribution of USF contrast and CT contrast from their agents. The second one is to co-register their distributions. In this study, we directly adopted the USF signal strength to represent the concentration of USF contrast agents. To quantify the distribution volume, the 3D USF image was segmented via a 2D Otsu method.[69,70,88] Briefly, we selected one representative slice of the 3D USF image on x-y plane and applied the 2D Otsu method. Thus, the threshold that differentiates the object from the background was found. By segmenting the whole 3D USF image with the threshold value, the USF contrast distribution was obtained. Similarly, the CT contrast distribution volume was quantified by the same method. In 3D co-registration, by co-localizing spatial coordinates, the 3D scan region in USF imaging was marked in the CT image so that the same region of CT data was extracted. Briefly, the initial x, y position of FU focus could be localized via acquiring a USF signal in a silicone tube. The real size that each pixel represents was calibrated by image a ruler. Thus, the x, y positions of the USF image scanning points were determined. By comparing the fluorescence image and the x-y planar intersections of the CT image, the x and y positions of the USF scan region and the corresponding CT region were co-localized. Their z positions were co-localized by using an ultrasound pulse-echo method to detect top and bottom surface of the imaging subject in USF imaging and comparing it to that in CT imaging. By co-localization, we then co-registered the 3D USF image and the 3D CT image in the software provided by micro-CT system (DataViewer). To realize a better co-registration, the angle and location of the two objects were slightly adjusted manually.

6.3 Results

6.3.1 Bio-distribution of the USF contrast agents in mice

6.3.1.1 Bio-distribution of ICG-NPs in the nude mice via subcutaneous injection

As a preliminary study, we conducted the experiments of ICG-NPs' bio-distribution in nude mice (NU/J, female) in a commercial fluorescence imaging system: IVIS Spectrum system (Caliper, Xenogen, Alameda, CA) at Department of Radiology, UT Southwestern Medical Center. This study includes two experiments: the first is to study the bio-distribution of ICG-NP when subcutaneously injected in the mice; the second is that when intravenously injected in the mice. In subcutaneous injection, two types of ICG-NPs were adopted: ICG-NPs (1) with T_{th} = ~26 °C and particle size = ~ 330 nm, and ICG-NPs (2) with T_{th} = ~36 °C and particle size = ~ 330 nm. In intravenous injection, one type of ICG-NPs was adopted: ICG-NPs (2) with T_{th} = ~36 °C and particle size = ~ 330 nm. The excitation filter was at 745 nm. The emission filter was at 820 nm. Figure 6.3 shows the bio-distribution of ICG-NPs over 48 hours when subcutaneously injected on the mice's dorsal side. The nude mouse on the left was injected 100 uL ICG-NPs (1), and the nude mouse on the right was injected 100 uL ICG-NPs (2). The fluorescence intensity in the figure was normalized. The displaying threshold of fluorescence = 0.15. The results show that when subcutaneously injected, both the ICG-NPs stayed nearby the injection spots and did not distributed fast to overall body for up to 48 hours. Also, the fluorescence intensity did not decrease fast over 48 hours.

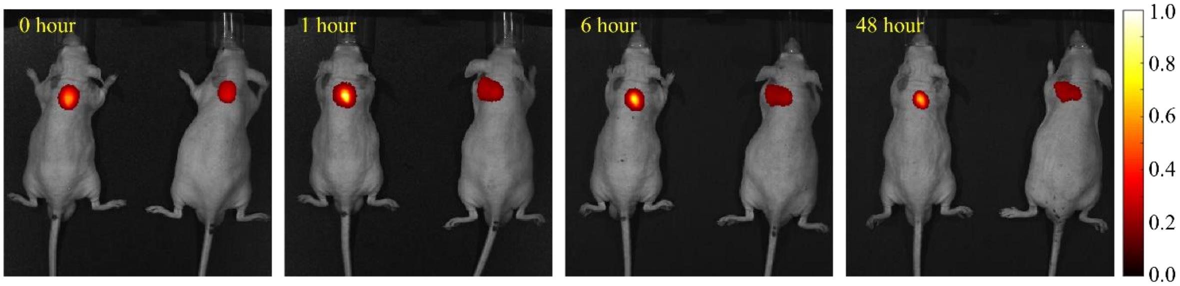

Figure 6.3 Biodistribution of ICG-NPs (1) (left) and ICG-NPs (2) (right) in the nude mice (NU/J, female) when subcutaneously injected.

Figure 6.4 shows the bio-distribution of ICG-NPs (2, T_{th} = ~26 °C, particle size = ~ 330 nm) when intravenously injected through the mice's lateral tail vein. Two mice were adopted in this experiment. Both mice were injected 100 µL ICG-NPs (2). The first image in Figure 6.4 shows the fluorescence in both mice accumulated on the mice's left side 6 hours after injection. One mouse (i.e., the left one in the first image) was kept alive and taken another fluorescence image after 24 hours after injection. The second image shows the corresponding results. The fluorescence in this mouse still accumulated in the same area. The fluorescence intensity is normalized in the two images and the fluorescence displaying threshold = 0.40. The other mouse (i.e., the right one in the first image) was sacrificed after taken fluorescence image at 6 hours. The third image in Figure 6.4 shows the normalized fluorescence image of *ex vivo* organs (i.e., liver, kidney, stomach, intestine, and spleen) of this mouse. The fluorescence displaying threshold is also 0.40. It shows the fluorescence mainly came from the spleen.

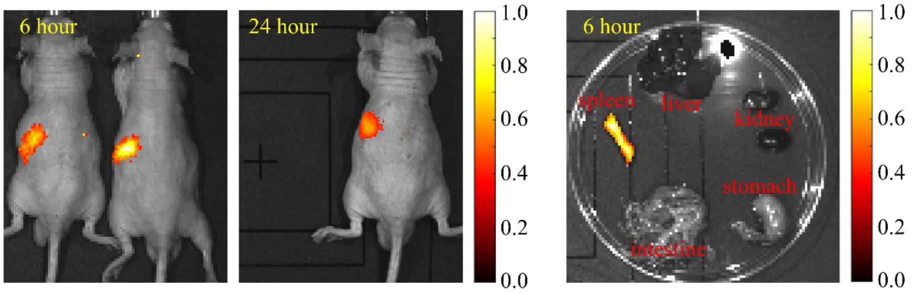

Figure 6.4 Biodistribution of ICG-NPs (2, T_{th} = ~26 °C, particle size = ~ 330 nm) in the nude mice (NU/J, female) when intravenously injected. It shows the fluorescence mainly accumulated in the spleen organ 6 hours after injection.

We conclude from this preliminary study that: 1) when subcutaneously injected, the ICG-NPs (i.e., either ICG-NP (1) or (2)) are likely to stay accumulated for a relatively long time (> 48 hours); 2) when intravenously injected, the ICG-NPs (T_{th} = ~26 °C, particle size = ~ 330 nm) are likely to accumulated the spleen organ of the mouse.

6.3.1.2 Bio-distribution of ICG-NPs in BALB/cJ mice via intravenous injection

In this section, we studied the bio-distribution of two USF contrast agents: ICG-NPs (2), whose T_{th} = ~36 °C, particle size = ~ 330 nm; and ICG-NPs (3), whose T_{th} = ~ 39 °C, particle size = ~ 70 nm. We adopted BALB/cJ mice (female, 6–8 weeks) as the imaging subjects. The mice were removed hair and intravenously injected the contrast agents via lateral tail vein. They were then placed under the ICCD camera system (Figure 6.1) for *in vivo* 2D planar fluorescence imaging in FOV 1. After that, we investigated that whether the fluorescence distributed in organs still had some USF properties. Thus, some mice was sacrificed after *in vivo* fluorescence imaging and their organs were conducted *ex vivo* fluorescence imaging. Figure 6.5 shows the biodistribution of ICG-NPs (2) (T_{th} = ~36 °C, particle size = ~ 330 nm). First, one mouse was intravenously-injected 100 uL ICG-NPs (2) and conducted *in vivo* fluorescence imaging over 24 hours. In Figure 6.5 (a), it shows the normalized fluorescence distribution on the left side of the mouse's body after injection. Other positions of the mouse were also recorded (i.e., dorsal, ventral, and right side; not shown). It is found that the fluorescence accumulated most on its left side after 3 hours. This area was nearby where the mouse's spleen was located. To verify whether the fluorescence mainly came from the spleen, another mouse was conducted intravenous injection and *in vivo* imaging with the same procedure but sacrificed 3 hours after injection. Figure 6.5 (b) shows the corresponding results. The *in vivo* results (i.e., the first three images) show the fluorescence also accumulated on the mouse's left side body. The last image shows a fluorescence image of the *ex vivo* organs taken from the sacrificed mouse. It shows the fluorescence most accumulated in spleen, and partially went to liver, kidney, stomach as well as intestine. After that, to investigate whether the strong fluorescence in spleen still had USF properties (i.e., the fluorescence intensity would change as a function of temperature), we studied the relationship between the spleen sample's fluorescence intensity and its environment temperature. The spleen was placed in a mortar filled with warm water and then was conducted *ex vivo* fluorescence imaging at different temperatures in the same FOV. Figure 6.5 (c) shows the spleen's fluorescence intensity change when the water temperature cooled down (temperature = ~ 50 °C, 43 °C, 34 °C, 28 °C, and 25 °C. The first image in Figure 6.5 (c) is a white photo of the sample. The results show that the fluorescence intensity was a few times higher when the temperature was higher than the ICG-NPs' T_{th} (= ~ 36 °C), compared to that when the temperature was lower than its T_{th}. Its intensity on-to-off ratio (i.e., $I_{T=50\ °C} / I_{T=25\ °C}$) = ~ 2.3 folds. The results indicate that the fluorescence intensity in spleen changed with temperature and the fluorescence intensity remained thermal-switchable properties.

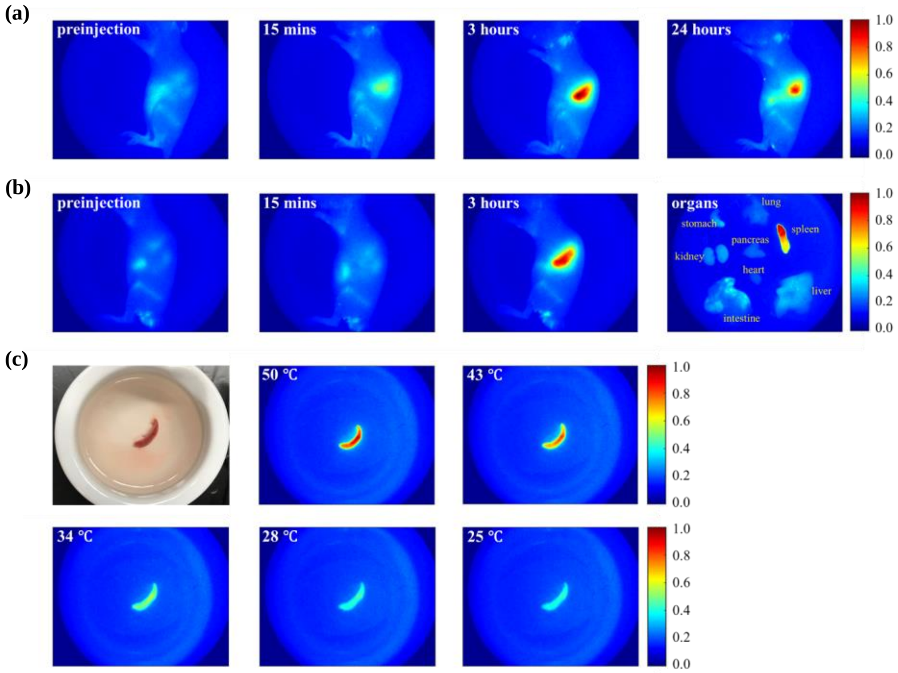

Figure 6.5 (a) Normalized fluorescence intensity variation on the left side of one mouse over 24 hours after it was intravenously injected 100 μL ICG-NPs with its T_{th} = ~36 ℃ and particle size = ~ 330 nm. (b) Normalized fluorescence intensity variation on the left side of a second mouse over 3 hours (the first three images) after it was intravenously injected the same ICG-NPs solution, as well as the normalized fluorescence from the mouse's organs (the last image) after the mouse was sacrificed at 3 hours. (c) The first image is a white photo of the second mouse's spleen sample. The next five images show its normalized fluorescence intensity change as a function of temperature.

In comparison, Figure 6.6 shows the biodistribution of ICG-NPs (3) (T_{th} = ~ 39 °C, particle size = ~ 70 nm) in mice. Similarly, a first mouse was intravenously-injected 150 uL ICG-NPs (3) and conducted *in vivo* fluorescence imaging over 24 hours. Figure 6.6 (a1) shows the normalized fluorescence distribution of the mouse's dorsal side, and Figure 6.6 (a2) shows that of the mouse's ventral side. Other positions (i.e., left side and right side, not shown in the figure) were recorded as well. It was likely that the fluorescence most accumulated in area of kidney and liver after 3 hours. To validate this, a second mouse was conducted the same procedure except that sacrificed 3 hours after injection. Figure 6.6 (b1)–(b3) show its *in vivo* biodistribution (Figure 6.6 (b1) represents dorsal side; Figure 6.6 (b2) represents ventral side) and its *ex vivo* organs (Figure 6.6 (b3)) after sacrifice. The results validate that the fluorescence was most accumulated in kidney and liver. Figure 6.6 (c1) and (c2) shows the liver's and kidney's fluorescence intensity change at different temperatures (50 °C, 43 °C, 34 °C, 28 °C, and 25 °C) in the water bath, respectively. In the liver, the fluorescence intensity on-to-off ratio (i.e., $I_{T=50\ °C}$ / $I_{T=25\ °C}$) = ~ 2.1 folds. In kidney, the fluorescence intensity on-to-off ratio (i.e., $I_{T=50\ °C}$ / $I_{T=25\ °C}$) = ~ 1.1 folds. The results demonstrate that the fluorescence in liver still had a good thermal-switchable property so it is appropriate for USF imaging. In contrast, the fluorescence intensity on-to-off ratio in the kidney was low so that kidney was less likely a good USF imaging target.

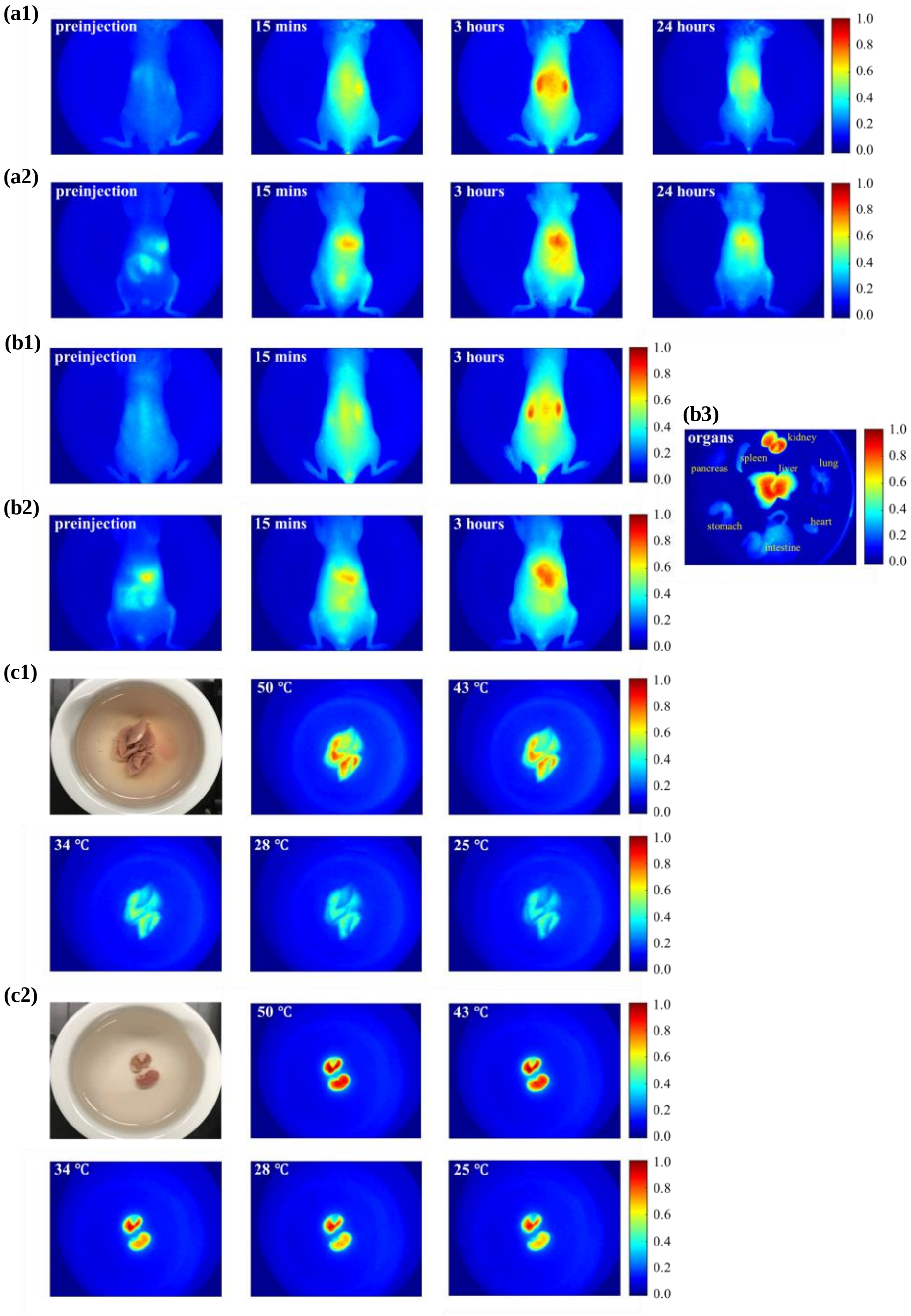

Figure 6.6 (a) 24 hours bio-distribution of one mouse after it was intravenously injected 150 μL ICG-NPs with its T_{th} = ~39 ℃ and particle size = ~ 70 nm. (a1) Normalized fluorescence intensity variation on the dorsal side of the mouse over 24 hours. (a2) Normalized fluorescence intensity variation on the ventral side of the mouse over 24 hours. (b) 3 hours bio-distribution of a second mouse after it was intravenously injected the same ICG-NPs solution. (b1) Normalized fluorescence intensity variation on the dorsal side of the mouse over 3 hours. (b2) Normalized fluorescence intensity variation on the ventral side of the mouse over 3 hours. (b3) Normalized fluorescence from the mouse's organs after sacrifice at 3 hours. (c) The fluorescence intensity change from the second mouse's liver and kidney as a function of temperature. (c1) The first image is a white photo of the liver sample. The next five images show its normalized fluorescence intensity change as a function of temperature. (c2) The first image is a white photo of the kidney sample. The next five images show its normalized fluorescence intensity change as a function of temperature.

In short conclusion, the first ICG-NPs (ICG-NPs (2), T_{th} = ~36 °C, particle size = ~ 330 nm) most accumulated in spleen when intravenously injected. Its fluorescence showed a good temperature-switchable property (> 2.0 folds) so that spleen is an appropriate USF imaging target. The second ICG-NPs (ICG-NPs (3), T_{th} = ~39 °C, particle size = ~ 70 nm) most accumulated in liver and kidney when intravenously injected. There was a good thermal-switchable fluorescence in liver (> 2.0 folds) while not in kidney (< 2.0 folds). Thus, liver is also an appropriate target in USF imaging.

6.3.2 *Ex vivo* USF imaging in a porcine heart tissue phantom via a local injection

In order to test the ICCD camera-based USF imaging system, we first adopted a porcine heart tissue as the imaging subject and conducted an *ex vivo* USF imaging experiment. The thickness of the tissue was ~ 10 mm. An aqueous mixture of USF contrast agents (ICG-NPs, T_{th} = ~ 26°C, particle size = ~ 330 nm) and CT contrast agents (ExiTron nano 12000) was locally injected from the center of its top surface. The mixture's total volume was 20 uL, with a volume ratio ICG-NPs/ExiTron nano 12000 = 3/1. Figure 6.7 (a) displays the normalized fluorescence intensity distribution on the tissue's top surface in FOV 2, with a fluorescence displaying threshold = 0.25. Its top left shows a white-light photo of the tissue sample. The red solid square in Figure 6.7 (a) represents the FU scanning region on x-y plane. The total scan volume was 10.16 (x) × 12.192 (y) × 6.096 (z) mm^3. The lateral step size (of both x and y direction) was 1.016 mm and the axial step size (of z direction) was 2.032 mm, respectively. Figure 6.7 (b) represents the top view of the 3D CT image of the tissue phantom. The red dash square highlights the CT contrast agents' distribution in the tissue. Figure 6.7 (c) shows an example of the acquired USF signal from the porcine heart tissue sample (also in FOV2). The FU driving voltage was voltage peak-to-peak (Vpp) = 160 mV. The FU location was x = –0.743 mm, y = +0.392 mm, z = +3.048 mm (marked as a black cross in the first image; the spatial coordinates were not shown in the images). The first image (t = 1.5 s) represents the background fluorescence image (of the tissue top surface) before a FU signal was sent. The second image (t = 6.5 s) represents the fluorescence image right after a FU signal was sent to the sample. The third image equals to the first subtracted from the second, which shows increased fluorescence photons. They were considered the USF photons emitted and scattered to tissue top surface. As described in the *Methods* section, mathematically, the summation of the USF photons in the third image with a selected ROI was counted as the USF signal at this FU scan point. By scanning the FU transducer and repetitively acquiring the USF signals, a 3D USF image was formed. Figure 6.7 (d) shows the normalized USF image on x-y planes at different z.

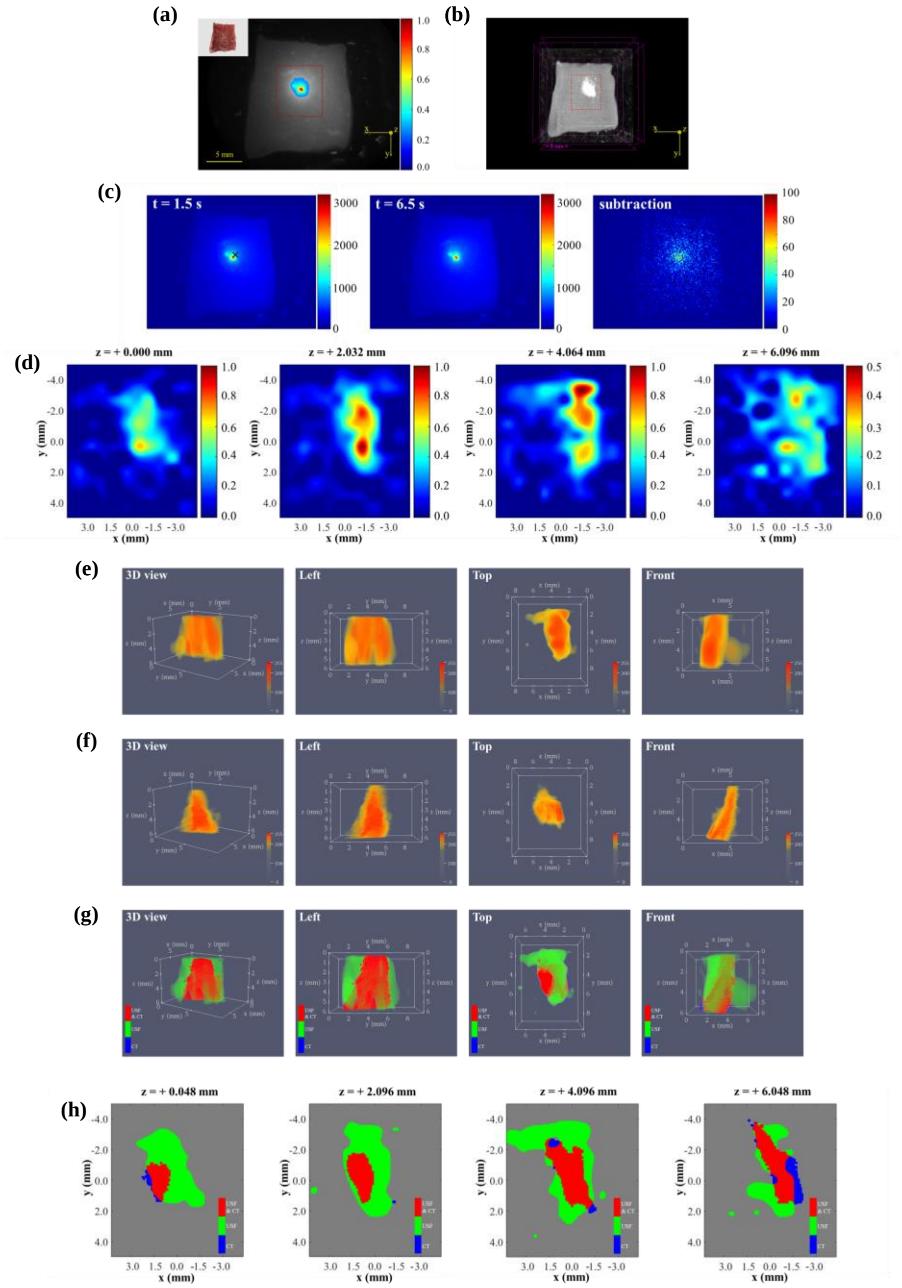

Figure 6.7 (a) Normalized 2D planar fluorescence image of the porcine heart tissue in FOV 2. (b) Top view of the 3D CT image of the porcine heart tissue. (c) An example of acquired USF signals from the porcine heart tissue. (d) Acquired USF images on x-y plane at different z locations. The data was normalized and interpolated. (e) The USF image of the USF contrast volume from 3D view, left side view, top view, and front view. (f) The CT image of the CT contrast volume from 3D view, left side view, top view, and front view. (g) 3D co-registration results of the USF and CT image. The green volume represents the USF contrast only. The blue volume represents the CT contrast agents only. The red volume represents their overlapped area. (h) The co-registration results on x-y plane at different z locations. Note that Mr. Tingfeng Yao developed the imaging processing and registration software, which was used in this dissertation.

After acquiring both the USF image and CT image, we processed the data for 3D co-registration. Figure 6.7 (e) represents the normalized (value range: 0 to 255) USF contrast volume in 3D view, left (YZ) view, top (XY) view and front (XZ) view. A transparency displaying threshold (= 93 here, same as its USF signal segmentation threshold) was applied to remove the background (same principle below). Correspondingly, Figure 6.7 (f) represents the normalized CT contrast volume (value range: 0 to 255), which was extracted from the overall CT image (see Figure 6.7 (b)) and has the same spatial coordinates as the USF image. A transparency displaying threshold = 163 (same as its CT contrast segmentation threshold) was applied here. Figure 6.7 (g) represents their 3D co-registration. The green volume represents the distribution of the USF contrast only, which is = 64.467 mm^3; the blue volume represents the distribution of the CT contrast only, which is = 3.285 mm^3; and the red volume represents their overlapped area, which is = 44.153 mm^3. Figure 6.7 (h) shows the 2D x-y planar cross-sections of the co-registered volumes at different z. The results indicate that two modalities provided a similar distribution of contrast agents.

6.3.3 *In vivo* USF imaging in mouse's tumor via local injection

6.3.3.1 *In vivo* USF imaging in a glioblastoma tumor on a mouse via one local injection

In this section, we adopted a nude mouse as the imaging subject. It was implanted a glioblastoma tumor (tumor size: ~ 1.5 cm at its maximum diameter) on its right hind leg. An aqueous mixture of USF contrast agents (ICG-NPs, T_{th} = ~ 36°C, particle size = ~ 330 nm) and CT contrast agents (ExiTron nano 12000) was locally-injected in the tumor, with a total volume = 50 uL and a volume ratio ICG-NPs/ExiTron nano 12000 = 3/1. The mouse was performed *in vivo* 3D USF imaging and then 3D CT imaging. Figure 6.8 (a) shows the normalized 2D fluorescence planar image of the mouse in FOV 1. At top left it shows a corresponding white photo of the mouse (photo was taken after sacrifice). The yellow dash square in Figure 6.8 (a) represents FOV 2 of the camera. Figure 6.8 (b) represents the normalized 2D fluorescence planar image in FOV 2, which highlights the fluorescence distribution in the tumor area. In both Figure 6.8 (a) and (b), the fluorescence was displayed at a threshold > 0.25. In Figure 6.8 (b), the red solid square represents the USF scanning area on x-y plane. The 3D USF scanning volume was 11.176 (x) × 12.192 (y) × 6.096 (z) mm^3. The lateral step size (of both x and y direction) was 1.016 mm and the axial step size (of z direction) was 2.032 mm. Figure 6.8 (c) represents the top view of the CT image of the mouse. The red dash square highlights the distribution of CT contrast agents in the tumor area. Figure 6.8 (d) represents a single USF signal acquired at a location of FU focus: x = + 1.015 mm, y = + 1.542 mm, z = 0.000 mm (marked as a black cross in the first image; the coordinates were not shown in the images). The FU driving voltage was Vpp = 220 mV. Similarly, the first image (t = 1.5 s) represents the background fluorescence image; the second image (t = 6.5 s) represents the fluorescence image after a FU signal was sent to the tumor; the third image was obtained by subtracting the first from the second. It clearly shows a USF signal in form of a 2D scattering spot emitted on the tumor's top surface. Its location was close to the FU focus on x-y plane. Then, by scanning the FU transducer and acquiring USF signals at different x, y, z, a 3D USF image was obtained. Figure 6.8 (e) shows the USF image on x-y planes at different z.

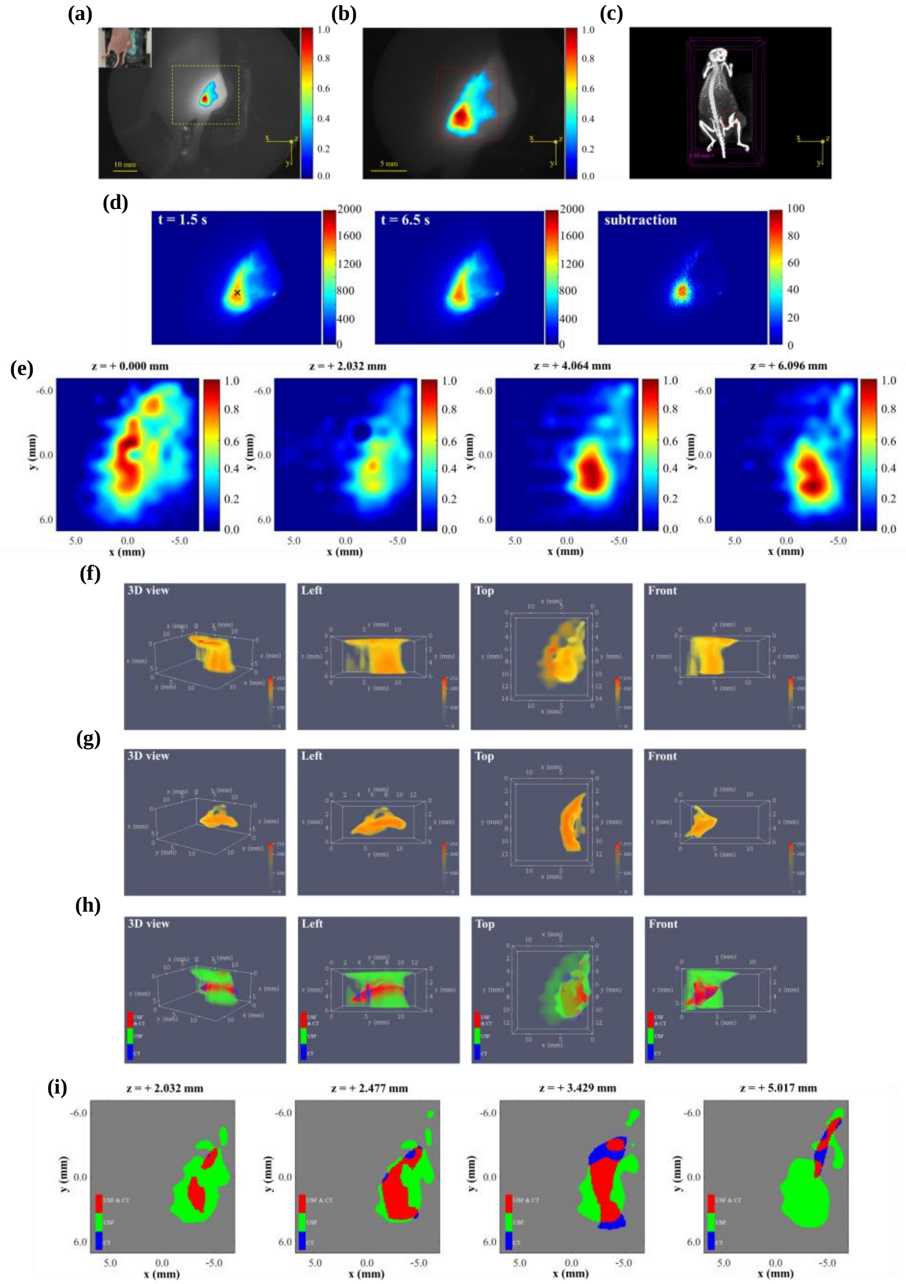

Figure 6.8 (a) Normalized 2D planar fluorescence image of the mouse in FOV 1. The yellow dash square highlights the fluorescence from the tumor. (b) Zoomed-in normalized 2D planar fluorescence image of the mouse's tumor area in FOV 2, which corresponds to the yellow dash square in (a). (c) Top view of the 3D CT image of the mouse's dorsal side. The red dash square highlights the distribution of the CT contrast agents in the tumor. (d) An example of acquired USF signals from the tumor. (e) Acquired USF images on x-y plane at different z locations. The data was normalized and interpolated. (f) The USF image of the USF contrast volume from 3D view, left side view, top view, and front view. (g) The CT image of the CT contrast volume from 3D view, left side view, top view, and front view. (h) 3D co-registration results of the USF and CT image. The green volume represents the USF contrast only. The blue volume represents the CT contrast agents only. The red volume represents their overlapped area. (i) The co-registration results on x-y plane at different z locations.

Following the same co-registration principle, the 3D USF contrast volume, the 3D CT contrast volume and their co-registered volume were represented. Figure 6.8 (f) shows 3D view, left (YZ) view, top (XY) view and front (XZ) view of the normalized (value range: 0 to 255) USF contrast volume. A transparency threshold (= 120) was applied to remove the background. Correspondingly, Figure 6.8 (g) shows 3D view, left (YZ) view, top (XY) view and front (XZ) view of the normalized (value range: 0 to 255) CT contrast volume within the same spatial coordinate. A displaying threshold (= 129) was applied to remove its background. Figure 6.8 (h) represents their co-registration results. The green volume represents the distribution of the USF contrast only, which is = 170.052 mm^3; the blue volume represents the distribution of the CT contrast only, which is = 11.085 mm^3; and the red volume represents their overlapped area, which is = 37.857 mm^3. Figure 6.8 (i) represents 2D x-y planar cross-sections of the co-registered volumes at different z. The results indicate that *in vivo* USF imaging was successful in tumor and the two modalities provided a similar distribution of contrast agents.

6.3.3.2 *In vivo* USF imaging in two adjacent glioblastoma tumors on a mouse via two separate local injections

In the previous section, we carried out *in vivo* USF imaging in the nude mouse's tumor where the contrast agents mainly distributed as a cluster in one location (see Figure 6.8 (a)–(c)) via one local injection. In this section, we demonstrated *in vivo* USF imaging of two separate clusters of contrast agents distributed in two adjacent tumors on a nude mouse, via two separate local injections in each tumor. The nude mouse was implanted two glioblastoma tumors adjacently on its right hind leg. The size of two tumors was ~ 3.4 cm at its maximum diameter. Each tumor had a maximum diameter < 2.0 cm. An aqueous mixture of USF contrast agents (ICG-NPs, T_{th} = ~ 36°C, particle size = ~ 330 nm) and CT contrast agents (ExiTron nano 12000) was locally injected in each tumor. The mixture volume ratio was ICG-NPs/ExiTron nano 12000 = 3/1. Each injection volume was 50 uL. The distance between two injection spots was ~ 1.5 cm. Figure 6.9 (a) shows the normalized 2D fluorescence planar image of the mouse in FOV 1. The mouse was placed on its back. The fluorescence was displayed > a threshold = 0.5. Its top left shows a white photo of the mouse (photo was taken after sacrifice). The yellow dash square represents FOV 2 of the camera. Figure 6.9 (b) shows the normalized 2D fluorescence planar image in FOV 2, highlighting the tumor area. The fluorescence was displayed > a threshold = 0.25. As shown, there were two spots (i.e., the upper location and the lower location) that showed fluorescence because of two local injections. The red solid square represents the USF scanning area on x-y plane. The 3D scanning volume was 13.716 (x) × 24.384 (y) × 10.668 (z) mm^3. The lateral step size (of both x and y direction) was 1.524 mm and the axial step size (of z direction) was 3.556 mm. Figure 6.9 (c) shows the CT image of the mouse in top view. The CT contrast in the two tumors were highlighted in the red dash square in the figure. Figure

4 (d1) and (d2) represent an example of single USF signals acquired in each tumor. The FU driving voltage was fixed at Vpp = 220 mV. Figure 6.9 (d1) represents a USF signal acquired at the upper location of the scanned area (i.e., nearby the first local injection). The position of FU focus was located at x = +1.905 mm, y = –9.144 mm, z = 0.000 mm (marked as a black cross in the first image in (d1)). Figure 6.9 (d2) represents a USF signal acquired at the lower location of the scanned area (i.e., nearby the second local injection). The position of FU focus was located at x = + 0.762 mm, y = + 6.096 mm, z = 0.000 mm (marked as a black cross in the first image in (d2)). In both Figure 6.9 (d1) and (d2), the first image represents the background fluorescence image, the second image represents the fluorescence image right after a FU signal was sent, and the third represents a subtraction of the first from the second which shows acquired USF signals from tumors' top surface. Comparing Figure 6.9 (d1) and (d2), it clearly shows that the USF signal, in either case, only occurred nearby where a FU signal was sent. That is, when a FU signal was sent to nearby the first local injection spot (i.e., the upper location), the USF signal only showed up nearby the upper location; likewise, when a FU signal was sent to nearby the second injection spot (i.e., the lower location), the USF signal only showed up nearby the lower location. Both USF signals were in form of 2D scattering fluorescence spots. It is worth mentioning that their scattering sizes were different, which depended on the depths (i.e., the distance from the location of switched-on contrast agents to tumor top surface) and also the tumor tissue's scattering coefficients. Figure 6.9 (d1) and (d2) exclude the possibility that the acquired signal might mainly come from fluorescence variation (noise). By 3D scanning, a 3D USF image was acquired. Figure 6.9 (e) shows the USF image on x-y planes at different z. It clearly shows that there were two separate clusters of USF signals at the upper and lower locations.

By image processing and 3D co-registration, we acquired 3D USF contrast volume, 3D CT contrast volume and their co-registration results. Figure 6.9 (f) shows 3D view, left (YZ) view, top (XY) view and front (XZ) view of the normalized (value range: 0 to 255) USF contrast volume. A displaying threshold (= 78) was applied to remove the background. Figure 6.9 (g) shows 3D view, left (YZ) view, top (XY) view and front (XZ) view of the normalized (value range: 0 to 255) CT contrast volume with a displaying threshold = 74. Figure 6.9 (h) shows their 3D co-registration results. The USF-only volume (green) has a size = 1125.697 mm^3; the CT-only volume (blue) has a size = 24.842 mm^3; and their overlapped volume (red) has a size = 116.639 mm^3. Figure 6.9 (i) shows the co-registration results on x-y planes at different z. The results shows that in both USF and CT image, there were two separate imaged objects, which should represent the two clusters of both contrast agents. Thus, in this experiment, *in vivo* USF imaging was successfully achieved with two separate imaging targets. Also, the results show that two modalities provided a similar distribution of contrast agents.

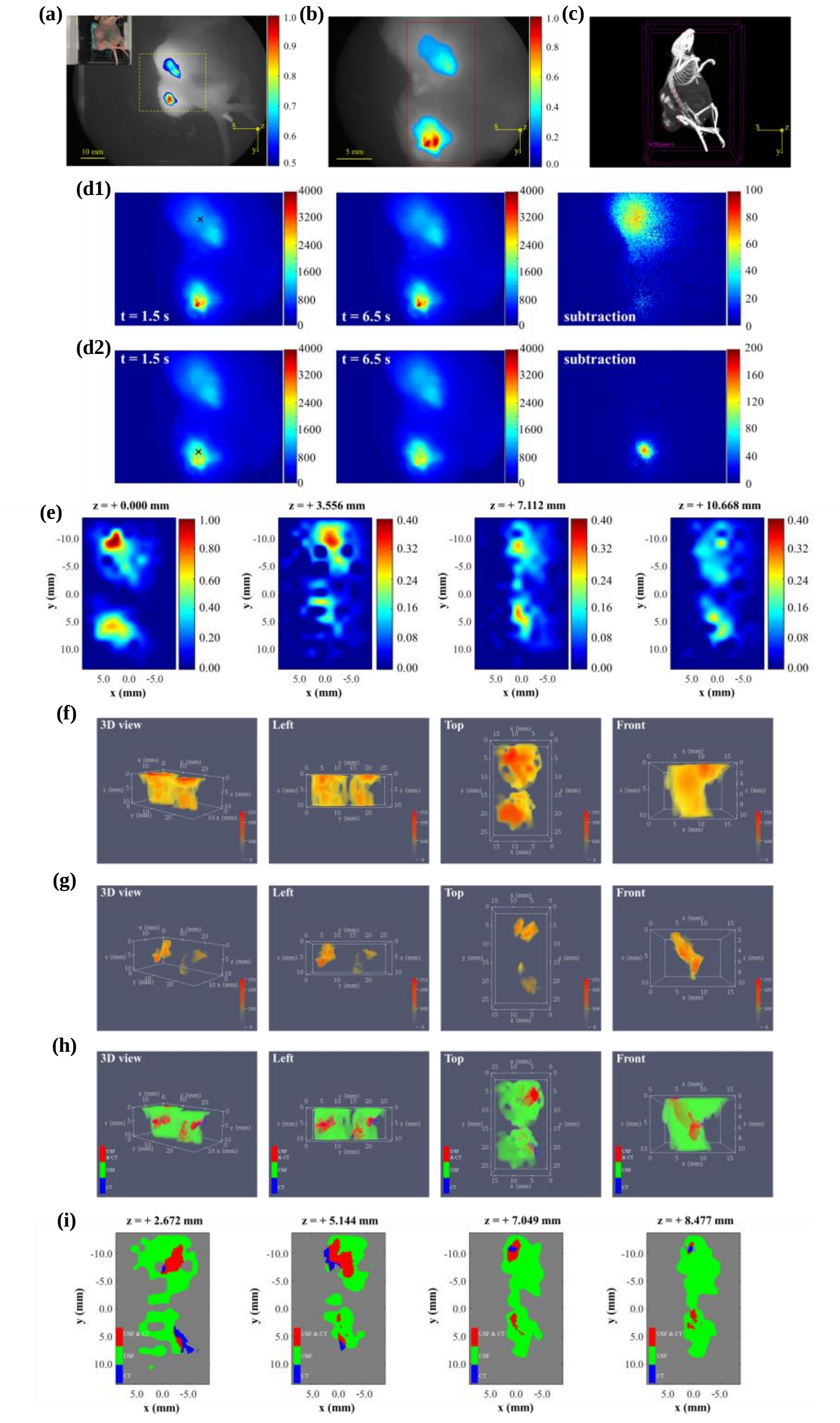

Figure 6.8 (a) Normalized 2D planar fluorescence image of the mouse in FOV 1. (b) Zoomed-in normalized 2D planar fluorescence image of the mouse's tumor area in FOV 2. (c) Top view of the 3D CT image of the mouse's ventral side. (d) Examples of acquired USF signals from each tumor. (d1) represents the USF signal acquired from the first tumor at the upper location. (d2) represents the USF signal acquired from the second tumor at the lower location. (e) Acquired USF images on x-y plane at different z locations. (f) The USF image of the USF contrast volume from 3D view, left side view, top view, and front view. (g) The CT image of the CT contrast volume from 3D view, left side view, top view, and front view. (h) 3D co-registration results of the USF and CT image. (i) The co-registration results on x-y plane at different z locations.

6.3.4 *In vivo* USF imaging of mice's organs via intravenous injection

In the previous section 6.3.1.2, we demonstrated that, when intravenously injected, the ICG-NPs would bio-distribute to spleen (ICG-NPs, T_{th} = ~36 °C, particle size = ~ 330 nm) or liver (ICG-NPs, T_{th} = ~39 °C, particle size = ~ 70 nm). Also, the fluorescence in these two organs still remain good temperature-switchable properties. Thus, the organs are appropriate USF imaging targets. In the next two sections, *in vivo* USF imaging of the mice's spleen and liver would be demonstrated.

6.3.4.1 *In vivo* USF imaging of a mouse's spleen

In this section, we adopted a BALB/cJ (female) mouse as the imaging subject. The mouse was intravenously-injected an aqueous mixture of USF contrast agents (ICG-NPs, T_{th} = ~36 °C, particle size = ~ 330 nm) and CT contrast agents (ExiTron nano 12000) through lateral tail vein. Note that the ICG-NPs have a large particle size here. The mixture solution volume ratio was ICG-NPs/ExiTron nano 12000 = 5/1, and its total volume = 120 μL. As shown previously, the ICG-NPs' fluorescence most accumulated in spleen and it had a good thermal-switchable property. Meanwhile, it is known that the CT contrast agents would partially accumulate in the mouse's spleen. Thus, the mouse's spleen was an appropriate imaging target for both USF and CT imaging. Figure 6.9 (a) shows the normalized 2D planar fluorescence image (in FOV 1) of the mouse's left side 3 hours after injection. The fluorescence displaying threshold is 0.25. Its top left is a white photo of the mouse (photo was taken after sacrifice). Again, it shows the fluorescence mainly accumulated in the spleen area. The yellow dash square in Figure 6.9 (a) represents FOV 2 of the camera. Figure 6.9 (b) shows the normalized 2D planar fluorescence image in FOV 2, with the same displaying threshold = 0.25. The red solid square represents the USF scanning area on x-y plane. The USF scanning volume was 13.208 (x) × 12.192 (y) × 6.096 (z) mm^3, with a lateral step size = 1.016 mm and an axial step size = 2.032 mm. Figure 6.9 (c) shows the CT image of the mouse from its top view after USF imaging (~ 9 hours). The red dash square highlights the spleen area. Figure 6.9 (d) shows a single USF signal acquired nearby the spleen, at a FU focus location x = –0.469 mm, y = +1.000 mm, z = 0.000 mm (marked as a black cross in the first image; the coordinates were not shown in the images). In the third image, it shows a USF signal was acquired in form of a scattering fluorescence spot nearby the FU focus on x-y plane. The FU driving voltage was fixed at Vpp = 200 mV. By scanning the FU transducer, a 3D USF image was acquired. Figure 6.9 (e) shows the normalized USF image on x-y planes at different z.

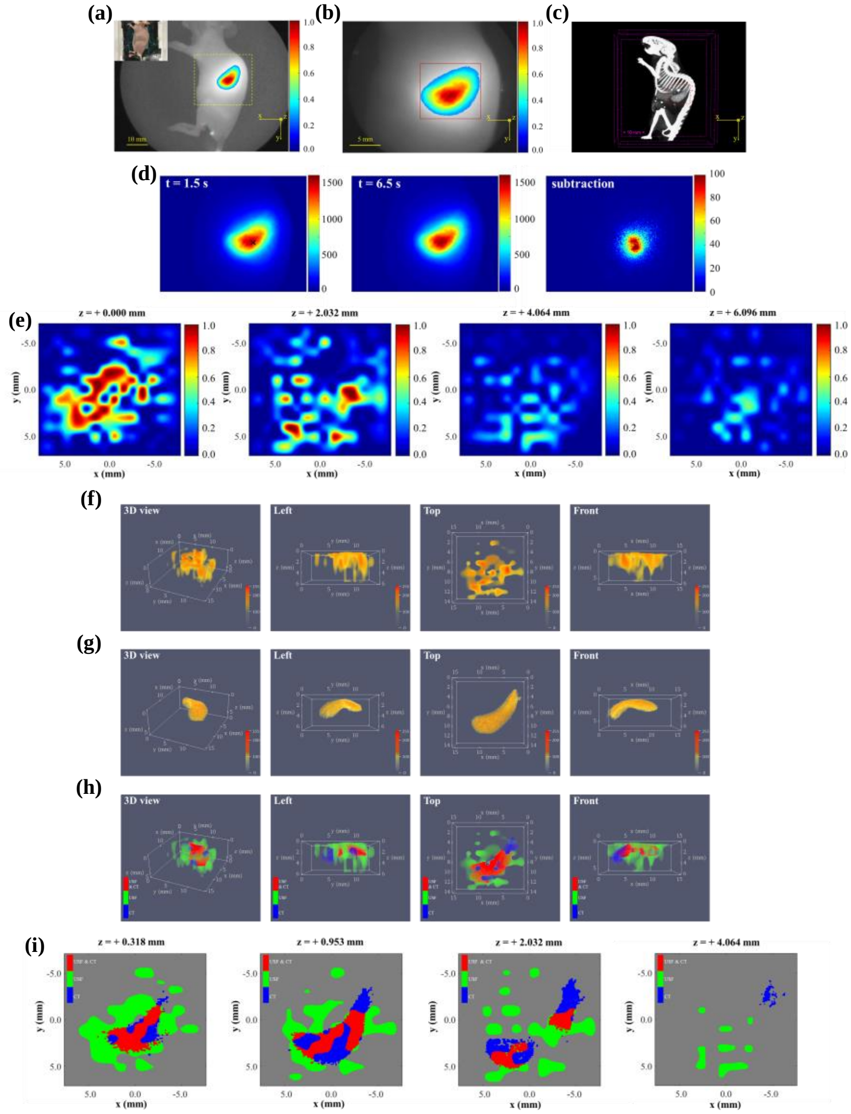

Figure 6.9 (a) Normalized 2D planar fluorescence image of the mouse on its left side in FOV 1. The fluorescence mainly accumulated in the mouse's spleen. (b) Zoomed-in normalized 2D planar fluorescence image of the mouse's spleen area in FOV 2. (c) Top view of the 3D CT image of the mouse's left side. (d) An example of acquired USF signals from the spleen area of the mouse. (e) Acquired USF images on x-y plane at different z locations. (f) The USF image of the USF contrast volume from 3D view, left side view, top view, and front view. (g) The CT image of the CT contrast volume from 3D view, left side view, top view, and front view. (h) 3D co-registration results of the USF and CT image. (i) The co-registration results on x-y plane at different z locations.

Similarly, after acquiring both the USF and CT images, we processed the data and co-registered the images. Figure 6.9 (f) shows the 3D, left (YZ), top (XY), front (XZ) view of the USF contrast volume (value range: 0 to 255). Its segmentation and displaying threshold is 95. Figure 6.9 (g) shows the corresponding CT contrast volume (value range: 0 to 255) of the spleen, with a segmentation and displaying threshold = 99. Figure 6.9 (h) shows their 3D co-registration results. The USF-only volume (green) is 107.307 mm^3. The CT-only volume (blue) is 43.680 mm^3. The overlapped volume (red) is 29.991 mm^3. Figure 6.9 (i) represents the co-registration results on x-y planes at different z. The results indicate *in vivo* USF imaging of the mouse's spleen was successfully achieved.

6.3.4.2 *In vivo* USF imaging of a mouse's liver

In this section, we also adopted a BALB/cJ (female) mouse as the imaging subject. Again, we intravenously-injected an aqueous mixture of USF contrast agents (ICG-NPs, T_{th} = ~39 °C, particle size = ~ 70 nm) and CT contrast agents (ExiTron nano 12000; volume ratio: ICG-NPs/ExiTron nano 12000 = 5/1; total volume = 180 μL) through the mouse's lateral tail vein. Note that the ICG-NPs have a small particle size here. As known, the ICG-NPs and ExiTron nano 12000 accumulated in the mouse's liver area. Also, it was validated that the fluorescence in the liver still had a good I_{on}/I_{off} ratio. Thus in this experiment, we adopted the mouse's liver as the imaging target for both USF and CT imaging. Figure 6.10 (a) shows the normalized 2D planar fluorescence image in FOV1 of the mouse's ventral side 3 hours after intravenous injection. The mouse was placed on its back (i.e., displaying its ventral side). The figure's top left is a white photo correspondingly (photo was taken after sacrifice). It shows the fluorescence mainly accumulated around the liver area. The yellow dash square represents FOV 2. Figure 6.10 (b) shows the normalized 2D planar fluorescence image in FOV 2 of the mouse's liver area. Both Figure 6.10 (a) and (b) have a fluorescence displaying threshold = 0.75. The red solid square in Figure 6.10 (b) represents the USF scanning area on x-y plane. The 3D USF scanning volume was 15.24 (x) × 12.192 (y) × 4.064 (z) mm^3, with a lateral step size = 1.016 mm and an axial step size = 2.032 mm. Figure 6.10 (c) is the CT image of the mouse from top view after USF imaging (~ 9 hours). It shows the mouse's liver has a relative high contrast (highlighted by a red dash square), because ExiTron nano 12000 accumulated in the mouse's liver. Figure 6.10 (d) shows a single USF signal acquired in the liver, at a FU focus location x = –2.545 mm, y = + 0.048 mm, z = + 2.032 mm (marked as a black cross in the first image). In the last image, it clearly shows increased fluorescence in the liver area after a FU signal was sent. The FU driving voltage was fixed at Vpp = 200 mV. By 3D scanning, a 3D USF image was acquired. Figure 6.10 (e) shows the normalized and interpolated USF image on x-y planes at different z.

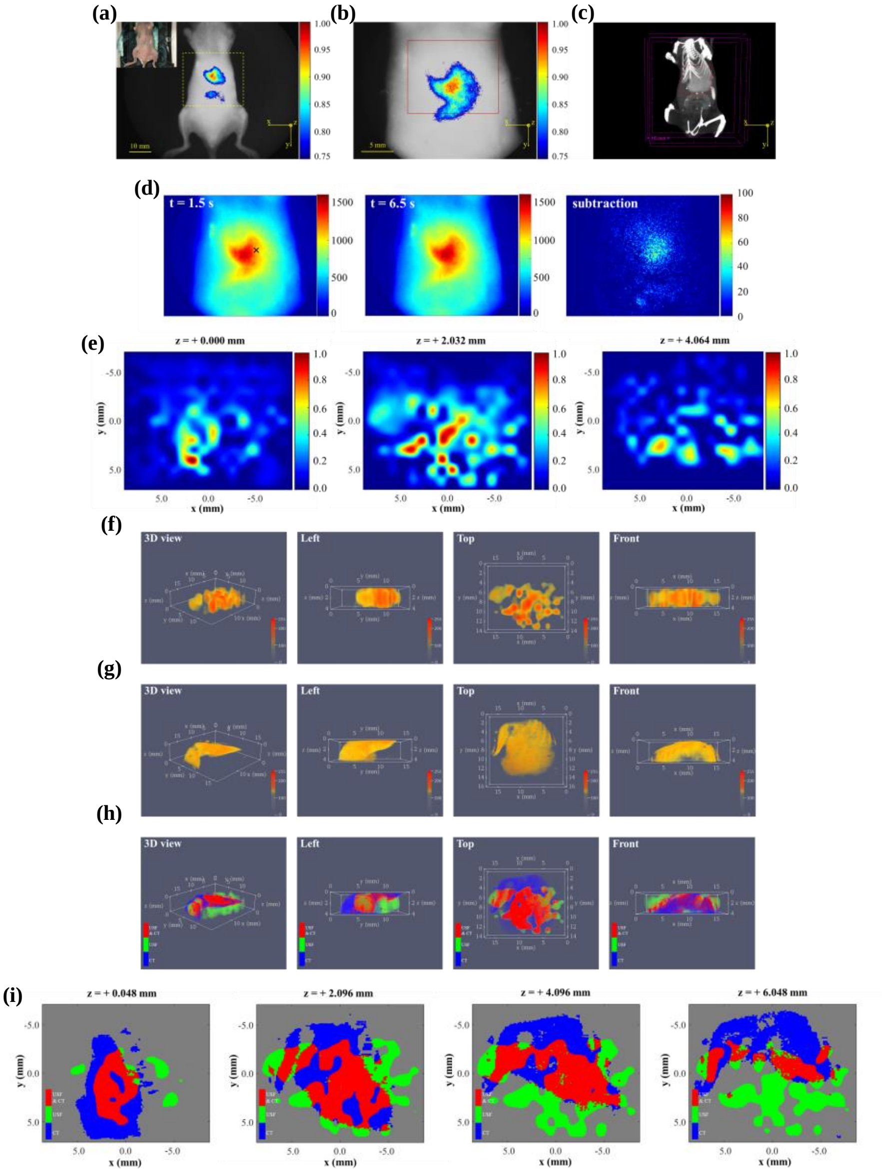

Figure 6.10 (a) Normalized 2D planar fluorescence image of the mouse on its ventral side in FOV 1. The fluorescence mainly accumulated in the mouse's liver. (b) Zoomed-in normalized 2D planar fluorescence image of the mouse's liver area in FOV 2. (c) Top view of the 3D CT image of the mouse's ventral side. (d) An example of acquired USF signals from the liver area of the mouse. (e) Acquired USF images on x-y plane at different z locations. (f) The USF image of the USF contrast volume from 3D view, left side view, top view, and front view. (g) The CT image of the CT contrast volume from 3D view, left side view, top view, and front view. (h) 3D co-registration results of the USF and CT image. (i) The co-registration results on x-y plane at different z locations.

Figure 6.10 (f) shows the normalized 3D, left (YZ), top (XY), and front (XZ) view of the USF contrast volume (value range: 0 to 255), which highlights the USF contrast from the liver area. Its segmentation and displaying threshold is 82. Correspondingly, in the same spatial coordinate, Figure 6.10 (g) shows the 3D, left (YZ), top (XY), and front (XZ) view of the CT contrast volume, which highlights the CT contrast in the mouse's liver. Its segmentation and displaying threshold is 120. Figure 6.10 (h) shows their co-registration results. The USF-only volume (green) is 125.594 mm^3. The CT-only volume (blue) is 157.272 mm^3. The overlapped volume (red) is 128.871 mm^3.

Correspondingly, Figure 6.10 (i) represents their co-registration on x-y planes at different z. The results indicate *in vivo* USF imaging of the mouse's liver was successful.

6.3.5 *In vivo* USF imaging in a mouse's leg via intramuscular injection

In this section, we carried out in vivo USF imaging in a mouse's leg via intramuscular injection. We adopted a BALB/cJ (female) mouse as the imaging subject. An aqueous mixture of USF contrast agents (ICG-NPs, T_{th} = ~ 36°C, particle size = ~ 330 nm) and CT contrast agents (ExiTron nano 12000) was intramuscularly-injected in the left hind leg of the mouse, with a total volume = 20 uL and a volume ratio ICG-NPs/ExiTron nano 12000 = 3/1. Figure 6.11 (a1)–(a3) show an example of acquiring a USF signal from the mouse's leg. Similar to the previous, (a1) represents the background fluorescence image, (a2) represents the fluorescence image after a FU signal was sent to one scan point of the target area on the leg (not shown), and (a3) is the image of subtracting (a1) from (a2) and represents the USF signal. The summation of the USF photons in a selected ROI was counted as the USF signal intensity. Figure 6.11 (b) shows the micro-CT image of the mouse's leg. The red dash square represents the USF scanning area on x-y plane. The total scan area is 9.144(x) × 8.128(y) × 3.048(z) mm^3. The CT contrast agents are highlighted in this area (shown as the white contrast except the bones). Figure 6.11 (c) shows the 2D background fluorescence image. The yellow dash square corresponds the same USF scanning area on x-y plane. Figure 6.11 (d) shows one of the normalized 2D USF image slices (z = + 1.016 mm). Figure 6.11 (e) shows the 3D CT-contrast distribution of ExiTron nano 12000 (shown in red). Its calculated volume is 37.46 mm^3. Figure 6.11 (f) shows the 3D USF-contrast distribution of ICG-NPs in the same volume (shown in green). Its calculated volume is 94.65 mm^3. Figure 6.11 (g) shows the 3D spatial co-registration of the two. The blue body represents the overlapped volume, which is 26.18 mm^3. By co-registration, Figure 6.11 (e)-(g) show that the micro-CT and the USF image have similar distribution. Also, it shows USF-contrast volume is larger than the CT-contrast volume.

6.4 Discussion

6.4.1 Selecting an appropriate particle size of USF contrast agents

Selecting an appropriate particle size of ICG-NPs is also very important especially in *in vivo* USF imaging of the mouse's organs. This study shows that when ICG-NPs have a large size (~ 330 nm), the particles were more likely to accumulate in spleen. In opposite, when ICG-NPs have a small size (~ 70 nm), they had a high chance to accumulate in liver and kidney. Of course, in either scenario, some fluorescence showed up in other organs as well. This is probably because 1) there were always both small and large particles in each solution although the proportions were significantly different, and the particle size here only represented their median value; 2) some ICG-NPs might be metabolized into small fragments (i.e., ICG-polymers) or even free fluorophores when bio-distributed to some organs.

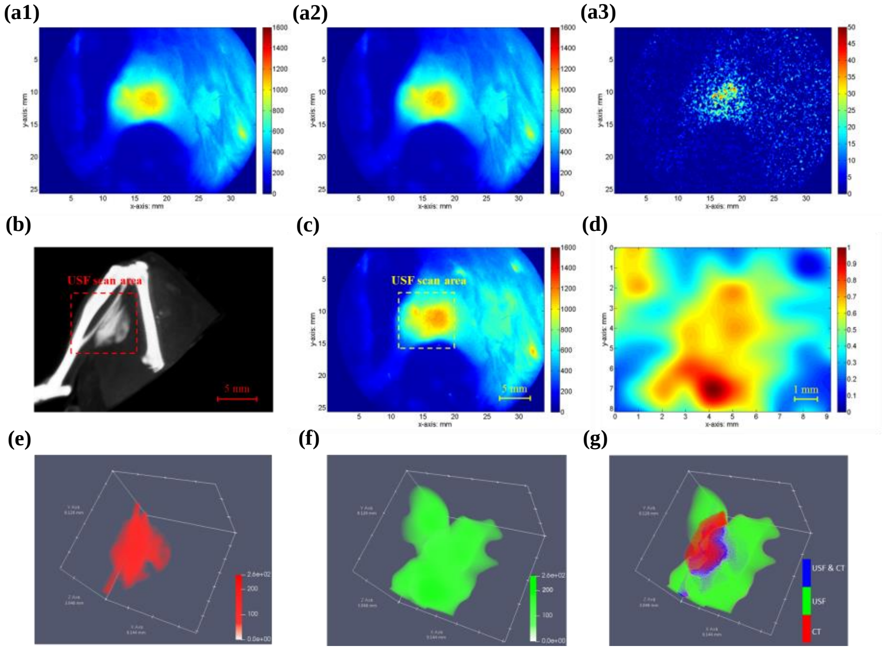

Figure 6.11 (a1)–(a3) Acquiring a USF signal from the mouse's leg; (a1) background fluorescence image; (a2) fluorescence image after a FU signal was sent to one scan point of the target area on the leg (not shown); (a3) image of subtracting (a1) from (a2). (b) Micro-CT image of the mouse's leg. The red dash square represents the USF scanning area on x-y plane. The total scan area is 9.144(x) × 8.128(y) × 3.048(z) mm^3. (c) 2D background fluorescence image. The yellow dash square corresponds the same USF scanning area on x-y plane. (d) One of the normalized 2D USF image slices acquired at z = + 1.016 mm. (e) 3D CT-contrast distribution of ExiTron nano 12000 (shown in red). (f) 3D USF-contrast distribution of ICG-NPs in the same volume (shown in green). (g) 3D spatial co-registration of CT-contrast and USF-contrast. The blue body represents the overlapped volume.

6.4.2 An appropriate time scale of bio-distribution

In this work, the contrast agents (i.e., ICG-NPs and ExiTron nano 12000) were injected by two pathways: local injection in tumor and intravenous injection through mouse's lateral tail vein. First, when the ICG-NPs (T_{th} = ~36 °C, particle size = ~ 330 nm) and ExiTron nano 12000 were locally injected in tumor, they were likely to stay in the tumor's intercellular space without a significant move for a few hours. This was proven by the 3D micro-CT image and 2D planar fluorescence image before and after the USF imaging (not shown in the *Results*). Second, the bio-distribution study of ICG-NPs showed that it could stay in spleen (i.e., ICG-NPs with a large particle size = ~ 330 nm) or in liver (i.e., ICG-NPs with a small particle size= ~ 70 nm) up to 24 hours without significant losses of fluorescence. Also, the CT contrast agents (ExiTron nano 12000) could stay in spleen and liver up to 9 hours after intravenous injection, until the 3D USF imaging were finished. It is worth pointing out that the slow change of bio-distribution made it possible to carry out 3D USF and CT imaging and process their co-registration without much variation in the contour of the imaging target. Therefore, the co-registration results were reliable and USF imaging were validated by CT imaging.

6.4.3 Bio-stability of USF contrast agents in tumors and organs

The bio-stability of USF contrast agents played a vital role in the success of USF imaging in live animals. From the perspective of acquiring a USF signal successfully, the contrast agents *in vivo* should remain two key USF properties: (1) the USF contrast agents should remain the same T_{th}; (2) the USF contrast agents should remain a high fluorescence intensity on-to-off ratio (i.e., a high I_{on}/I_{off}). ICG-NPs is an excellent USF contrast agents with a long shelf life[64] and a high stability in biological environments and thus adopted in this study. In this work, the ICG-NPs were injected by two pathways: local injection in tumor and intravenous injection through mouse's lateral tail vein. When the agents were locally injected in mouse's tumor, it is relatively easy to assume that ICG-NPs remained its USF properties since it mainly clustered in tumor's intercellular space and had less chance of interaction with the biological environments. The USF imaging results in tumor also validate this assumption. In our previous work, we also validated this assumption from the fact that it is difficult to acquire a USF signal from a dead mouse's tumor when T_B (~ 23.5 °C) was much lower than the T_{th} (~ 36 °C) because of lack of FU heating efficiency. In contrast, when ICG-NPs were intravenously injected, it was much more likely that the agents were partially or fully metabolized in mice's organs. Thus, it requires extra attention to verify whether the organs' fluorescence remain USF properties. In this work, based on the bio-distribution study, we verified that the ICG fluorescence from spleen has a T_{th} between 34 °C and 43 °C, and an I_{on}/I_{off} = ~ 2.3 folds (see Figure 6.5 (c)); that from liver has a T_{th} between 34 °C and 43 °C, and an I_{on}/I_{off} = ~ 2.1 folds (see Figure 6.6 (c1)); and that from kidney has a T_{th} between 34 °C and 43 °C, and an I_{on}/I_{off} = ~ 1.1 folds (see Figure 6.6 (c2)). As a result, the spleen and liver were more appropriate for USF imaging since their fluorescence remained an appropriate T_{th} and also a good I_{on}/I_{off} (> 2.0 folds). Meanwhile, it comes to our attention that the fluorescence in kidney had a low on-to-off ratio (< 2.0 folds). The possible mechanism is that the kidney usually took up small particles (e.g., < 10 nm) in biodistribution[89] so that most of small ICG-polymer fragments or free ICG fluorophores accumulated in the kidney. As a result, the fluorescence from kidney might lose most of thermal-switchable properties.

6.4.4 An appropriate temperature-switching threshold of USF contrast agents

In our previous work, we have demonstrated that the temperature threshold (T_{th}) of USF contrast agents should be a few degrees higher than the background temperature (T_{BG}), either *ex vivo* or *in vivo*, in order to most efficiently acquire the USF signal. In this work, we adopted ICG-NPs as contrast agents. In USF imaging of the porcine heart tissue phantom (i.e., an *ex vivo* scenario), the T_{th} of ICG-NPs was selected at 26 °C when the T_B was the room temperature (= ~ 23.5 °C). In *in vivo* USF imaging, the T_{th} of ICG-NPs was selected at ~ 36 – 39 °C, when T_B was equal to the mice body temperature (= ~ 35–36 °C, under anesthesia condition).

6.4.5 Advantages of a camera-based USF imaging system for *in vivo* study

Compared with the previous USF imaging system[57,58,65,67,68], which mainly used a photomultiplier (PMT) as the detector, there are several advantages of adopting a camera-based system for *in vivo* study. First, the ICCD camera is NIR-enhanced and it has a high sensitivity in detecting NIR USF photons. Also, the camera's intensifier was on DC mode so that it had the highest detection sensitivity for weak *in vivo* USF signals. Second, the camera captured the USF signal in a 2D space (x-y plane), with a relatively large FOV. Due to that the USF photons mainly came from centimeter deep tissue and was in form of a scattering spot (whose size was usually up to a few centimeters in diameter), the camera could help collect most of the USF photons from the top surface of tissue or animal. In a word, the camera provides a high detection efficiency. What's more important, the 2D scattering spot clearly represented the source of the USF signal and its location was shown in the camera's FOV. Since the location of the FU signal was known, it was easy to determine whether the acquired signal was FU-correlated. For example, in USF imaging of the contrast agent distribution in two adjacent glioblastoma tumors on a mouse via two separate local injections (see *Results* section), when a FU signal was sent to the first tumor at the upper location, the 2D scattered USF signal only showed up at the upper tumor's top surface (Figure 6.8 (d1)). When another FU signal was sent to the second tumor at the lower location, the 2D scattered USF signal only showed up at the lower tumor's top surface (Figure 6.8 (d2)). Thus, the increased fluorescence in the subtraction image (see the third image in Figure 6.8 (d1) or (d2)) was highly correlated to the location of the FU signal and thus was not likely caused by fluorescence fluctuation (noise). This analysis is very unique in a camera-based USF imaging system. Third, the camera captured the USF signal by accumulatively collecting photons within a long exposure time (= 1 second) and helped reduce the noise caused by the animals' breath. Especially, in USF imaging of the spleen or liver, the live mice had a strong breathing motion and caused fluorescence fluctuation in organs. This fluctuation would significantly add noise to the acquired USF signal. In our previous work, we removed this noise by fitting the USF signal and correlating it with a reference signal. In this work, instead, the camera accumulated all the USF photons in a long exposure time and got rid of this fluctuation by signal-averaging. Note that the mice's breathing rate was controlled at ~ 1 breath/second (as described in *Methods* section) and the camera exposure time was selected at 1 second too, so that the fluorescence fluctuation caused by the mouse's breath could be mostly averaged and removed.

6.4.6 Spatial resolution of both *ex vivo* and *in vivo* USF images

The spatial resolution of a USF image is determined by the size of thermal focal volume generated by FU signal. In this work, it was mainly determined by the FU power (or its driving voltage) and the biological tissue's ultrasound absorption coefficients. Briefly, with the increase of FU power, the spatial resolution of a USF image would be worse, but the signal-to-noise ratio (SNR) of the image would be better, due to a larger size of thermal focal volume. There were three types of biological tissues adopted for USF imaging in this study: dead porcine heart tissue, live mice's tumor, and live mice's organs (spleen and liver). Basically, the FU driving voltage for dead porcine heart tissue was 160 mV Vpp, for a live mouse's tumor was 220 mV Vpp, for a live mouse's spleen was 200 mV, and for a live mouse's liver was also 200 mV. The reason for adopting a higher Vpp for tumor and organs is that living tissue usually has a lower ultrasound absorption coefficient because of the fluids and blood flows. Another reason for using a highest Vpp in tumor is that its imaging depth (up to 1 cm) was bigger than that in organs (spleen and liver were located relatively close to the skin). Thus, the USF signal from the tumor was weaker so that a higher FU power could help increase the SNR.

6.4.7 Limitations

As seen in this work, the SNR of USF images were relatively low especially in the organ's *in vivo* USF imaging. This is due to the weak signal and the strong background noise. Although ICG-NPs have been approved that it has excellent USF properties such as an adjustable T_{th}, a good I_{on}/I_{off}, and a high bio-stability, as well as an adjustable particle size, it is desirable to develop more contrast agents with a higher quantum efficiency in NIR region (i.e., a higher I_{on}) for a better SNR. Another limitation is the motion artifacts caused by the animal's breath in USF imaging, especially when the imaging targets were the mice's organs. Solutions should be developed to minimize the effect of animal motion.

6.5 Conclusion

In this work, we successfully carried out *in vivo* 3D USF imaging in live mice via a camera-based USF imaging system. *In vivo* USF imaging in the mouse's glioblastoma tumor with one or multiple targets were demonstrated. Also, *in vivo* USF imaging of the mouse's spleen and liver were achieved. The results were validated by 3D co-registration with the micro-CT images. This work showed feasibility of *in vivo* USF imaging. The ICG-NP showed bio-stability in mouse's tumor as well as some organs (spleen and liver) and was proven a suitable USF contrast agent for *in vivo* USF imaging. Also, the camera-based USF imaging system demonstrated several advantages for *in vivo* USF imaging. This work will push USF imaging technique to many biomedical applications in the future.

Chapter 7 Conclusion and future work

7.1 Conclusions

In this dissertation, first, we successfully developed (a) new generation ICG-encapsulated poly(N-isopropylacrylamide) nanoparticles (ICG-NPs), and (b) ADP- or ZnPc-encapsulated pluronic nanocapsules. We demonstrated their excellent USF properties (i.e., NIR spectrum, a high I_{on}/I_{off}, a high τ_{on}/τ_{off}, an adjustable T_{th}, and a narrow T_{BW}) as well as long-term stability, bio-stability, and functionalization; second, we successfully developed an ICCD camera-based time-domain USF imaging system and several signal identification algorithms to improve USF imaging qualities (i.e., a higher SNR and spatial resolution). Also, we studied the tradeoffs inherent in USF imaging qualities (i.e., SNR, spatial resolution, and temporal resolution); third, we successfully carried out *in vivo* USF imaging in mice, such as tumors via local injection, muscle of the leg via local injection, and also organs (spleen and liver) via intravenous injection. The accomplished work was presented in Chapter 2–6.

In Chapter 2, two new protocols of ICG-NPs were developed for USF contrast agents with long-term stability, adjustable LCST, and functionalization. The shelf life of these new generation ICG-NPs is much longer (>6 months) than that of the first generation (<1 month). Meanwhile, this new generation ICG-NP was conjugated with functional groups (hydroxyl or carboxyl). It can be used for molecular imaging in the future if attached with a targeting moiety. Furthermore, we investigated the effect of the temperature-switching threshold (T_{th}) of the agent and the background temperature (T_{BG}) on USF imaging. Maintaining the agents' temperature threshold slightly above the background temperature is necessary for conducting USF imaging successfully and efficiently. Therefore, for *in vivo* USF imaging, the temperature threshold of the contrast agents should be controlled slightly above the body temperature, i.e. >37°C.

In Chapter 3, we successfully synthesized, characterized, and selected a series of NIR nanocapsules, by encapsulating two series of NIR fluorophores (ADP and ZnPc) in four pluronic polymers (F127, F98, F68, and F38). These nanocapsules showed excellent temperature-switchable properties of fluorescence intensity and/or lifetime. At the same time, we investigated that some factors (i.e., pluronic categories and nanocapsules' concentration) affected the nanocapsules' T_{th}s while other (i.e., fluorophore categories) did not. The pluronics' T_{th} sequence is F127 < F98 < F68 < F38 based on using different pluronics. And, a lower nanocapsule concentration brings a higher T_{th}. By selecting appropriate pluronic categories and adjusting the nanocapsule's concentration, we can synthesize the nanocapsules with a wide range of T_{th}s. We discussed that these temperature-switchable fluorescence nanocapsules can be used for USF imaging and temperature sensing.

In Chapter 4, we successfully developed an ICCD camera-based, time-domain USF imaging system. By implementing USF experiments on this system, first, we demonstrated its features and advantages for USF imaging. That is, the ICCD camera-based, time-domain USF imaging system is capable of reducing the background noise from a short lifetime pulse (such as laser leakage and autofluorescence) when the USF signal has a long lifetime. Second, we also described the tradeoffs between SNR, spatial resolution, and temporal resolution inherent in USF imaging and suggested appropriate USF imaging strategies. By changing experimental parameters: CCD camera recording time, FU power, imaging depth, and gate delay of ICCD camera, we could balance the tradeoffs. Details are shown in Table 4.3. Also, we discussed that selecting an appropriate USF contrast agent is important for a desired USF image.

In Chapter 5, we investigated several signal identification algorithms to improve USF imaging qualities based on studies in Chapter 4. We described that the USF signal acquired in the ICCD camera was as a function of recording time and also as a function of 2D spatial scattering spot. Using the temporal information of a recorded USF signal, we improved the SNR of USF images by a correlation method. Furthermore, we characterized the shape of the normalized USF signal's temporal information in three parameters: (1) the ascending slope; (2) the descending slope; and (3) the full-width-at-half-maximum (FWHM). By adopting an ascending-slope-weighted method, we improved the spatial resolution of USF images. Meanwhile, using the spatial information (i.e., 2D spatial scattering spot of a detected USF signal), we developed a completely new algorithm to plot a USF image: spatial back projection of USF scattering spots. By adopting this method, the spatial resolution was significantly improved, especially in a less scattered medium or a relatively thin tissue (a few millimeters, depending on $\mu_{s'}$). We investigated all these algorithms in one dimensional (1D) and 2D USF imaging with several imaging phantoms. The results validated the feasibility of these algorithms.

In Chapter 6, we successfully carried out *in vivo* 3D USF imaging in live mice via an ICCD camera-based *in vivo* USF imaging system. We demonstrated successful *in vivo* USF imaging in the mouse's glioblastoma tumor with one or multiple targets. Also, we achieved *in vivo* USF imaging of the mouse's spleen and liver. The results were validated by 3D co-registration with the micro-CT images. This work showed feasibility of *in vivo* USF imaging. The USF contrast agent ICG-NP (2nd generation) showed bio-stability in mouse's tumor as well as some organs (spleen and liver) and was proven a suitable agent for *in vivo* USF imaging. Also, we discussed several advantages about the ICCD camera-based *in vivo* USF imaging system for *in vivo* USF imaging.

7.2 Limitations and future directions

7.2.1 USF contrast agents

7.2.1.1 Bio-stability

In Chapter 2, we discussed about the advantages of ICG-NP as a USF contrast agent. It has an excellent bio-stability and shows feasibility for *in vivo* USF imaging. However, its on-to-off ratio is limited <10, which limits the signal-to-noise ratio. In the future, developing ICG-NP with a higher USF performance and meanwhile a maintained bio-stability is desired. In Chapter 3, we mainly synthesized a series of NIR fluorophore-encapsulated pluronic-based nanocapsules which are appropriate USF contrast agents. These nanocapsules have excellent USF properties such as a high I_{on}/I_{off}. The disadvantage is that currently the nanocapsules are limited only for in vitro USF imaging. They may not be directly used for *in vivo* USF imaging due to their bio-instability. Solutions to address the bio-stability should be explored and investigated in future.

7.2.1.2 Functionalization

Functionalization of USF contrast agents is an important step for achieving USF molecular imaging. In this dissertation, we have developed two types of ICG-NPs which have hydroxyl groups or carboxyl groups on the surface of the nanoparticles. They can be used for conjugation with other targeting moieties such as peptides, proteins or antibodies for molecular targeting and USF imaging in the future. Similarly, the pluronic-based nanocapsules have hydroxyl groups and they also have the potential for functional USF imaging.

7.2.2 USF imaging system

7.2.2.1 Time-domain USF imaging

In Chapter 4, we demonstrated the advantage of time-domain USF imaging that it is capable of reducing the short-lifetime background from long-lifetime USF signal, by appropriately delaying the time-gated window. The limitation is that we only demonstrated the effect of gating delay, by using a tissue-mimic silicone phantom with a total thickness of 4 mm, and by adding a quartz cuvette filled with contrast agents to mimic the strong background. In the future, the effect of gating delay should be investigated in centimeter-deep biological tissue. To achieve this, we need to develop a USF contrast agent that has a high τ_{on}/τ_{off}, a high quantum efficiency (i.e., a high I_{on}), and also a high τ_{on}. A high τ_{on}/τ_{off} ensures reducing the short-lifetime background fluorescence from long-lifetime USF signal, as already demonstrated in Chapter 4 by using the ZnttbPc nanocapsule. A high quantum efficiency of USF contrast agents ensures a high detection sensitivity in centimeter deep tissue. In Chapter 4, we also discussed that the ZnttbPc nanocapsule has a relatively low quantum efficiency (although it has a very high τ_{on}/τ_{off}) so we only demonstrate its USF imaging at 4 mm thickness. A higher I_{on} could help improve detecting USF photons from a larger depth. Meanwhile, the optical detector with a higher sensitivity is also desirable for achieving this. Last, high τ_{on} is necessary as well. This is because when fluorescence scatters in tissue, its pulse width will be convolved with a time delay due to scattering. This delay is more effective with the increase of tissue depth and may result in a significantly-reduced τ_{on}/τ_{off} when τ_{on} is equivalent to or smaller than the delay. To avoid this, it requires a high τ_{on} of a USF contrast agent. The ZnttbPc nanocapsule has a τ_{on} of ~3 ns. In the future, we will develop contrast agents that has an even higher τ_{on} (e.g., > 10 ns) for its benefit in centimeter-deep tissue time-domain USF imaging.

7.2.2.2 Utilizing the spatial information of a USF signal

In Chapter 5, we demonstrated that the USF signals' spatial information (i.e., 2D spatial scattering spot) acquired in a camera-based USF imaging system provides extremely useful information in improving the spatial resolution of a USF image, and we achieved this improvement by adopting the spatial back-projection algorithm. However, as discussed, with the increase of imaging depth, this algorithm showed its limited capability in the improvement because of more chaos of spatial and temporal information in a larger depth. Also, we didn't develop this algorithm with a universal protocol; as we analyzed the experimental data case by case, we adopted different values for signal processing, such as adopting a different threshold for signal segmentation in each case. In addition to these limitations, in a more realistic case, we should consider the algorithm's applicability in a model with a heterogeneous scattering and an uneven surface as well. In our future work, we aim to develop algorithms that could fully utilize the spatial information even when the USF photon comes from a deep biological tissue (> 5 mm). At the same time, we aim to improve the universality of the algorithms in different scenarios.

7.2.4 *In vivo* USF imaging

7.2.4.1 Bio-distribution of contrast agents in tumor

In Chapter 6, we did not study the bio-distribution of the USF contrast agents (e.g., ICG-NP) in tumor when intravenous injected. This study is very important for *in vivo* tumor USF imaging. Although we demonstrated *in vivo* tumor USF imaging by locally injecting the contrast agents in the mouse's tumor in Chapter 6, intravenous injection of the USF contrast agents is a highly preferable pathway for their targeting, accumulating, and labelling the tumor. This is being investigated in our lab.

7.2.4.2 Breathing motions

The breathing motions in *in vivo* USF imaging lead to increased fluorescence fluctuation noise (which means a low SNR) as well as the motion artifacts. The problem is severe especially in imaging the organs (e.g., spleen and liver), as demonstrated in Chapter 6. To avoid breathing motions, a possible solution is to adopt a respiratory trigger and acquiring *in vivo* USF signals during the animal's expiration phase.

References

1 Fass, L. Imaging and cancer: a review. *Mol. Oncol.* **2**, 115-152 (2008).

2 Siegel, R. L., Miller, K. D. & Jemal, A. Cancer statistics, 2016. *CA Cancer J. Clin.* **66**, 7-30 (2016).

3 Jalalian, A. *et al.* Computer-aided detection/diagnosis of breast cancer in mammography and ultrasound: a review. *Clin. Imaging* **37**, 420-426 (2013).

4 Cnudde, V. & Boone, M. N. High-resolution X-ray computed tomography in geosciences: A review of the current technology and applications. *Earth-Science Reviews* **123**, 1-17 (2013).

5 Fenster, A., Downey, D. B. & Cardinal, H. N. Three-dimensional ultrasound imaging. *Phys. Med. Biol.* **46**, R67 (2001).

6 Warner, E. *et al.* Systematic review: using magnetic resonance imaging to screen women at high risk for breast cancer. *Ann. Intern. Med.* **148**, 671-679 (2008).

7 Houssami, N. & Hayes, D. F. Review of preoperative magnetic resonance imaging (MRI) in breast cancer: should MRI be performed on all women with newly diagnosed, early stage breast cancer? *CA Cancer J. Clin.* **59**, 290-302 (2009).

8 Yang, W. T. *et al.* Inflammatory breast cancer: PET/CT, MRI, mammography, and sonography findings. *Breast Cancer Res. Treat.* **109**, 417-426 (2008).

9 Pennant, M. *et al.* A systematic review of positron emission tomography (PET) and positron emission tomography/computed tomography (PET/CT) for the diagnosis of breast cancer recurrence. *Health Technol. Assess.* (2010).

10 Mariani, G. *et al.* A review on the clinical uses of SPECT/CT. *European journal of nuclear medicine molecular Imaging* **37**, 1959-1985 (2010).

11 Lichtman, J. W. & Conchello, J.-A. Fluorescence microscopy. *Nature methods* **2**, 910 (2005).

12 Pifferi, A. *et al.* New frontiers in time-domain diffuse optics, a review. *J. Biomed. Opt.* **21**, 091310 (2016).

13 Schmitt, J. M. Optical coherence tomography (OCT): a review. *IEEE Journal of selected topics in quantum electronics* **5**, 1205-1215 (1999).

14 Van Dam, G. M. *et al.* Intraoperative tumor-specific fluorescence imaging in ovarian cancer by folate receptor-α targeting: first in-human results. *Nat. Med.* **17**, 1315 (2011).

15 Hilderbrand, S. A. & Weissleder, R. Near-infrared fluorescence: application to in vivo molecular imaging. *Curr. Opin. Chem. Biol.* **14**, 71-79 (2010).

16 Corlu, A. *et al.* Three-dimensional in vivo fluorescence diffuse optical tomography of breast cancer in humans. *Opt. Express* **15**, 6696-6716 (2007).

17 Xu, C. T. *et al.* High-resolution fluorescence diffuse optical tomography developed with nonlinear upconverting nanoparticles. *ACS nano* **6**, 4788-4795 (2012).

18 Andresen, V. *et al.* Infrared multiphoton microscopy: subcellular-resolved deep tissue imaging. *Curr. Opin. Biotechnol.* **20**, 54-62 (2009).

19 Webb, A. & Kagadis, G. C. Introduction to biomedical imaging. *Med. Phys.* **30**, 2267-2267 (2003).

20 Aime, S., Castelli, D. D., Crich, S. G., Gianolio, E. & Terreno, E. Pushing the sensitivity envelope of lanthanide-based magnetic resonance imaging (MRI) contrast agents for molecular imaging applications. *Acc. Chem. Res.* **42**, 822-831 (2009).

21 Licha, K. in *Contrast Agents II* 1-29 (Springer, 2002).

22 Pansare, V. J., Hejazi, S., Faenza, W. J. & Prud'homme, R. K. Review of long-wavelength optical and NIR imaging materials: contrast agents, fluorophores, and multifunctional nano carriers. *Chem. Mater.* **24**, 812-827 (2012).

23 Stride, E. & Saffari, N. Microbubble ultrasound contrast agents: a review. *Proceedings of the Institution of Mechanical Engineers, Part H: Journal of Engineering in Medicine* **217**, 429-447 (2003).

24 Frangioni, J. V. In vivo near-infrared fluorescence imaging. *Curr. Opin. Chem. Biol.* **7**, 626-634 (2003).

25 Weissleder, R., Tung, C.-H., Mahmood, U. & Bogdanov Jr, A. In vivo imaging of tumors with protease-activated near-infrared fluorescent probes. *Nat. Biotechnol.* **17**, 375 (1999).

26 Hoffman, R. M. Green fluorescent protein imaging of tumour growth, metastasis, and angiogenesis in mouse models. *The lancet oncology* **3**, 546-556 (2002).

27 Hu, C.-D. & Kerppola, T. K. Simultaneous visualization of multiple protein interactions in living cells using multicolor fluorescence complementation analysis. *Nat. Biotechnol.* **21**, 539 (2003).

28 Yamamoto, N., Tsuchiya, H. & Hoffman, R. M. Tumor imaging with multicolor fluorescent protein expression. *Int. J. Clin. Oncol.* **16**, 84-91 (2011).

29 Ntziachristos, V. Going deeper than microscopy: the optical imaging frontier in biology. *Nature methods* **7**, 603 (2010).

30 Santi, P. A. Light sheet fluorescence microscopy: a review. *Journal of Histochemistry Cytochemistry* **59**, 129-138 (2011).

31 Huang, B., Bates, M. & Zhuang, X. Super-resolution fluorescence microscopy. *Annu. Rev. Biochem.* **78**, 993-1016 (2009).

32 Shen, K., Lu, H., Baig, S. & Wang, M. R. Improving lateral resolution and image quality of optical coherence tomography by the multi-frame superresolution technique for 3D tissue imaging. *Biomedical optics express* **8**, 4887-4918 (2017).

33 Wang, L. V. Multiscale photoacoustic microscopy and computed tomography. *Nature photonics* **3**, 503 (2009).

34 Streeter, J. E., Gessner, R., Miles, I. & Dayton, P. A. Improving sensitivity in ultrasound molecular imaging by tailoring contrast agent size distribution: in vivo studies. *Mol. Imaging* **9**, 7290.2010. 00005 (2010).

35 Cai, W. & Chen, X. Multimodality molecular imaging of tumor angiogenesis. *J. Nucl. Med.* **49**, 113S-128S (2008).

36 Lakowicz, J. R. *Principles of fluorescence spectroscopy*. (Springer Science & Business Media, 2013).

37 Seddon, B. & Workman, P. The role of functional and molecular imaging in cancer drug discovery and development. *The British journal of radiology* **76**, S128-S138 (2003).

38 Rudin, M. & Weissleder, R. Molecular imaging in drug discovery and development. *Nature reviews Drug discovery* **2**, 123 (2003).

39 Culver, J., Akers, W. & Achilefu, S. Multimodality molecular imaging with combined optical and SPECT/PET modalities. *J. Nucl. Med.* **49**, 169-172 (2008).

40 Yuan, B. & Zhu, Q. Separately reconstructing the structural and functional parameters of a fluorescent inclusion embedded in a turbid medium. *Opt. Express* **14**, 7172-7187 (2006).

41 Xu, X., Liu, H. & Wang, L. V. Time-reversed ultrasonically encoded optical focusing into scattering media. *Nature photonics* **5**, 154 (2011).

42 Si, K., Fiolka, R. & Cui, M. Fluorescence imaging beyond the ballistic regime by ultrasound-pulse-guided digital phase conjugation. *Nature photonics* **6**, 657 (2012).

43 Si, K., Fiolka, R. & Cui, M. Breaking the spatial resolution barrier via iterative sound-light interaction in deep tissue microscopy. *Sci. Rep.* **2**, 748 (2012).

44 Wang, Y. M., Judkewitz, B., DiMarzio, C. A. & Yang, C. Deep-tissue focal fluorescence imaging with digitally time-reversed ultrasound-encoded light. *Nature communications* **3**, 928 (2012).

45 Judkewitz, B., Wang, Y. M., Horstmeyer, R., Mathy, A. & Yang, C. Speckle-scale focusing in the diffusive regime with time reversal of variance-encoded light (TROVE). *Nature photonics* **7**, 300 (2013).

46 Lai, P., Suzuki, Y., Xu, X. & Wang, L. V. Focused fluorescence excitation with time-reversed ultrasonically encoded light and imaging in thick scattering media. *Laser physics letters* **10**, 075604 (2013).

47 Liu, Y., Feshitan, J. A., Wei, M.-Y., Borden, M. A. & Yuan, B. Ultrasound-modulated fluorescence based on donor-acceptor-labeled microbubbles. *J. Biomed. Opt.* **20**, 036012 (2015).

48 Liu, Y., Yuan, B. & Vignola, J. Effect of fluorescent particle size on the modulation efficiency of ultrasound-modulated fluorescence. *International journal of optics* **2012** (2012).

49 Yuan, B., Pei, Y. & Kandukuri, J. Breaking the acoustic diffraction limit via nonlinear effect and thermal confinement for potential deep-tissue high-resolution imaging. *Applied physics letters* **102**, 063703 (2013).

50 Yuan, B. & Liu, Y. Ultrasound-modulated fluorescence from rhodamine B aqueous solution. *J. Biomed. Opt.* **15**, 021321 (2010).

51 Yuan, B., Liu, Y., Mehl, P. M. & Vignola, J. Microbubble-enhanced ultrasound-modulated fluorescence in a turbid medium. *Applied physics letters* **95**, 181113 (2009).

52 Yuan, B. Ultrasound-modulated fluorescence based on a fluorophore-quencher-labeled microbubble system. *J. Biomed. Opt.* **14**, 024043 (2009).

53 Jarrett, C. W., Caskey, C. F. & Gore, J. C. Detection of a novel mechanism of acousto-optic modulation of incoherent light. *PLoS One* **9**, e104268 (2014).

54 Hall, D. J., Sunar, U. & Farshchi-Heydari, S. Quadrature detection of ultrasound-modulated photons with a gain-modulated, image-intensified, CCD camera. *The Open Optics Journal* **2** (2008).

55 Kobayashi, M., Mizumoto, T., Shibuya, Y., Enomoto, M. & Takeda, M. Fluorescence tomography in turbid media based on acousto-optic modulation imaging. *Applied Physics Letters* **89**, 181102 (2006).

56 Yuan, B., Gamelin, J. & Zhu, Q. Mechanisms of the ultrasonic modulation of fluorescence in turbid media. *Journal of applied physics* **104**, 103102 (2008).
57 Pei, Y. *et al.* High resolution imaging beyond the acoustic diffraction limit in deep tissue via ultrasound-switchable NIR fluorescence. *Sci. Rep.* **4**, 4690 (2014).
58 Yuan, B., Uchiyama, S., Liu, Y., Nguyen, K. T. & Alexandrakis, G. High-resolution imaging in a deep turbid medium based on an ultrasound-switchable fluorescence technique. *Applied physics letters* **101**, 033703 (2012).
59 Lin, Y., Kwong, T. C., Gulsen, G. & Bolisay, L. Temperature-modulated fluorescence tomography based on both concentration and lifetime contrast. *J. Biomed. Opt.* **17**, 056007 (2012).
60 Lin, Y., Bolisay, L., Ghijsen, M., Kwong, T. C. & Gulsen, G. Temperature-modulated fluorescence tomography in a turbid media. *Applied physics letters* **100**, 073702 (2012).
61 Liu, Y., Feshitan, J. A., Wei, M.-Y., Borden, M. A. & Yuan, B. Ultrasound-modulated fluorescence based on fluorescent microbubbles. *J. Biomed. Opt.* **19**, 085005 (2014).
62 Huynh, N. T., Hayes-Gill, B. R., Zhang, F. & Morgan, S. P. Ultrasound modulated imaging of luminescence generated within a scattering medium. *J. Biomed. Opt.* **18**, 020505 (2013).
63 Cheng, B. *et al.* Development of ultrasound-switchable fluorescence imaging contrast agents based on thermosensitive polymers and nanoparticles. *IEEE Journal of Selected Topics in Quantum Electronics* **20**, 67-80 (2014).
64 Yu, S. *et al.* New generation ICG-based contrast agents for ultrasound-switchable fluorescence imaging. *Sci. Rep.* **6**, 35942 (2016).
65 Cheng, B. *et al.* High-resolution ultrasound-switchable fluorescence imaging in centimeter-deep tissue phantoms with high signal-to-noise ratio and high sensitivity via novel contrast agents. *PLoS One* **11**, e0165963 (2016).
66 Cheng, B. *et al.* The mechanisms and biomedical applications of an NIR BODIPY-based switchable fluorescent probe. *Int. J. Mol. Sci.* **18**, 384 (2017).
67 Kandukuri, J., Yu, S., Yao, T. & Yuan, B. Modulation of ultrasound-switchable fluorescence for improving signal-to-noise ratio. *J. Biomed. Opt.* **22**, 076021 (2017).
68 Kandukuri, J. *et al.* A dual-modality system for both multi-color ultrasound-switchable fluorescence and ultrasound imaging. *Int. J. Mol. Sci.* **18**, 323 (2017).
69 Yao, T., Yu, S., Liu, Y. & Yuan, B. Ultrasound-Switchable Fluorescence Imaging via an EMCCD Camera and a Z-Scan Method. *IEEE Journal of Selected Topics in Quantum Electronics* **25**, 1-8 (2019).
70 Yao, T., Yu, S., Liu, Y. & Yuan, B. In vivo ultrasound-switchable fluorescence imaging. *arXiv preprint arXiv:.04997* (2018).
71 Yu, S., Yao, T. & Yuan, B. An ICCD camera-based time-domain ultrasound-switchable fluorescence imaging system. *Sci. Rep.* **9**, 10552 (2019).
72 Wang, L. V. & Hu, S. Photoacoustic tomography: in vivo imaging from organelles to organs. *Science* **335**, 1458-1462 (2012).
73 Chen, Y. & Li, X. Near-infrared fluorescent nanocapsules with reversible response to thermal/pH modulation for optical imaging. *Biomacromolecules* **12**, 4367-4372 (2011).
74 Marshall, S., Milligan, A. & Yates, R. Experimental techniques and anaesthesia in the rat and mouse. *ANZCCART Facts sheet. ANZCCART News* **7**, 4 (1994).
75 Hicklin, D. J. & Ellis, L. M. Role of the vascular endothelial growth factor pathway in tumor growth and angiogenesis. *J. Clin. Oncol.* **23**, 1011-1027 (2005).
76 Taketoshi, N., Baba, T., Schaub, E. & Ono, A. Homodyne detection technique using spontaneously generated reference signal in picosecond thermoreflectance measurements. *Rev. Sci. Instrum.* **74**, 5226-5230 (2003).
77 Liang, Z.-P. & Lauterbur, P. C. *Principles of magnetic resonance imaging: a signal processing perspective*. (SPIE Optical Engineering Press, 2000).
78 Yao, T., Yu, S., Liu, Y. & Yuan, B. In vivo ultrasound-switchable fluorescence imaging. *Sci. Rep.* **9**, 9855 (2019).
79 Monici, M. Cell and tissue autofluorescence research and diagnostic applications. *Biotechnol. Annu. Rev.* **11**, 227-256 (2005).
80 Marshall, M. V. *et al.* Near-infrared fluorescence imaging in humans with indocyanine green: a review and update. *Open surgical oncology journal* **2**, 12 (2010).
81 Ayers, F., Grant, A., Kuo, D., Cuccia, D. J. & Durkin, A. J. in *Biomedical Optics (BiOS) 2008.* 687007-687007-687009 (International Society for Optics and Photonics).

82 Engel, E. *et al.* Light-induced decomposition of indocyanine green. *Investigative ophthalmology visual science* **49**, 1777-1783 (2008).

83 Nagano, T. Development of fluorescent probes for bioimaging applications. *Proceedings of the Japan Academy, Series B* **86**, 837-847 (2010).

84 Terai, T. & Nagano, T. Fluorescent probes for bioimaging applications. *Curr. Opin. Chem. Biol.* **12**, 515-521 (2008).

85 Nolan, E. M. & Lippard, S. J. Small-molecule fluorescent sensors for investigating zinc metalloneurochemistry. *Acc. Chem. Res.* **42**, 193-203 (2008).

86 Bandi, V. *et al.* Excitation-Wavelength-Dependent, Ultrafast Photoinduced Electron Transfer in Bisferrocene/BF2-Chelated-Azadipyrromethene/Fullerene Tetrads. *Chemistry–A European Journal* **19**, 7221-7230 (2013).

87 Chung, H. J. *et al.* Synthesis and characterization of Pluronic® grafted chitosan copolymer as a novel injectable biomaterial. *Current Applied Physics* **5**, 485-488 (2005).

88 WENQING, L. J. L. The Automatic thresholding of gray-level pictures via two-dimensional otsu method [J]. *Acta Automatica Sinica* **1**, 015 (1993).

89 De Jong, W. H. *et al.* Particle size-dependent organ distribution of gold nanoparticles after intravenous administration. *Biomaterials* **29**, 1912-1919 (2008).

Biographical Information

Shuai Yu was born in Ningbo, Zhejiang, China, in 1989. Shuai received his Bachelor of Science degree in Bio-technology from Zhejiang Sci-Tech University, Hangzhou, Zhejiang, China, in 2012. He continued his graduate studies in US since 2012 fall. Shuai received his Master of Engineering degree in Biomedical Engineering from The University of Southern California, Los Angeles, CA, US, in 2014. In 2014 fall, Shuai started his Ph.D. in Biomedical Engineering at the Joint Program of University of Texas at Arlington and University of Texas Southwestern Medical Center at Dallas, Texas, completing it by summer 2019. During this time, Shuai worked as a teaching assistant in the department and a research assistant in the ultrasound and optical imaging lab. His research expertise is in medical imaging instruments, ultrasound and optical imaging, fluorescence contrast agents, and operation of small animal imaging and surgeries. His research focus is developing ultrasound switchable fluorescence imaging techniques including developing novel fluorescence contrast agents and new imaging systems, as well as investigating pre-clinical imaging trials. During his Ph.D. studies, Shuai has published two first-author paper and five co-author papers on high-impact journals. Currently, he is preparing two additional first-author manuscripts for journal publication. Shuai has received Graduate Studies Dissertation Fellowship from the University of Texas at Arlington in 2019. In the future, he hopes to continue research in medical imaging techniques as well as medical facilities for public healthcare.